# Development of optical fibres to guide vacuum-ultraviolet and other extreme wavelengths

Winter, Bartlomiej

*Award date:*
2021

*Awarding institution:*
University of Bath

# Development of optical fibres to guide vacuum-ultraviolet and other extreme wavelengths

submitted by

Bartlomiej Winter

for the degree of Doctor of Philosophy

of the

University of Bath

Department of Physics

March 2021

*Dedicated to my dad,*

*David Winter OBE*

# Acknowledgements

I've been at Bath Uni. since September 2013. Over those many years, I have met lots of interesting people and made many great friends, with my time as part of the CPPM being no exception. I have lots of people to thank during my time as a PhD student. Firstly, I could not have asked for a better supervisor. William's guidance was key to my development as a scientist and without his excellent mentorship, I very much doubt that I would've enjoyed my research as much as I did. I would also like to thank my second supervisor Tim. His insights during my project were also vital to its progression. I will be forever grateful to both William and Tim for giving me the opportunity to have worked on such an awesome PhD.

I would also like to extend my thanks to other members of the CPPM. In no particular order, Adam, Carlo, Ross, Lukas, Leah, Tabijah, Olly, Stephanos, Tom, and Kristina, thank you! And to Will Rowe, I want to say thank you for the great conversations and your MatLab betterFigures library which saved me lots of time writing this thesis! I spent many an hour in the fibre drawing tower, and I thoroughly enjoyed the many chats I had with Steve and also appreciate the support he provided during fibre fabrication.

Moving across the pond, I was lucky enough to visit Boulder, Colorado twice during my PhD. I had a great time there and have Brian, Dmitry, and Emily to thank for that! It was an experience I will never forget.

I would also like to show my appreciation and thanks for the undying support and love from my partner Kamila. Lastly, I would like to thank my family as well as hers for the support they have provided me during my studies. I dedicate this thesis to the memory of my father whose values I will always hold close to my heart.

As I move out to the wider world I have one message. Winter is coming.

# Abstract

Creating optical fibres which transmit ultraviolet (UV) wavelengths is challenging due to the material absorption and photodarkening effects of silica glass, the most commonly used material in optical fibres, at these wavelengths. Previous studies have managed to guide down to deep-UV wavelengths ($> 200$ nm) using a hollow-core negative curvature fibre (HCNCF) to evade the material absorption of glass. The research presented here further develops this type of optical fibre by creating the first multimode HCNCF where it was found that the number of guided modes scales faster with core area than that of a solid-core step-index fibre. The goal was to guide vacuum-UV wavelengths ($< 190$ nm) for space-based applications. The results were successful such that a multimode hollow-core negative curvature optical fibre was manufactured which was shown to guide wavelengths down to 135 nm through the antiresonant effect and as far as 110 nm through glancing angle reflections.

Due to the success of the hollow-core negative curvature structure in the vacuum-UV it was conjectured that a similar performance would be seen at other extreme wavelengths, specifically 10 μm. The issues at this wavelength is similar to that in the UV where the loss is dominated by the material absorption of glass. To combat this, current optical fibres which guide this wavelength have their core-cladding boundary coated with a metal and are cylindrical in shape. The research concluded that a metal-coated hollow-core negative curvature fibre had a greater loss than its hollow-core metal-coated cylindrical fibre counterpart. However, it did provided insights into the guiding mechanisms which makes a hollow-core negative curvature fibre low loss at shorter wavelengths.

# Contents

# Chapter 1

# Background

Following the first optical fibre in 1952, the technology has become an integral part of modern society (Hecht and Hecht 1999). Optical fibres have found applications in a variety of fields such as in long-distance communication, medical research and non-linear optics to name a few (Buchanan 2015). There are many different types of optical fibres which guide light in a variety of ways with the primary goal being to transmit as much light as possible from the input end to the output, whether it is in a straight or curved line.

The research undertaken, primarily by myself, focused on the development of hollow-core optical fibres to guide extreme wavelengths, namely the vacuum-ultraviolet (VUV) and mid-infrared (mid-IR). Here, extreme wavelengths are frequency regions where silicon dioxide ($SiO_2$), the predominant material which optical fibres are made from absorbs strongly (Kitamura et al. 2007). Therefore, traditional solid-core optical fibres

whose guiding region is made of $SiO_2$ are unable to transmit these wavelengths and hence another type of optical fibre needs to be developed.

Hollow-core optical fibres are a viable alternative. They have an empty core which means they do not suffer from material absorption in the central guided region making them a viable candidate to guide wavelengths which would have otherwise be absorbed. The predominant wavelengths of interests are sub-190 nm which is defined as the VUV region. Furthermore, the work performed also aimed to manufacture optical fibres for the mid-IR $> 5$ μm.

The primary theme of the research presented in this thesis was on enabling guidance via an optical fibre within the VUV. The implications of this research would allow for the creation of space-bound astrophotonic technologies as well as further the development of medical devices. In terms of the former application the flexibility of these structures allow for the creation of a bundle of fibres to be placed onto a satellite to collect high-energy photons from celestial objects. This 2D array of fibres would be funneled down to a 1D array where the propagating light would be focused onto a slit which would diffract the radiation onto a spectrometer, creating VUV spectral maps of different regions in space. Moreover, this type of optical fibre would greatly simplify the calibration of VUV sensitive apparatus as current technology relies on the steady alignment of an optical set-up during the launch of a rocket (Chamberlin et al. 2004).

The research performed, primarily by myself, in the mid-IR was centered around creating large (relative to the guided wavelength) hollow-core optical fibres to deliver high-power laser light, which would otherwise damage a solid core fibre (Yao et al. 2018). The aim was to improve on current optical fibres by manufacturing one with low-loss guidance in the mid-IR. There are also wavelengths, such as 10 μm, where

current state-of-the-art cylindrical optical fibres suffer relatively high losses. However, using 'traditional' materials such as silica glass is not possible at these wavelengths due to the high material absorption. Instead the cylindrical optical fibres are made with a different dielectric material and often include a metal layer in order to transmit these wavelengths. A theoretical model on concentric ring Bragg fibres (Bird 2017) was used and extended, to accommodate metals, to theoretically test whether or not the cylindrical fibre model is optimal to guide 10 μm or whether the primary type of fibre which is subject of this thesis could produce a lower loss. The results would potentially lead to re-designing hollow-core optical fibres for 10 μm guidance.

The field of UV optical fibre technology has received a lot of attention in recent years (Matsuura and Miyagi 2004, Hartung et al. 2015, Galleani et al. 2017, Yu et al. 2018, Gao et al. 2018, Habib et al. 2018). However, the literature on the subject can be quite inconsistent when referring to the wavelength ranges in the UV. For clarity they will be defined here. UV refers to a wavelength range of 220-400 nm, whilst deep-UV is between 190-220 nm. The wavelength range which is the subject of this work, VUV, covers wavelengths less than 190 nm.

## 1.1 Developments of ultraviolet guiding optical fibres

Before moving onto the work I did on VUV guiding optical fibres it is worth reviewing what others did in the development of UV guiding fibres as it highlights some of the challenges that are needed to be overcome in order to push the guidance to even shorter wavelengths. Early in the development of UV fibres the optical fibres had a solid-core and were made of undoped silica, meaning that the efficiency of the guidance was at the mercy of the material properties in the UV. The UV-intrinsic losses down to approximately 230 nm were dominated by Rayleigh scattering (Heitmann 1990, Siegel Jr 1974). The solid-core prevented long-term use below 230 nm due to the UV

induced defects in the silica glass, an effect known as photodarkening which increases the absorption of UV radiation (section 1.3.2) (Klein et al. 1997, Karlitschek et al. 1995, Fabian et al. 1991, Friebele 1986, Friebele et al. 1985, Weeks 1994, Khalilov et al. 1994). Several other factors also contributed to the loss in the UV such as contaminants in the preforms of the fibre, a poorly manufactured fibre and also any post-processing treatments of the optical fibres which could degrade performance such as tapering. The problem of photodarkening was temporarily overcome by doping the optical fibres with O-H (section 1.3.2). The problem was the longevity of the use of these fibres as the UV performance degraded significantly after just a few hours (Heimann et al. 2013). Although improvements were made in this respect by refining the manufacturing process of these fibres, the guidance wavelength was limited to the deep-UV i.e. (Khalilov et al. 2014, 2015) above 190 nm. The limitation revolved around the design that was being used which was a solid-core optical fibre which guided light via total internal reflection (Klein and Khalilov 2015). In order to push the transmission to the VUV a new type of optical fibre would need to be used.

The initial development of VUV optical fibres came in 2004 (Matsuura and Miyagi 2004). In this study the authors coated the inside of a silica glass capillary with a thin layer of aluminium to overcome the strong absorption of silica glass at VUV wavelengths (Kitamura et al. 2007). Although this work was motivated by guiding 193 nm wavelength light from a ArF-excimer laser the researchers aimed to push the coated capillary design to wavelengths sub-190 nm (Matsuura and Miyagi 1998, 1999). The optical fibres used glancing angle guidance to transmit light from one end to the other as the shallow angle improved reflectivity (Marcatili and Schmeltzer 1964). The advantage of this design is that with a large core relative to wavelength, in their case 1 mm, the confinement loss (straight line guidance loss, section 2.1.2) is very low as the effective number of bounces per unit length of lower-order modes is low, minimising the interaction of the radiation with the surface. In their case they measured a loss

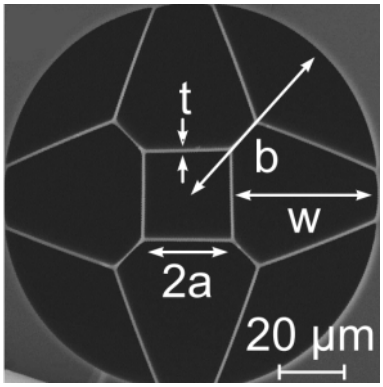


(a)

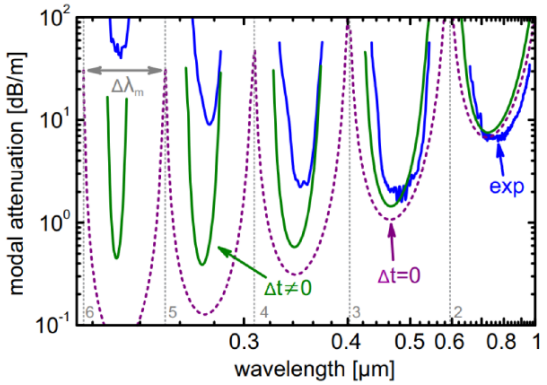


(b)

Figure 1-1: (a) SEM image of the square core fibre. (b) experimental attenuation curve (blue), along with theoretical loss curves if the wall thickness variation was fixed (green, $\Delta t = 70$ nm) and excluded (dotted purple). The grey numbers to the bottom-right of the dotted-grey vertical lines represent the resonance order. $\Delta t$ represents the variation the the wall thickness $t$ across the fibre. $\Delta\lambda_m$ is the width of the theoretical transmission region when $\Delta t = 0$. (Hartung et al. 2015)

of approximately 1.8 dB/m at a wavelength of 190 nm. The compromise with a large core is that the fibre suffers a high-bend loss (equation (2.19)). For a 1 mm diameter core, at a wavelength of 193 nm and a bend diameter of 33 cm the loss was measured to be approximately 3 dB. The bend loss was measured by creating a half-bend in the fibre of 180°.

The next significant iteration came in 2014 when the development of optical fibres for UV guidance moved away from a capillary structure to one which used the antiresonant guiding effect (section 2.1, Hartung et al. 2015, Litchinitser et al. 2002). In this structure the core of the fibre is in a square shape with the thickness of the wall being 560 nm. An SEM image of the fibre along with it's attenuation spectrum is shown in figure 1-1. This wall thickness is quite large for deep-UV guidance, let alone for the VUV. That can be seen from the attenuation spectrum where the loss starts to increase dramatically the shorter the wavelength, even though the theory of confinement loss suggests that the loss should decrease (dashed-line). The reason can be attributed to the material loss endured by the glass at shorter wavelengths. A wall thickness of

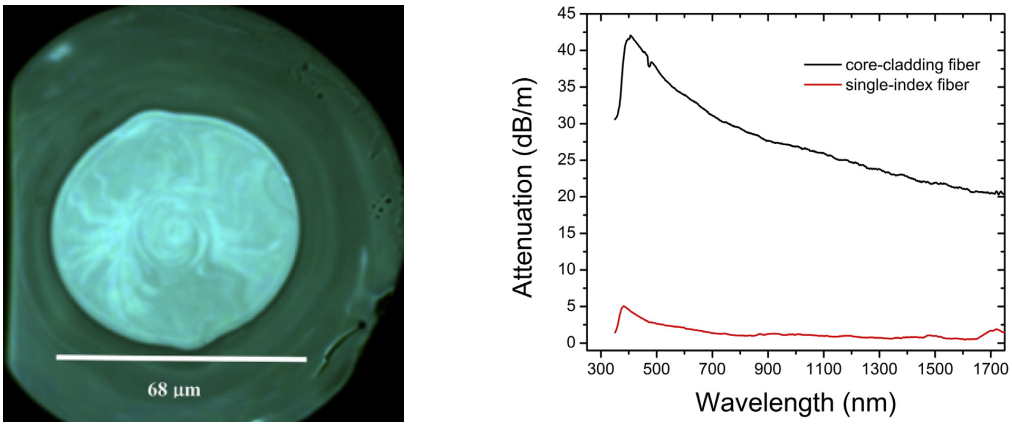


(a) (b)

Figure 1-2: (a) SEM image of the fibre's cross-section showing the core (light green/blue) and the cladding (dark green). (b) Attenuation spectra of the single-index fiber (red curve) and core-cladding fiber (black curve) measured by the cut-back method on 3 fiber sections. (Galleani et al. 2017)

560 nm would mean that the light penetrating the glass gets heavily attenuated before being reflected back into the core, thus minimising the beneficial effect that is derived from anti-resonance guidance.

Due to the absorption effects of silica glass (figure 1-7) most of the development in this field revolved around hollow-core optical fibres to minimise the material attenuation at UV wavelengths. However, some attempts have been made to guide deep-UV solid-core structure even though the results presented in the research paper goes down to the UV (Galleani et al. 2017). This optical fibre guides light through total internal reflection (Hecht 2015). An SEM image of the fibre's cross section as well as the transmission of the optical fibre can be seen in figure 1-2. The optical fibre was built from fluorophosphate glass which had a low attenuation in the UV compared to standard silicon dioxide. The difficulty in manufacturing from this soft glass material is the tight temperature range where the glass can actually be made into an optical fibre. As a result the authors managed to draw a 20 cm long piece of fibre. The shortest wavelength loss

measurement in this optical fibre was at 350 nm where it was measured to be 30 dB/m. The high value is attributed to the imperfections at the core cladding boundary.

Due to the possible applications of UV optical fibres in precision spectroscopy, optical clocks and quantum information processing, primarily revolving around maximising the UV throughput, there has been research performed in developing a different type of optical fibre, known as a hollow-core negative curvature fibre (HCNCF), for UV guidance (Wan et al. 2014, Ludlow et al. 2015, Häffner et al. 2005). One attempt looked to overcome the photo-darkening issues of glass in the UV by producing a deep-UV guiding hollow optical fibre (Skuja et al. 2001). A paper reported an attenuation of 0.1 dB/m at a wavelength of 218 nm (Yu et al. 2018). As of time of writing this optical fibre produced the lowest loss for deep-UV wavelengths. An SEM image of the cross-section and the attenuation measurement of the optical fibre is shown in figure 1-3. The most significant aspect of this optical fibre is that it was produced directly from a fibre drawing tower (section 2.2). The significance of this comes from simultaneously managing the stress on a fibre with a small cross-section whilst actively pressurising the tubes to inflate them typically leads to a runaway inflation, resulting in tubes that will over-inflate and touch due to the instability of the drawing process. In this case many meters of a single optical fibre was produced allowing for an effective cut-back

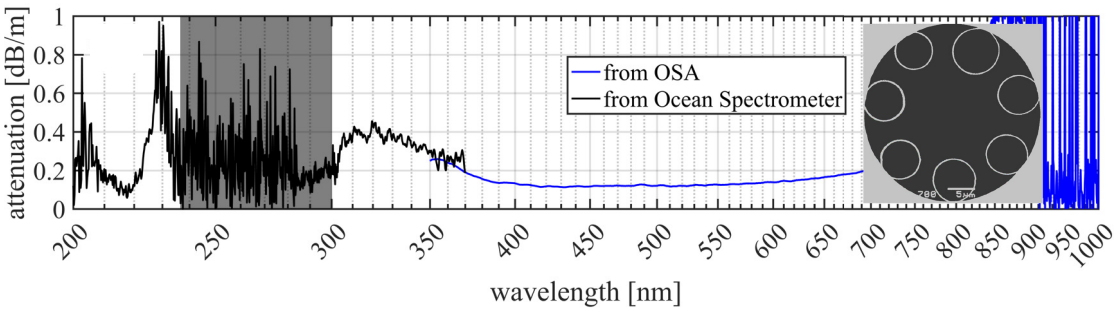


Figure 1-3: Attenuation curve of the fibre measured via a cut-back measurement from 33.6 m to 8.4 m. The inset shows an SEM image of the fibre's cross-section with a wall thickness of approximately 132 nm. (Modified from (Yu et al. 2018))

measurement to attain the attenuation (section 2.1.3). However, pushing deeper into the deep-UV is made even more challenging due to the rapid increase of the refractive index in the VUV (Kitamura et al. 2007).

There have also been some more unorthodox designs in an attempt to use hollow fibres for UV guidance. One study has demonstrated transmission at 260 nm (Gao et al. 2018). Although the wavelength is not as short as that from (Yu et al. 2018, figure 1-3), the interesting aspect comes from the structure of the fibre itself. Figure 1-4 shows 4 large tubes surrounding a small core. F. Gao *et al* claim that even with this structure the fibre guides in the UV. However, attenuation results show that when nearing the deep-UV region, only simulation results are presented. Being unable to measure deep-UV guidance is not a surprise as the resonator wall thickness is approximately 420 nm. This optical fibre suffers the same material loss as (Hartung et al. 2015, figure 1-1) because the thick walls absorb much of the deep-UV light which penetrates them, making the reflection back into the core significantly weaker.

The research papers discussed so far have investigated transmitting UV light through an optical fibre. However, there have been successful attempts in generating deep-UV

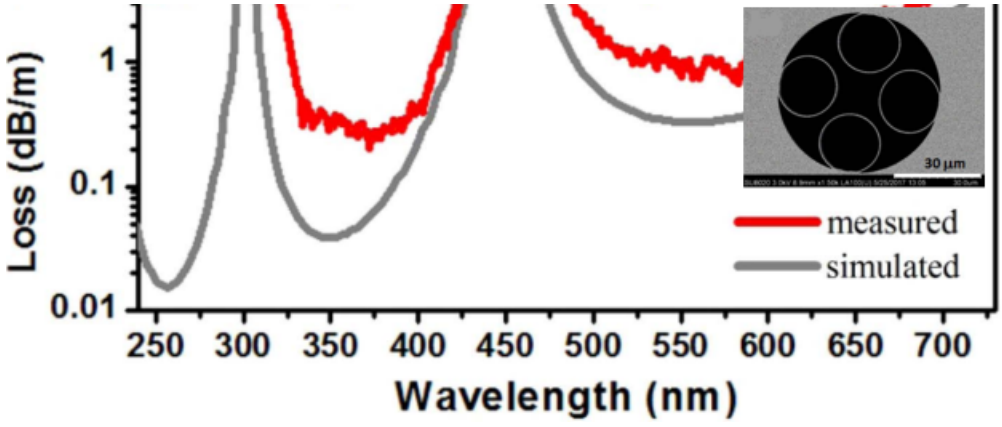


Figure 1-4: Attenuation curve measured via a cut-back measurement from 5 m to 1 m. Inset shows an SEM image of the fibre's cross-section with a wall thickness of approximately 420 nm. (Modified from (Gao et al. 2018))

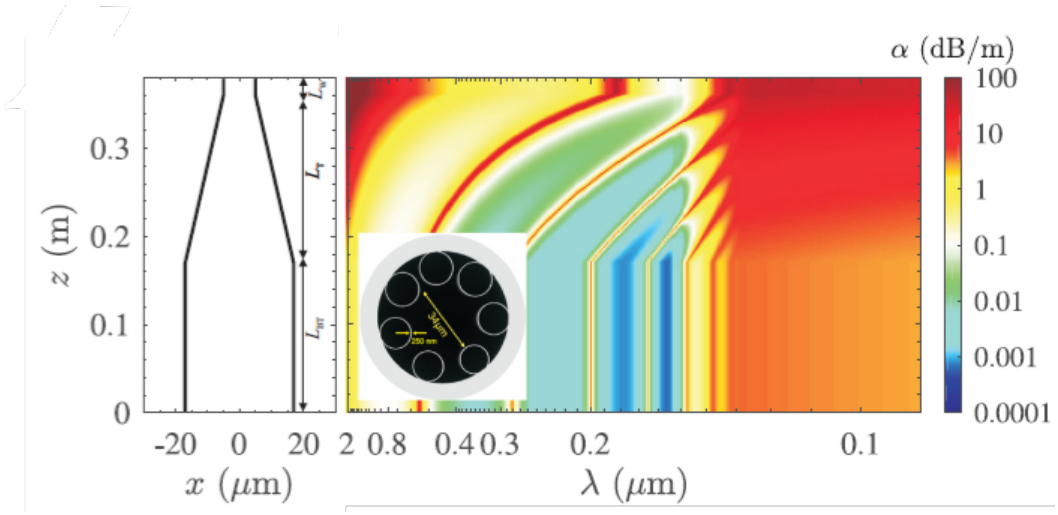


Figure 1-5: Tapered schematic of the optical fibre. Initial untapered length of 17 cm with a fibre core diameter of 34 μm followed by a 19 cm taper which reduced the fibre core diameter to 10 μm. The final waist length of the optical fibre is 2 cm. Simulated attenuation (inset) SEM image of the original untapered optical fibre with a 34 μm core diameter and a tube wall thickness of 250 nm. (Modified from (Habib et al. 2018))

and VUV light inside an optical fibre also. Although, the light is generated and not guided for the whole fibre length due the non-linear processes involved, i.e. creating dispersive waves through soliton generation and the effect of Rayleigh length (Fox 2002). The research performed in (Habib et al. 2018) involved filling a HCNCF with Neon gas in order to excite the non-linear processes (figure 1-5). Pumping the optical fibre with a 30 fs 10 μJ pulse energy, at a wavelength of 800 nm in a 34 μm diameter core fibre which is filled with Ne gas at a pressure of 9 bar produced VUV wavelengths (Dudley and Taylor 2010). The outer diameter of the optical fibre was also reduced along its length in order to guide some of these VUV wavelengths. The results showed that although the optical fibre did emit these VUV wavelengths, the VUV was produced at the end of the structure. The long Rayleigh length does also mean that the light's interaction with the tubes was minimised. The authors note that the simulations of the loss in this fibre, although not experimentally measured, suggested that the small core at the output end resulted in an attenuation coefficient of 0.1 dB/m at 150 nm. This theoretical low loss gives confidence in developing an optical fibre to guide these VUV wavelengths.

Research in the field of UV guiding optical fibres has been picking up pace since the development of HCNCF. The work demonstrated in this summary does suggest that the future of high photon energy guidance is in a hollow-core negative curvature type of structure. Thus far, the shortest actively-guided demonstration was in the deep-UV, namely 218 nm (Yu et al. 2018). Other work has shown that the generation of VUV wavelengths in these structures is possible but they do not demonstrate low-loss guidance such that the optical fibres can be used to transmit a practical amount of VUV light from one end to the other. This gap is the primary theme of this thesis, to develop a HCNCF which can actively guide VUV wavelengths.

## 1.2 Mid-infrared guidance in metal coated hollow-core optical fibre

Although not the main theme of this thesis, work has been performed to see if there are any beneficial effects from using hollow-core negative curvature fibres to guide in the mid-infra-red (mid-IR), specifically 10 μm. Current state-of-the-art optical fibres at this wavelength have a high confinement loss of 0.2 dB/m. Improvements in the loss performance have been centred around developments in the manufacturing of the optical fibres, which are cylindrical in shape. Therefore examining if the hollow-core negative curvature structure could reduce the loss would be beneficial for the field of mid-IR guiding optical fibres which has been stagnant in the model of fibre used. Before exploring the effects of using a HCNCF for this purpose however, understanding why the cylindrical shape of fibre has remained the primary design choice would be beneficial.

The problems faced with guiding light in the IR is similar to those in the UV, silica glass becomes very absorbent (Kitamura et al. 2007). Therefore most solid-core optical fi-

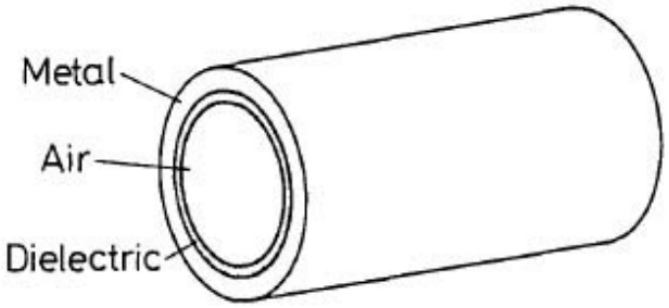


Figure 1-6: Schematic of the configuration for a hollow-core optical fibre designed to guide infrared wavelengths. The structures have a dielectric film which is deposited on a metal surface. The metal boundary is also generally in-cased in a glass or polymer material (Matsuura et al. 1990).

bres designs become replaced with a hollow-core model. Hollow-core cylindrical optical fibres are used in many different fields from high-power laser delivery, spectroscopy and radiometry (Saggese et al. 1991, Saito et al. 1990). A cylindrical shape with a hollow-core which guides light through glancing angle reflections (Marcatili and Schmeltzer 1964) is the most common model used in this field. However, there are some types of optical fibres which guide through a form of total internal reflection, even though the core is hollow. These types of optical fibres are made of a dielectric material which has a refractive index of less than 1 in the mid-IR (Harrington and Gregory 1990). The structure of these fibres consists of a dielectric film which coats the inside of a metal cladding. When comparing optical fibres for the mid-IR and the VUV the material composition is different. A HCNCF for the VUV consists of a single dielectric material, silica glass whilst for the mid-IR the optical fibres require more than one type of material. In this case it is generally a dielectric layer which is surrounded by a metal.

The HCNCF model will be compared to a structure which is of the type as in figure 1-6 where an air-core is surrounded by a dielectric layer of material which in turn is surrounded by a layer of metal. These structures are currently the state of the art model for 10.6 μm guidance, with confinement losses of 0.25 dB/m (dielectric ZnS, metal Ag) (Matsuura and Miyagi 1993) and 0.048 dB/m (dielectric Ge, metal Ag) (Mat-

suura et al. 1990). Commercially the lowest-loss fibre available is 0.2 dB/m (AgI/Ag, Molex/Polymicro). These optical fibres all have core diameters at least 100 times the wavelength making their straight line confinement loss low (equation (2.18)). Predictably bend-loss suffers with the bend loss being approximately 1 dB for the ZnS/Ag optical fibre and 2.5 dB for the Ge/Ag coated structure for a bend diameter of 33 cm (180° bend). The commercial counterpart states a bend loss of 1 dB but does not state the bend diameter.

Work in this field has not developed much during the last three decades in terms of moving away from the capillary type of structure. The attenuation in these optical fibres is relatively high in practical terms, let alone the bend loss. However, with the advent of the HCNCF, research in this thesis investigates if this new structure of HCNCF can produce a lower loss than its cylindrical equivalent. If the results show that a HCNCF does produce a lower loss then it will provide grounds to start researching how a HCNCF with a dielectric layer which surrounds a metal will be manufactured.

## 1.3 Properties of silica glass in the VUV and mid-IR

The challenges of fabricating an optical fibre for the VUV and mid-IR primarily revolved around mitigating the material loss of silica glass, the most popular type of glass used to manufacture this technology. Therefore, the vast majority of optical fibres developed to guide these wavelength ranges were based around hollow-core structures where the light is guided in air, thus, minimising the material absorption. Understanding the behaviour of silica glass at the wavelengths of interest is paramount to creating a viable optical fibre to guide those wavelengths.

### 1.3.1 Refractive index and extinction coefficient

The two most relevant optical properties of a material are the refractive index, $n$, and the extinction coefficient $\kappa$. The total refractive index of a material is given by (Canit et al. 1969),

$$\tilde{n} = n + i\kappa \tag{1.1}$$

where $\tilde{n}$ is the total refractive index. $\kappa$ defines how strongly the medium absorbs light at a given wavelength.

Figure 1-7 shows how the refractive index and extinction coefficient of silica glass behave between 10 nm and 1000 nm. In the VUV the refractive index and extinction coefficient experiences a rise. At 185 nm the real part of the refractive index has a value of approximately 1.59 which is very different from that of 1.45 between the visible and the near-IR. In terms of the extinction coefficient at 185 nm the value is about $5 \cdot 10^{-6}$ and at 150 nm it is $1 \cdot 10^{-3}$. Translating the extinction coefficient into attenuation can be done via (Fox 2002),

$$\alpha = \frac{2\omega\kappa}{c} \tag{1.2}$$

where $\alpha$ is the absorption coefficient which is measured in per meter, $\omega$ is the angular frequency and $c$ is the speed of light in a vacuum. In experimental terms the absorption coefficient translates to an attenuation (loss) of $1.5{\cdot}10^3$ dB/m and $3.6{\cdot}10^5$ dB/m. These enormous material losses reinforce the motivation to develop a hollow-core optical fibre to guide these extreme wavelengths. However, in the VUV, two-photon absorption which causes photo-darkening (section 1.3.2) also has an impact on the transmission properties by increasing the absorption in the VUV.

Moving to the infrared towards 10 μm it can be seen that the extinction coefficient and refractive index rise rapidly, with the rise of the refractive index starting to in-

crease at about 9 μm (see figure 1-8). The extinction coefficient also increases to approximately 2 at 10 μm which translates to an attenuation of $1.1 \cdot 10^7$ dB/m. This high extinction coefficient is due to the vibrational bonds between $SiO_4$ (Hanna 1965).

### 1.3.2 Photodarkening in the UV

It was mentioned in section 1.3.1 that the photodarkening phenomenon can occur in silica glass due to UV radiation. This is an unwanted effect which leads to an increase in the absorption of light in both the UV and visible. Photodarkening is caused by light itself through one or two photon absorption (Kajihara et al. 2004). It occurs when a bond in a stressed multiple member $(Si\text{-}O)_n$ ring is optically broken. O-Si-O bonds rarely rest at their natural angle in silica glass increasing the chances that they break due to one or two-photon absorption of UV light. The absorption causes the O-Si-O bond to break resulting in a dangling Si bond which absorbs strongly in the UV (Galeener 1985, Stone et al. 2013).

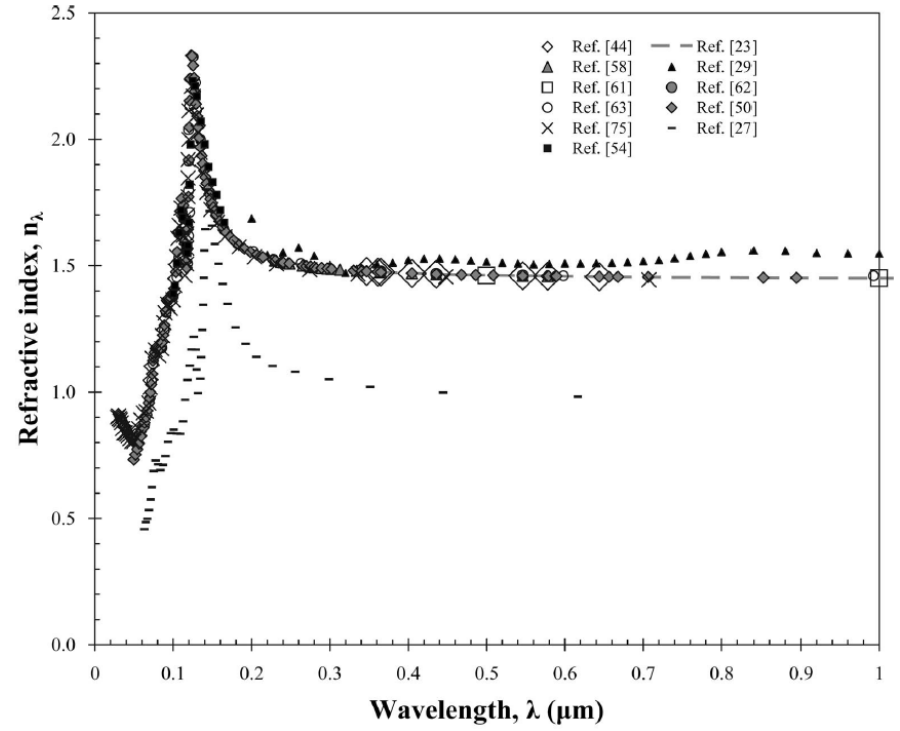


(a)

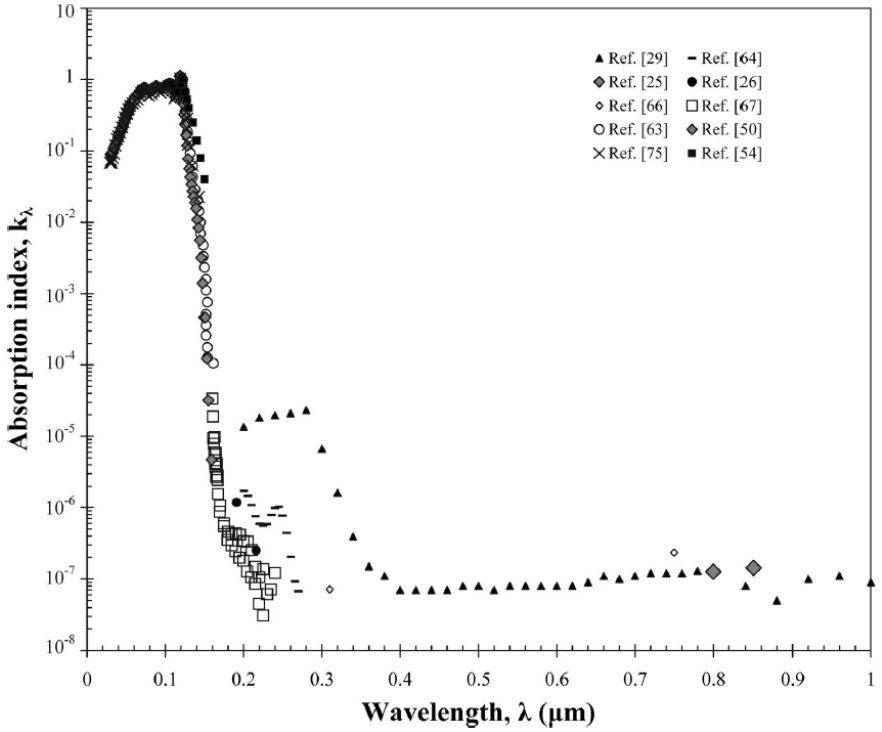


(b)

Figure 1-7: (a) Refractive index profile, (b) extinction coefficient for silica glass between 10 to 1000 nm. (Kitamura et al. 2007)

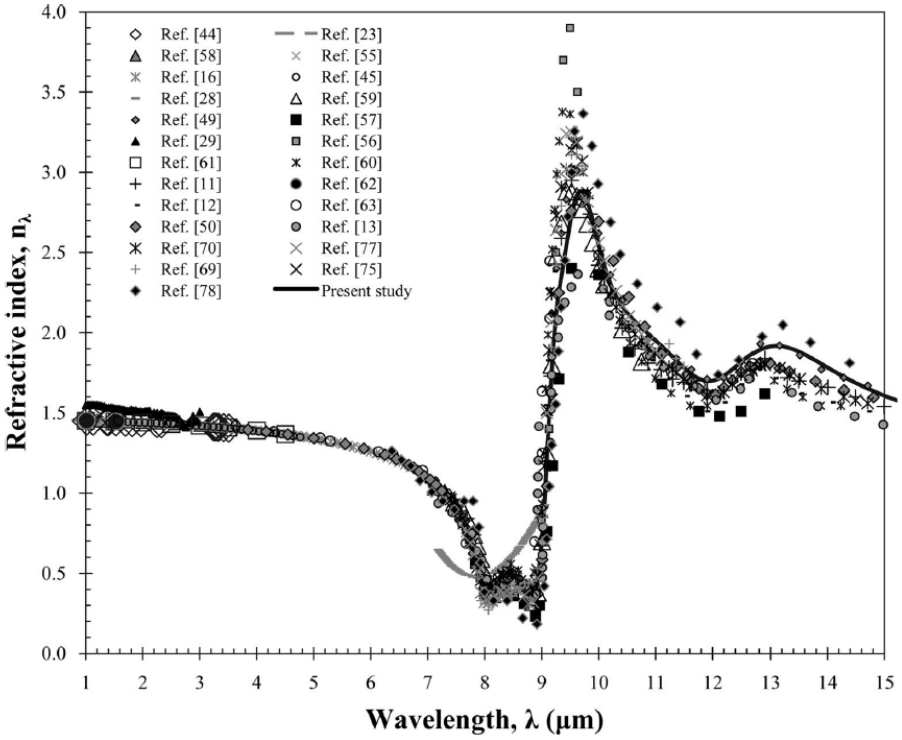


(a)

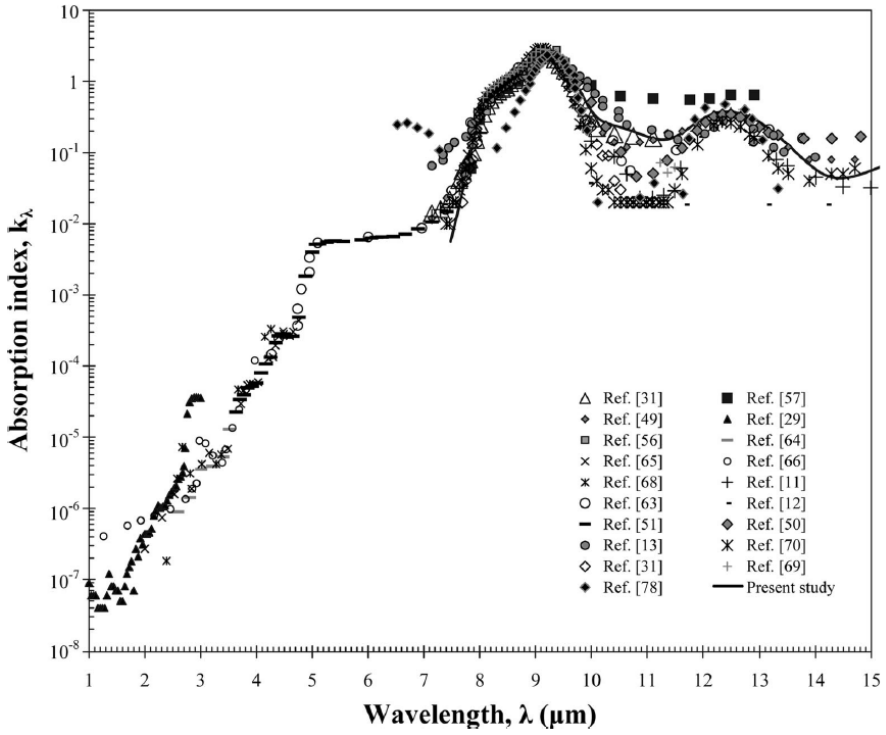


(b)

Figure 1-8: (a) Refractive index profile, (b) extinction coefficient for silica glass between 1 to 15 μm. (Kitamura et al. 2007)

# Chapter 2

# Hollow-core negative curvature fibres

The development of hollow-core negative curvature fibres (HCNCF) for VUV and mid-infrared light delivery is the main theme of this thesis. These optical fibres (figure 2-1) consist of a hollow-core surrounded by a set of tubes. The name negative curvature derives from how the tubes curve away from the core. The optical fibre is made from a single material, silica glass. There are many variations which have emerged as the fibers were developed such as the contiguous HCNCF (figure 2-1(a)) which is where the tubes touch, the free-boundary HCNCF where the tubes do not touch (figure 2-1(b)) and then less common types such as the ice cream cone HCNCF (figure 2-1(c)) and the nested HCNCF (figure 2-1(d)). These optical fibres guide light through the antiresonant effect which is discussed in section 2.1. A thorough review can be found in (Yu and Knight 2016).

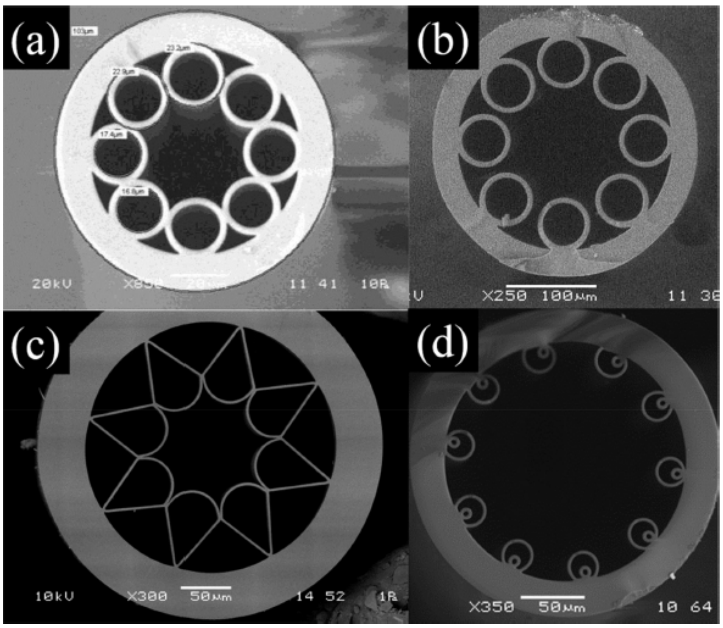


Figure 2-1: SEM of different types of negative curvature fibres (HCNCF). (a) Contiguous HCNCF (Pryamikov et al. 2011), (b) free-boundary HCNCF (Kolyadin et al. 2013, (c) ice cream cone HCNCF (Yu et al. 2012) and (d) nested free-boundary HCNCF (Belardi 2015). (Retrieved from (Yu and Knight 2016))

## 2.1 Anti-resonance effect

This guidance mechanism can be understood by considering a simple Fabry-Perot etalon, where two reflecting surfaces are separated by a distance $d$ (Modes 2020). Consider an input field $u_0$ which travels perpendicular to the left reflective boundary into a medium (figure 2-3). After passing through the first(left) reflective boundary the transmitted light will have an amplitude of $tu_0$, where $t$ is the transmission coefficient of both reflective surface. After passing through both the gap $d$ and the second(right) reflective surface the field $u_0$ acquires a phase term, due to the increase in optical density of the medium, such that the field is now $t^2u_0e^{ikd}$. The term $k$ is the wavevector perpendicular to the reflective boundary. The wave which gets reflected off the second(right) reflective surface is equal to $rtu_0e^{ikd}$ where $r$ is the reflectively of both reflective surfaces. Then when that particular wave is transmitted through the first(left) reflective

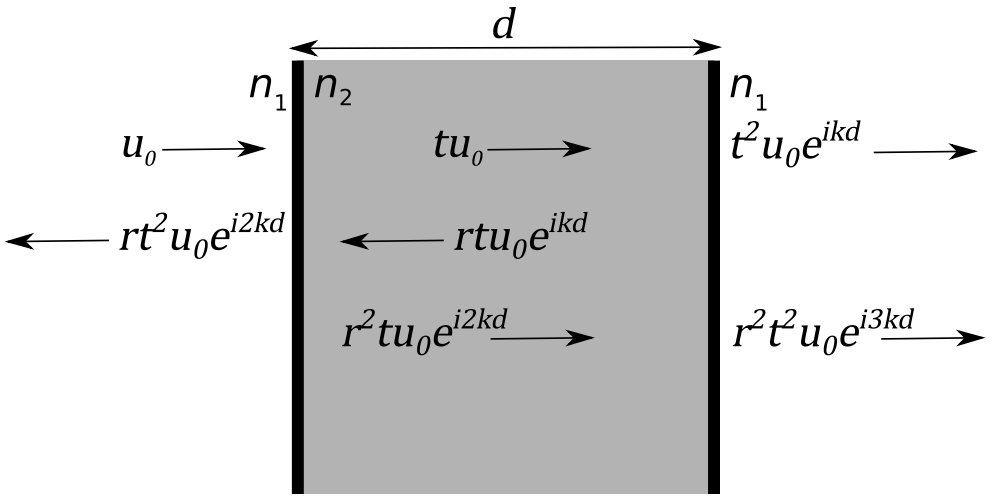


Figure 2-2: Fabry-Perot etalon with two reflective boundaries (solid vertical black lines) separated by a distance $d$. The regions to the left and right of the grey area has a refractive index $n_1$. The grey area in between the reflective surfaces has a refractive index $n_2$, where $n_2 > n_1$.

surface the field is $rt^2u_0e^{i2kd}$. The field which reflects off the first(left) reflective surface is $r^2tu_0e^{i2kd}$ and then when that passes through the medium of thickness $d$ and transmits through the second(right) reflective surface the field will be $r^2t^2u_0e^{i3kd}$ and so on. Adding up all of the fields which pass through the second(right) reflective surface to give the output field, $u_{out}$, yields

$$u_{out} = t^2u_0e^{ikd} + r^2e^{2ikd}t^2u_0e^{ikd} + (r^2e^{2ikd})^2t^2u_0e^{ikd} + (r^2e^{2ikd})^3t^2u_0e^{ikd} + ...$$

which can be re-written as

$$u_{out} = t^2u_0e^{ikd}[1 + r^2e^{2ikd} + (r^2e^{2ikd})^2 + (r^2e^{2ikd})^3 + ...]$$

Evaluating the geometric series to infinity gives,

$$u_{out} = \frac{t^2u_0e^{ikd}}{1 - r^2e^{2ikd}} \tag{2.1}$$

We know that $I \propto |u_{out}|^2$, where $I$ is the intensity. Calculating the intensity from equation (2.1) leads to,

$$I_{\text{out}} = \frac{T^2 I_{\text{in}}}{(1 - r^2 e^{2ikd})(1 - r^2 e^{-2ikd})} = \frac{T^2 I_{\text{in}}}{1 + R^2 - 2R\cos(2kd)}$$

where $T = t^2$, $R = r^2$ and $T + R = 1$. Using the trigonometric identity $\cos(2\theta) = 1 - 2\sin^2(\theta)$ leads to the final output intensity formula

$$I_{\text{out}} = \frac{I_{\text{in}}}{1 + \frac{4R}{T^2}\sin^2(kd)} \tag{2.2}$$

From equation (2.2) it can be seen that when $kd = m\pi$, where $m = 0, 1, 2, 3...$, $I_{\text{out}} = I_{\text{in}}$. All of the input light which is incident onto the cavity is passing straight through it, an effect known as *resonance*. Away from the resonance condition is where some of the field is returned back in the direction of $u_{in}$.

Figure 2-3 shows how the behaviour of the intensity changes as a function of the wavenumber in the Fabry-Perot etalon model. It can be seen that the region between the peaks remains broad for almost all of the values of $R$.

In addition, it must be noted that equation (2.2) cannot reach 0 when $\sin^2(kd) = 1$, so there is always light which passes through the second surface. The wide transmission regions means that this mechanism is a useful one to base the transmission properties of an optical fibre on, however, the surface does need to be highly reflective in order to have narrow resonances.

So far the wavevector $\vec{k}$ was considered to be in the transverse direction i.e. traveling normal to the cavity. Now consider the situation where multiple reflections which are travelling at an angle interfere which each other (Lipson et al. 2010, figure 2-4). In this scenario the wave is travelling from what can be thought of as the core of a

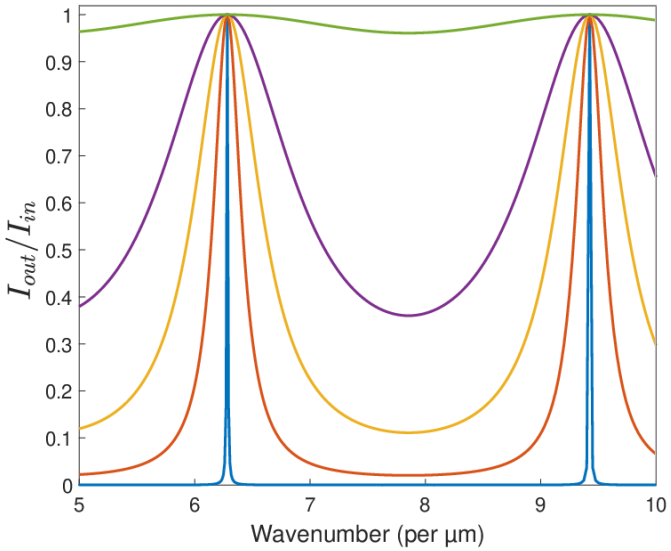


Figure 2-3: Intensity output of a Fabry-Perot cavity with a mirror separation distance of $d = 1\mu$m. The multiple curves represent the results for various values of mirror reflectivity, $R = 0.99$ (blue), $R = 0.75$ (orange), $R = 0.50$ (yellow), $R = 0.25$ (purple) and $R = 0.01$ (green).

HCNCF at an angle $\theta_0$ relative to the the surface. Equation (2.2) assumes that the wave is travelling perpendicular to the surface. From the geometry in figure 2-4 the transverse wavevector $k$ can be given as,

$$k = k_0 n_1 \cos(\theta_0) = k_0 n_2 \cos(\theta_1) \tag{2.3}$$

where $k_0$ is the free-space wavenumber. Therefore, $\sin^2(kd) \rightarrow \sin^2(k_0 n_2 d \cos(\theta_1))$.

Two assumptions are made to evaluate the model. Firstly, it is assumed that the medium is a dielectric such as silica glass. Having a dielectric material means that the ray of light which reflects off the surface without penetrating the medium undergoes a $\pi$ phase shift. Therefore, the condition of resonance, where the waves X and Y interfere destructively occurs when $k_0 n_2 d \cos(\theta_1) = m\pi$ where $m$ is an integer. The second assumption that is made is that the core diameter, $D$, of the hollow-core fibre follows $D >> \lambda$ where $\lambda$ is the wavelength. This condition creates a glancing angle of

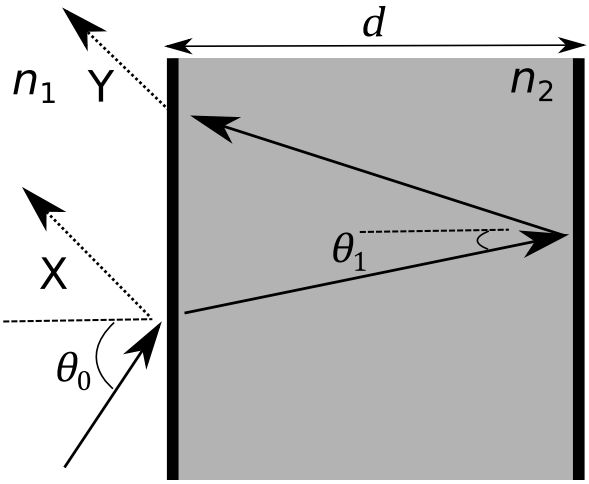


Figure 2-4: Schematic of a medium of width $d$ and refractive index $n_2$ with a wave traveling at an angle $\theta_0$ relative to the surface. The wave penetrates the medium at an angle $\theta_1$. Outside the medium the refractive index is $n_1$ where $n_2 > n_1$. The dashed arrows X and Y represent the rays which return to the region where the original incident ray came from.

incidence so $\theta_0 = \pi/2$. From Snell's law $n_1 \sin(\theta_0) = n_2 \sin(\theta_1)$ it can be deduced that,

$$\sin(\theta_1) = \frac{n_1}{n_2}. \tag{2.4}$$

Using the trigonometric identity $\cos^2(\theta)+\sin^2(\theta) = 1$ the resonance condition is written as,

$$k_0 n_2 d\sqrt{(1 - \sin^2(\theta_1))} = m\pi. \tag{2.5}$$

Substituting this result into equation (2.4), and also rewriting $k_0$ to $2\pi/\lambda$ and then making $\lambda$ the subject gives,

$$\lambda = \frac{2n_2 d}{m}\sqrt{\left(1 - \left(\frac{n_1}{n_2}\right)^2\right)}. \tag{2.6}$$

Multiplying the right-hand side by $(n_1/n_2)(n_2/n_1)$ so that $n_1$, which is air in the case of a hollow fibre and is therefore equal to 1, comes out in from of the square root.

Implementing this leads to the final result

$$\lambda_m = \frac{2d}{m}\sqrt{(n_2^2 - 1)}, \tag{2.7}$$

where $\lambda_m$ is the wavelength which matches the resonance order $m$. Equation (2.7) is commonly known as the resonance condition which is where, as in this example, the rays X and Y interact destructively in the core making the resonance wavelength high loss. When the wavefronts X and Y are in phase and interfere constructively the condition is known as the antiresonant condition. The antiresonant wavelength represents the minimum loss wavelength in between the appropriate resonances. For constructive interference to occur $\sin^2(k_0 n_2 d\cos(\theta_1)) = 1$, which is where equation (2.2) is at a minimum. Following the same derivation as equation (2.7) the antiresonant condition occurs at a wavelength which is given by,

$$\lambda_h = \frac{4d}{(2h+1)}\sqrt{\left(n_2^2 - 1\right)} \tag{2.8}$$

where $h$ is an integer which represents the transmission band order and where $\lambda_h$ is known as the anti-resonance wavelength.

Observing equations (2.7) and (2.8) it can be seen that the primary design parameter is $d$. Translating this to a HCNCF it would represent the tube wall thickness that can be seen from the rings surrounding the core as in figure 2-1(b). Equations (2.7) and (2.8) are also referred to as the ARROW (antiresonant reflecting optical waveguide) model (Litchinitser et al. 2002).

Looking at figure 2-4 the surface with which the light interacts is flat. Although this model works very well in predicting the location of the resonances, when designing an optical fibre it is also important to know what the loss will be for the guided wavelengths. As of time of writing, there is no analytical solution which can explain the

behaviour of light in a hollow-core negative curvature fibre. Attempts to understand the loss via the antiresonant effect has been made using Bragg fibre models (Yeh et al. 1978). These structures consist of concentric circles. The central circle was made of air with the next layer being glass which is then followed by an air layer and then glass again etc... The main result from this analysis is that the confinement loss (in dB) incurred through propagation through a distance of one wavelength $\lambda_0$ is (Bird 2017),

$$8.686 \left(\frac{x_0}{2\pi}\right)^{N+2} \left(\frac{1}{\sqrt{(\epsilon-1)}}\right)^{N+1} \left(\frac{\lambda_0}{r_c}\right)^{N+3} \prod_{i=1}^{N} \frac{1}{\sin^2(\phi_i)} \quad \text{(TE modes)} \tag{2.9}$$

$$8.686 \left(\frac{x_0}{2\pi}\right)^{N+2} \left(\frac{\epsilon}{\sqrt{(\epsilon-1)}}\right)^{N+1} \left(\frac{\lambda_0}{r_c}\right)^{N+3} \prod_{i=1}^{N} \frac{1}{\sin^2(\phi_i)} \quad \text{(TM modes)} \tag{2.10}$$

$$8.686 \left(\frac{x_0}{2\pi}\right)^{N+2} \frac{1}{2} \frac{\epsilon^{N+1}+1}{(\epsilon-1)^{(N+1)/2}} \left(\frac{\lambda_0}{r_c}\right)^{N+3} \prod_{i=1}^{N} \frac{1}{\sin^2(\phi_i)} \quad \text{(HE/EH modes)} \tag{2.11}$$

where $r_c$ is the core radius. $N$ is known as the number of antiresonant layers, i.e. the number of layers in which the light can reflect back into the core of the optical fibre. The factor 8.868 (=20/ ln(10)) is the conversion of the imaginary part of the propagation constant to a loss in dB. $x_0$ is a dimensionless quantity which is related to the mode (section 2.1.1) under consideration in the core through Bessel functions. $\epsilon$ is the relative dielectric constant of the glass regions.

The important factor in terms of resonance and antiresonant guidance to take away from equations (2.9), (2.10) and (2.11) is the final product series. Here $\phi_i$ are the phase angles corresponding to each successive layer in the Bragg fibre structure. For glass ($g$) and air ($a$) layers this is given by,

$$\phi_i^{(g)} = \frac{2\pi\sqrt{(\epsilon-1)t_i^{(g)}}}{\lambda_0} \quad \text{or} \quad \phi_i^{(a)} = \frac{x_0}{t_i^{(a)}} r_c \tag{2.12}$$

where $t_i^{(g)}$ or $t_i^{(a)}$ is the width of the $i$th layer and $r_c$ is the core radius. Anti-resonance occurs when $\phi_i = \pi/2, 3\pi/2, ...$ and resonance when $\phi_i = 0, \pi, \pi, ....$ For hollow-core negative curvature fibres $3 < N < 4$, therefore the loss can be approximated analytically using this Bragg fibre model.

We have considered a couple of ways of viewing the antiresonant guidance mechanism. They all revolve around the same concept. HCNCFs take advantage of the enhanced reflection provided by the light which re-enters the core after penetrating the tube's wall. This property is the fundamental difference between glancing angle guidance (Marcatili and Schmeltzer 1964) and it is what produces low loss propagation in this type of structure.

### 2.1.1 Modes in optical fibres

A mode is defined as a transverse spatial distribution which does not change in the direction of propagation except in phase. A useful comparison in understanding this concept is through the solutions of the Schrödinger equation in a 1D finite potential well (equation (2.13), Phillips 2013).

$$\psi(x) = \begin{cases} \cos(kx) & |x| < a \quad \text{Even} \\ \sin(kx) & |x| < a \quad \text{Odd} \\ Ae^{-k|x|} & |x| > a \end{cases} \tag{2.13}$$

where $\psi$ represents the wavefunction as a function of displacement $x$ from the center of the well. $a$ is half the width of the well, $k$ and $A$ are constants.

The ground state solution to the 1D well is an analog for the first solution of the scalar wave equation (Kokubun and Iga 1980) which returns the greatest propagation constant $\beta$. This value of $\beta$ corresponds to the fundamental mode in the optical fibre. Solutions

to the scalar wave equation are also discrete such as that in the Schrödinger equation. Moreover, outside the boundaries of the 1D well, unconfined continuum states exist. In terms of optical fibres this would be radiation which exists in the cladding where the light decays exponentially with distance. The description of modes given here is valid for step-index fibres where the refractive index of the core is greater than that of the cladding. Modes are considered to only be truly guided if this condition is met,

$$kn_1 < \beta \leq kn_2 \tag{2.14}$$

where $n_1$ is the refractive index of the cladding, $n_2$ is the refractive index of the core and $n_1 < n_2$. $k$ is the free space wavevector. Therefore, we can say that modes have an effective refractive index, $n_{\text{eff}}$, given by

$$n_{\text{eff}} = \frac{\beta}{k} \tag{2.15}$$

A useful quantity to be able to measure is the number of guided modes in a step-index fibre. Further analysis of the scalar wave equation for a step-index slab fibre leads to a parameter known as the normalised frequency $V$ which is defined as (Yeh 2013),

$$V = kaNA \tag{2.16}$$

where $a$ is the core radius of the fibre and $NA = \sqrt{n_2^2 - n_1^2}$ is the fibre's numerical aperture. From equation 2.16 we can derive the number of modes, $N_{\text{modes}}$, which are guided in a step-index fibre,

$$N_{\text{modes}} \approx \frac{V^2}{2} \tag{2.17}$$

So far, the analysis on modes has been done assuming a 'traditional' refractive index profile where the core has a greater refractive index than the cladding around it. We know that for a hollow-core fibre this physical property is inverted as the light exists in the low index core. Although the guiding mechanism is different to that of a step-index

fibre. The principle of equation (2.15) still holds true as the modes have an effective refractive index which is lower than the refractive index of the core.

Since the condition (2.14) is not possible in antiresonant guidance then technically these modes are not truly guided. They do share the same properties of guided modes such that the shape of the spatial distribution remains constant as they travel down the optical fibre. However, they have an extra property that they decay exponentially with distance. Increasing the core diameter of HCNCFs, defined as the distance between an outer tube to the opposite outer tube, with respect to wavelength greatly reduces the rate at which the light decays. The increase in propagation distance means that the low loss modes can essentially be treated as if they were truly guided as they would be in a solid-core fibre (Hu and Menyuk 2009).

Equation (2.17) shows how one can calculate the number of modes in a step-index fibre. However, in a hollow-core negative curvature fibre modes do not technically exist in

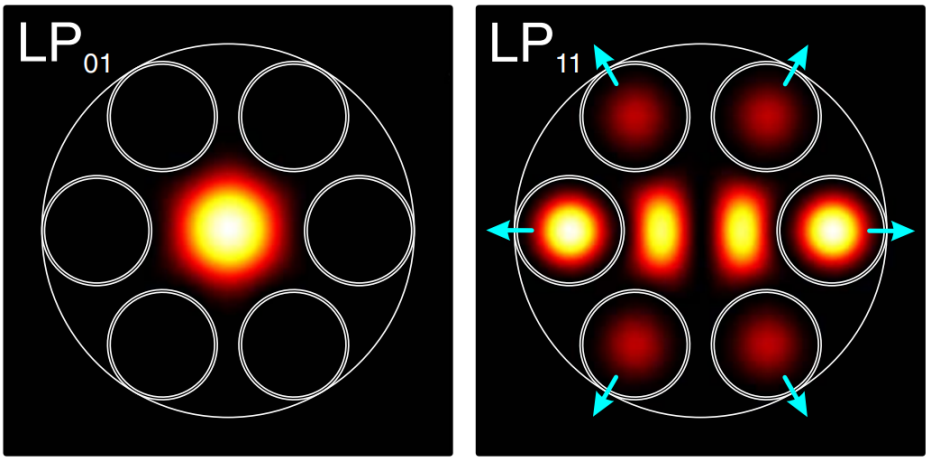


Figure 2-5: Possible design of a HCNCF for single-mode guidance. Here the ratio between the outer diameter of the tubes $d_{\text{tube}}$ and the core diameter $D$ is $d_{\text{tube}}/D \approx 0.68$ which is the condition for single mode guidance. With this ratio higher order modes couple into the tubes which in turn couple into cladding modes (arrows show the direction of coupling) which are then lost leaving the fundamental mode after a short distance of propagation. This quoted ratio limits the design of these fibres to have between 6 to 8 tubes. (Uebel et al. 2016)

the sense that they do not meet the condition (2.14), but as it was said earlier with a large enough core relative to wavelength they behave as if they were modes (with the addition of the exponential decay with distance). The difference between the 'modes' in the fibre is the rate at which they are attenuated. Therefore the concept of developing a single mode hollow-core negative curvature fibre is quite different from that for the standard step-index fibre which has a very well defined single-mode guidance regime (Yeh 2013). Single-mode guidance in a hollow-core negative curvature fibre is achieved through the engineering of the physical parameters of the optical fibre. The filtering of higher-order modes is done by matching the propagation constant $\beta$ of the lobes of the higher-order modes with modes which can exist inside the tubes. This has the effect of coupling the light in the core to inside the tubes which therefore greatly increases the rate at which the higher-order modes decay in the core (Uebel et al. 2016). From figure 2-5 it can be seen that the Gaussian distribution of the fundamental mode is confined in the core whilst the higher order mode is coupled into the resonators and then leaked out into the cladding and is lost. This outcome is achieved when $d_{\text{tube}}/D \approx 0.68$, where $d_{\text{tube}}$ is the outer diameter of the tube and $D$ is the diameter of the core of the fibre and also when $d/D = 0.1$ where $d$ is the wall thickness of the tube (Uebel et al. 2016). The ratios allow for the propagation constants $\beta$ of the lobes of the higher-order modes in the core to couple into and therefore match the $\beta$ of modes in the tubes. This causes the modes to leak out into the cladding to be lost which means that higher-order modes have a very high attenuation. To match these ratios hollow-core optical fibres are limited to 6-8 resonators.

Single-mode fibres (for step-index they have a normalised frequency, $V < 2.405$) have great benefits such as preserving mode quality (Peng et al. 2016), but are limited in some applications especially those which require high-power delivery (Harrington 2000). These uses are best suited for multi-mode fibres ($V \geq 2.405$) as the core relative to wavelength is much larger and thus minimises the interaction of the radiation with the

glass tubes. To obtain a multi-mode guiding optical fibre the ratios which generate single-mode guidance need to be broken. A simple way of doing this is to simply add more tubes. By doing this the ratio between $d_{\text{tube}}/D$ will mean that the lobes of some of the higher-order modes will be physically larger than the inside of the tubes, as can be seen from figure 2-5. This leads to the $\beta$ values of the higher-order modes to be mismatched with those inside the tubes, which therefore means the higher-modes in the core would not couple into the tubes and so propagate for a longer distance before being lost (Belardi and Knight 2014).

### 2.1.2 Confinement and bend loss

The primary goal of an optical fibre is to get as much of the input light to the output, whether that is in a straight line or when bent. When designing a silica glass hollow-core negative curvature fibre there are two kinds of loss under consideration, confinement loss and bend loss.

Confinement loss is straight line guidance loss of the optical fibre. As of the time of writing this thesis there is no analytical solution which can describe the confinement loss in a hollow-core negative curvature optical fibre. However, there are analytical models for simplified structures such as the Bragg fibre model from equations (2.11), (2.9) and (2.10) (Bird 2017) and also the Marcatili and Schmeltzer model which describes the confinement loss in a capillary type of structure (Marcatili and Schmeltzer 1964). For the latter model the confinement loss is given by (which is the $N = 0$ case of equations 2.9, 2.10 and 2.11),

$$\alpha_{vm} = \left(\frac{u_{vm}}{2\pi}\right)^2 \frac{\lambda^2}{r_c^3} \Re(V_v) \tag{2.18}$$

where $\alpha_{vm}$ is the attenuation of the mode, $u_{vm}$ is the $m^{th}$ zero of the Bessel function $J_{v-1}$, and $v$ and $m$ are azimuthal and radial number of modes, $\lambda$ is the wavelength, $r_c$ is

the core radius and $V_v$ is the constant determined by the cladding refractive index and mode order. The important factor from equation (2.18) and also equations (2.11), (2.9) and (2.10) (Bird 2017) is the $\lambda/r_c$ term. The ratio demonstrates that for a given core radius $r_c$ decreasing the wavelength will reduce the confinement loss whilst increasing the wavelength will increase the confinement loss.

Bend loss occurs due to the variation in distance that the modes have to travel between one side of the core and the opposite side (figure 2-6). The discrepancy in the distance means that the relative phase of mode on either side of the core is different. Therefore allowing one side of the mode to couple to other modes which it is in phase with leads to an increase in attenuation for the mode that suffered the initial phase-mismatch. For bend loss (Marcatili and Schmeltzer 1964) states it as,

$$\alpha_{vm} = \frac{r_c^3}{\lambda^2 R^2} \Re(V_v) \tag{2.19}$$

where $R$ is the radius of curvature of the optical fibre. Here, it can be seen that the relationship for bend loss is inverted when compared to confinement loss. For a given core radius $r_c$ and bend radius $R$, decreasing the wavelength will increase the bend loss whilst increasing the wavelength will reduce it. Also, note that the bend loss increases faster than the bend radius as $\alpha_{vm} \propto R^{-2}$.

So we know that the relationship between confinement and bend loss are reciprocals of each other. Therefore, a balance needs to be made between how design an optical fibre in such a way to minimise the loss. Of course the balance between confinement and bend loss is dependent on the application but experimentally it was found that a core diameter to wavelength relationship should follow $D = 30\lambda$ which is generally a good balance between bend and confinement loss.

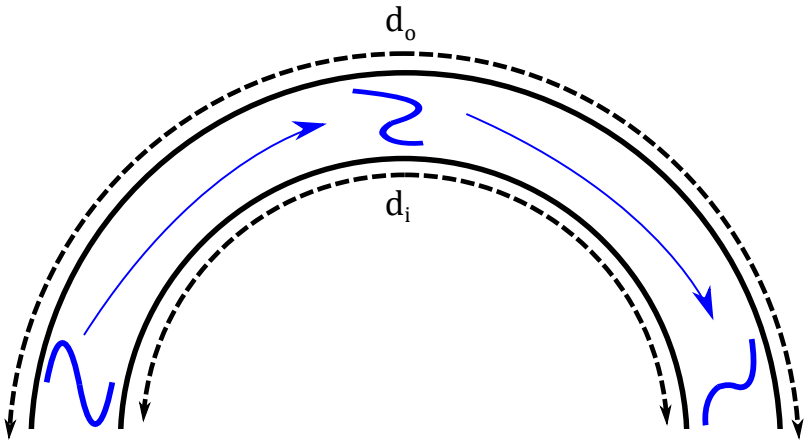


Figure 2-6: Change in phase across a bend for a mode due to distance $d_o$ being greater than distance $d_i$. Starting with the mode to the left, the left-hand lobe moves downwards whilst the right-hand lobe move upwards due to the differences on distances $d_o$ and $d_i$. The relative phase difference can cause the mode to couple to other modes and thus increase its attenuation.

### 2.1.3 Experimental measurement of confinement and bend loss

The primary method used to measure the confinement loss in an optical fibre is through the cut-back method (figure 2-7, Marcuse 2012). In this set-up the output power of the fibre is measured for the long piece (ideally $> 100$ meters), then the fibre is cut to a shorter length without disturbing the input and the output power is measured again. The formula, to give the loss in dB/m is given by

$$\alpha_{\mathrm{dB}} = -10\frac{\log_{10}\left(\frac{P_{\mathrm{out}}}{P_{in}}\right)}{L_1 - L_2} \tag{2.20}$$

where $\alpha_{\mathrm{dB}}$ is the attenuation in dB/m, $P_{\mathrm{out}}$ ($P_{\mathrm{in}}$) is the output(input) power of the fibre and $L_1(L_2)$ is the long(short) length of the fibre. $L_1$ is generally tens to hundreds of meters whilst $L_2$ is in the range of 5-10 meters to ensure that the high loss modes are filtered out of the measurement. This cut-back technique is the most common way of obtaining the loss of an optical fibre. A couple of practical points need to be tackled though, these also apply to bend loss measurements. Firstly the key here is to keep the input coupling unchanged to ensure that in input power is constant over the two lengths of fibre used, so the cutback is performed at the output end. Secondly, the long

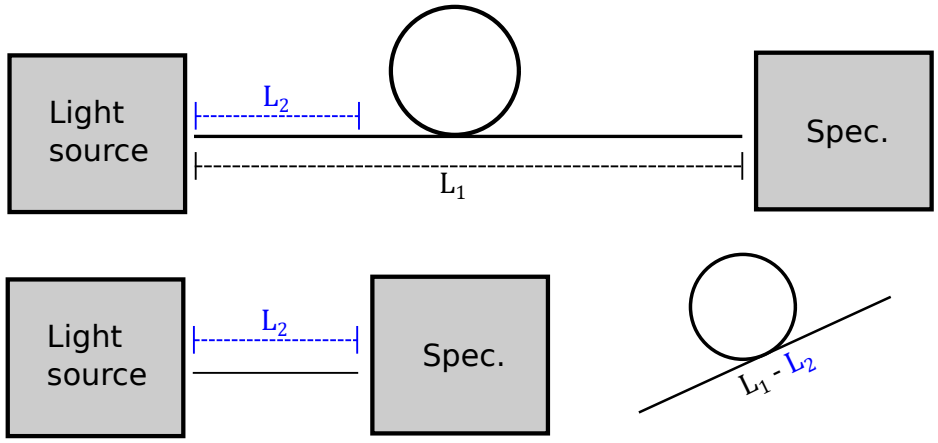


Figure 2-7: Schematic of a general set-up for a cut-back measurement. The emission from a light source is coupled into a fibre of length L and the output is then passed into a detector to measure its power spectrum over a certain wavelength range. (a) Initial measurement of the fibre's spectra of length $L_1$. (b) The same measurement but this time with the length of the fibre cut to $L_2$ leaving the input optics untouched.

length of the fibre will be too long to measure in a straight line. Therefore, the fibre will need to be laid out in many loops, here the radius of the loop needs to be large enough such that bend loss becomes as insignificant as possible.

Measuring the bend loss in an optical fibre is not too dissimilar to measuring the confinement loss. Here the fibre is laid out in large loops with the end of the fibre being initially straight to give a baseline measurement to compare tight bends to. Then the end straight part is bent to form a semi-circle of controllable radius (figure 2-8). Bend loss is measured in dB per half-turn and has a similar form to equation (2.20) with the absence of the length,

$$\alpha_{\mathrm{BL}} = -10 \log_{10} \left( \frac{P_{\mathrm{out}}}{P_{in}} \right) \tag{2.21}$$

where $\alpha_{BL}$ is the attenuation for a certain bend radius. There is a subtlety in this set-up that needs to be taken into account. The fibre is initially laid out in large loops with the bend at the end of the optical fibre. Laying it out in loops initially allows for the higher-order modes to propagate through the fibre. This allows for the bend loss of the higher-order modes to be part of the measurement as they are not filtered out

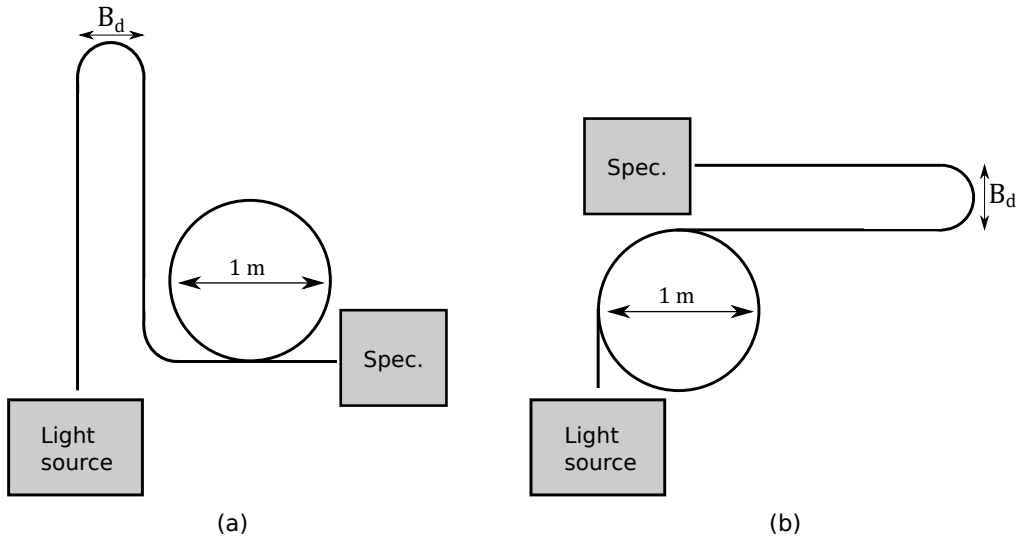


Figure 2-8: Schematic of two bend loss measurements. Both methods measure the loss for a bend diameter of $B_d$ with the loops of the fibre being large enough such that they are comparable in radius with that of the loops for a cutback measurement. (a) In order to filter out higher-order modes by increasing their loss at the start. A method that should be used when attempting to measure the loss of solely lower-order modes. (b) The bend is at the end of the set-up. This configuration is optimal when quantifying the overall bend loss of all of the 'low' loss modes, irrespective of their order.

at the start. Whereas having the bend near the input would cause the higher-order modes to be lost quickly and therefore not be part of the results. An experimental set-up like this would generally be used to measure the bend loss of the fundamental mode (Carter et al. 2017).

## 2.2 Fabricating hollow-core negative curvature optical fibres

Fabricating HCNCF can be done in multiple ways. However, the most common way to do so is through the stack and draw technique. Before explaining the stack and draw technique it would be best to describe the main piece of apparatus, the fibre drawing tower (figure 2-9). A fibre drawing tower is a vertical structure which comprises of three sections. The upper most section is that which holds the glass structure. The intermediate stage is where the glass structure is fed through the furnace. The glass

is placed inside the furnace until softened which occurs at a of temperature about 2000 $^{o}$C. Once the viscosity of the glass has been reduced it gets pulled by the final stage where the fibre gets wound around a drum.

The stack and draw technique is similar to that used to build photonic crystal fibres (Russell 2003). A stack is generally a 1 m in length and a few centimeters in diameter (figure 2-10(a)). Inside the stacking tube capillaries are placed. Capillaries will form the tubes of the optical fibre which is responsible for the antiresonant guidance effect. In between the capillaries, support tubes of usually the same outer diameter are also placed. The primary difference between the capillary tubes and support tubes is their length. Capillary tubes are approximately 10 cm longer than the stacking tube (the

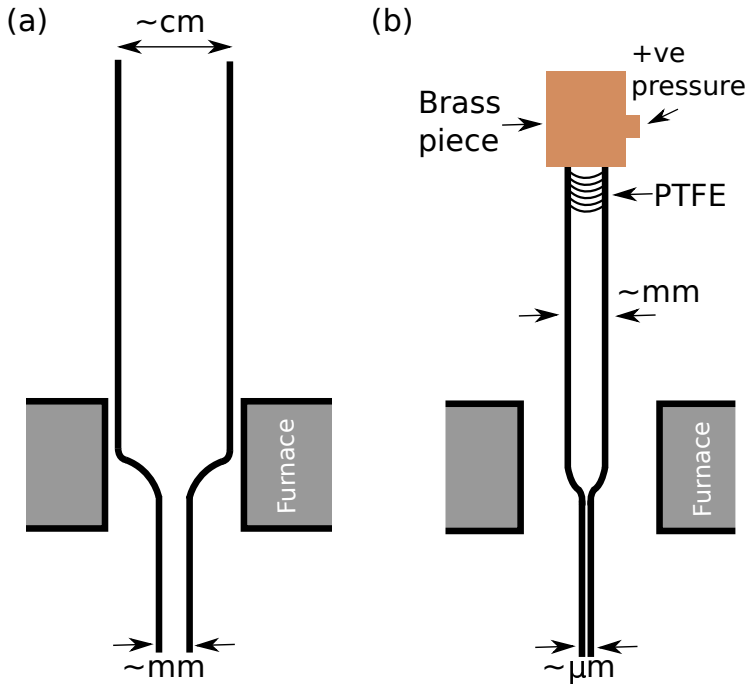


Figure 2-9: Schematic of the fibre tower for the (a) stack to cane stage and the (b) preform to fibre stage. (a) The stack gets fed into the furnace at a fixed rate which then gets drawn at a fixed rate, reducing the outer diameter into the cane. (b) The preform, which is a cane which has been prepared to be drawn, also gets fed into the furnace and draw into an optical both at a fixed rate. The tension is controlled by the temperature of the furnace as the feed and draw speed remain constant. The PTFE tape is used to provided a seal between the glass and brass piece.

tube which houses the structure), whilst the support tubes are only a fraction of that length. A central support tube, which also only runs a proportion of the length of the stacking tube, is used to keep the shape of the structure from collapsing. To finish off the structure PTFE tape is used to hold the top of the stack, as it can withstand up to 260 degrees Celsius before it deteriorates, whilst the bottom side is kept together by tungsten wire as it can withstand the high temperatures of the furnace (Langmuir 1915).

Once the stack is built it is drawn into canes (figure 2-10(c)). Canes are the intermediate step between stack and optical fibre. These structures generally have an outer diameter spanning millimeters. The cross-section of the cane looks very similar to that

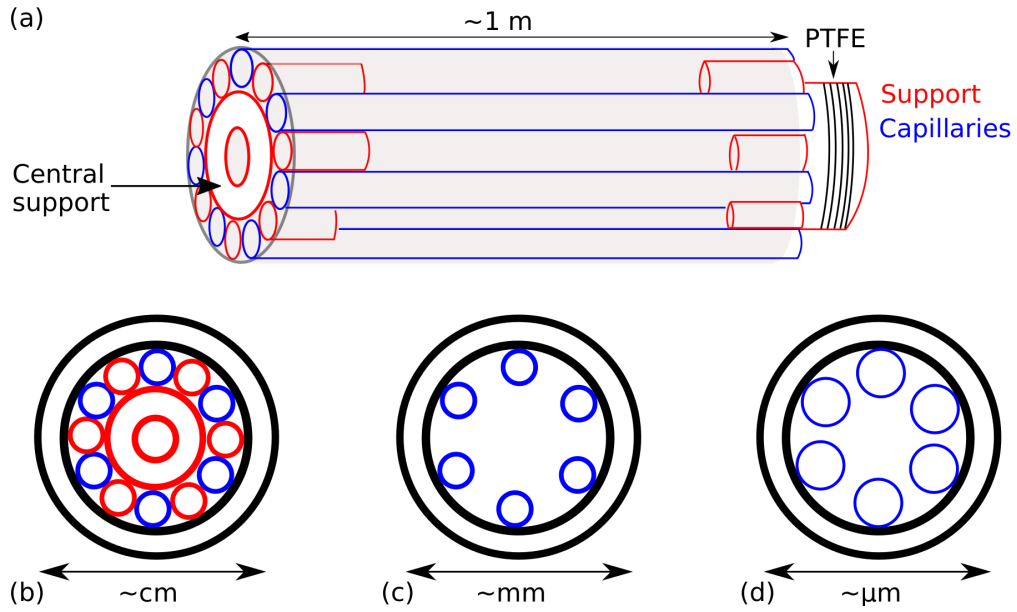


Figure 2-10: Schematic of the various stages in manufacturing a HCNCF. (a) The stacking tube which is generally about a meter long. The cylinders which have a blue outline represent the capillaries which run along the length of the stacking tube. The tubes with the red outline represent the supporting tubes which are only a fraction of the length of the stacking tube. At this stage all the constituents of the stacking tube are supported by a central support tube. (b) The cross-section of the stacking tube which is on the order of centimetres. (c) The cross-section of a cane/preform which is on the order of millimetres. Note that all the support tubes have been removed from the structure and the capillaries have fused with the tube surrounding them. (d) The cross-section of the final fibre which is on the order of micrometers. It is essentially identical to (c) except for the outer diameter and the fact the resonators have been inflated.

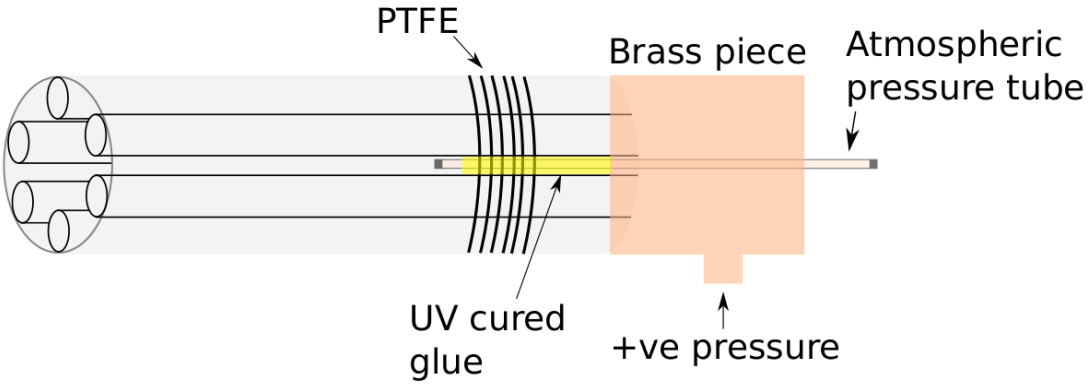


Figure 2-11: Schematic of a preform. The outer diameter generally spans millimeters and the length approximately 1 m. The difference between a cane and a preform is that a preform is a cane that is ready to be drawn to an optical fibre. The components which a preform has is the atmospheric pressure tube which goes through the core of the preform. High-temperature UV cured glue which goes around the atmospheric pressure tube and seals the area around it, including the spaces between the tubes. PTFE tape which acts as a thread for the brass pieces on the same end as the glued side of the preform. Lastly the brass pieces with an inlet for pressure to inflate the tubes during the fibre drawing stage.

of the stack tube with the support tubes missing since they are no longer necessary as the capillaries are now fused to the cladding, after the stack was passed through the furnace. Before drawing the canes into fibres the canes must be built into preforms (see figure 2-11). Preforms are the penultimate structure of the process. Here one of the ends cane has its central "core" region filled with high-temperature UV curing glue. A tube is placed in the core before curing which is used to keep the centre of the structure at atmospheric pressure during the draw. Around the glued end of the cane, brass pieces, one with an inlet for gas flow, is screwed onto the glass structure with PTFE tape used as the seal. The top brass piece, which has an open top to allow the atmospheric tube to go through it, is covered with glue to prevent any external gas flowing into the structure with the exception of the atmospheric pressure. With the preform built the final stage of fabricating the optical fibre can start.

The outer diameter of a typical HCNCF is of the order of hundreds of microns. The cross-section looks very similar to that at the cane stage with the exception that the

tubes are inflated, reducing the spacing between them and consequently also reducing their wall thickness (see figure 2-10(d)). There are two primary ways to increase the outer diameter of the tubes, firstly there is the active pressurisation which relates to the method described here from the cane to preform (Yu 2013). In this scenario pressure is applied to the tubes through the inlet of the brass piece. Since the core is sealed off with glue, the pressure will pass through the tubes and cause them to expand in the furnace region. The alternative method is to apply a vacuum to the core, thus, reducing the pressure in the core to where it is less than that in the tubes. The pressure differential causes the tubes to expand.

In summary creating a HCNCF is about drawing down a large version of the fibre to the desired size. Calculating the required draw parameters to achieve this is vital to obtaining a successful outcome. The conservation of volume is the principle used in order to calculate the required speed in which the preform is fed into the furnace and also the speed at which the drum is going to pull the optical fibre. The conservation of volume for two cylindrical structures is given by,

$$L_0\pi\left(\frac{d_0}{2}\right)^2 = L_1\pi\left(\frac{d_1}{2}\right)^2$$

where $L_0(L_1)$ is the length of the preform(fibre) and $d_0(d_1)$ is the outer diameter of the preform(optical fibre). Taking the derivative of the length with respect to time yields the velocity, $dL/dt = v$.

$$v_0\left(\frac{d_0}{2}\right)^2 = v_1\left(\frac{d_1}{2}\right)^2 \tag{2.22}$$

From equation (2.22) the speed at which to draw the fibre for known outer diameters can be calculated.

As described by equation (2.7) when designing a fibre to guide in the VUV the wall thickness of the tubes are significantly thinner than HCNCFs designed for visible or in-

frared wavelengths. For example, to build an optical fibre to guide 185 nm between the first and second resonance ($m = 1.5$), the wall thickness required is 110 nm ($n = 1.59$). Commonly an optical fibre for this wavelength will also have an outer diameter of the order of tens of microns. Therefore, the typical draw-down ratio (outer diameter of the preform to the outer diameter of the optical fibre) will be in the hundreds. The stress imposed on the glass through this large draw-down ratio is what makes manufacturing a VUV guiding optical fibre directly from a fibre so challenging. Stress is defined as,

$$S = \frac{F}{A} \tag{2.23}$$

where $S$ is the stress, $F$ is the tension and $A$ is the cross-sectional area of the optical fibre. When drawing the fibre it is important to draw it as quickly as possible with the furnace temperature being as low as possible. Being as close to the maximum tensile strength is optimal to prevent the tubes from collapsing under their own surface tension (White et al. 1962). Therefore, from equation (2.23) the stress increases due to a reduction in the cross-sectional area of the optical fibre given a constant tension. This is where the large draw-down ratio becomes counter-productive as the fibre will be close to the maximum tensile strength but the preform will not. The glass will not be drawn at its optimal stress level in order to prevent the tubes from collapsing. Moreover, the tubes do not collapse uniformly. Some will collapse more than others depending on the temperature profile of the furnace which is seldom constant across the hot zone. Inflating tubes of different outer diameters at a constant pressure will result in the fibre's tubes to be of different outer diameters and therefore different wall thicknesses which will result in a poorly performing optical fibre. In order to reliably build a HCNCF for the VUV another technique needs to be used, which in this case is tapering (section 2.3).

In summary manufacturing a HCNCF is about reducing a macroscopic structure down to it microscopic equivalent. However, although the process is straightforwards there

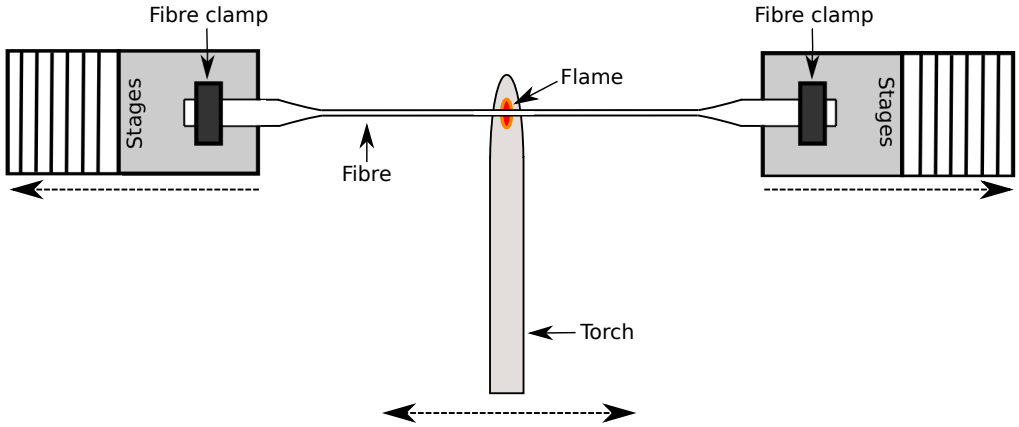


Figure 2-12: Schematic of the taper rig. The fibre is made taught on two stages (grey) which move in opposite directions. Simultaneously, a torch (yellow) sweeps a flame (red) underneath the sample (black horizontal line in between the stages) in both directions thinning the fibre. This has the effect of replicating the fibre on a smaller scale by drawing it down further allowing for the guidance wavelength to be shortened in the case of a HCNCF.

are some nuances to the stack and draw technique which highlights some common problems that occur when producing these fibres.

## 2.3 Tapering, a post-processing technique

As mentioned in section 2.2 manufacturing a HCNCF directly from a fibre tower to guide in the VUV is very challenging. To overcome this difficulty a process known as fibre tapering can be used. The technique is essentially an extension to the fibre tower. The ends of an optical fibre sample are clamped on two stages separated by a certain distance, keeping the fibre taut. A flame is then moved underneath the optical fibre. The flame starts to sweep underneath the sample whilst the stages, where the ends of the fibre is clamped, will simultaneously retract from each other (figure 2-12). The resulting optical fibre should be the same as that of untapered fibre but drawn-down to a smaller outer diameter, allowing for the creation HCNCF with walls too thin to be produced on a fibre drawing tower. The careful control of the flame's temperature and sweeping speed and also the speed at which the stages move apart allows for fine tuning of the tension during tapering. This is the main advantage of using optical fibre

tapering. Unlike the fibre tower where the draw parameters are kept constant, a taper rig is a multi-stage process. Each stage can comprise of a different flame sweeping speed and the speed at which the stages retract from one another. Therefore, as the fibre gets drawn-down it can be kept close to the maximum tensile strength which best preserves the shape of the internal structure (Birks and Li 1992).

### 2.3.1 Ratio conservation

In section 2.3 the final stage of producing a VUV guiding HCNCF was discussed. An effect that needs to be taken into account whilst tapering, unlike of the fibre drawing tower, is preventing the collapse of the tubes under their own surface tension. The pressure caused by the surface is defined as (Tabor and Tabor 1991),

$$P_{st} = \frac{\gamma}{r} \tag{2.24}$$

where $P_{st}$ is the pressure experienced on the tube caused by the surface tension, $\gamma$ represents the surface tension and $r$ is the radius of the tube. The surface tension acts like a negative pressure inside the tube trying to collapse it. Equation (2.24) shows that the smaller the tube the greater the pressure on it trying to collapse it. The collapse is slowed by the viscosity of the glass which is why the tension on the sample needs to remain as close to the maximum tensile strength as possible, as the viscosity is at its highest whilst the sample is still soft enough to be tapered.

In order to quantify the quality of the taper, certain aspect ratios of the original and tapered samples should remain constant. For example the ratio between the core diameter and the resonator outer diameter. Figure 2-13 shows two optical fibres. On the left is the original one and on the right its tapered counterpart. The ratios are calculated from the resonator diameter $d_{\text{tube}}$ and the core diameter $D$. The following results are $d_{\text{tube}}/D = 0.25 \pm 0.03$ for the original fibre and $d_{\text{tube}}/D = 0.23 \pm 0.01$

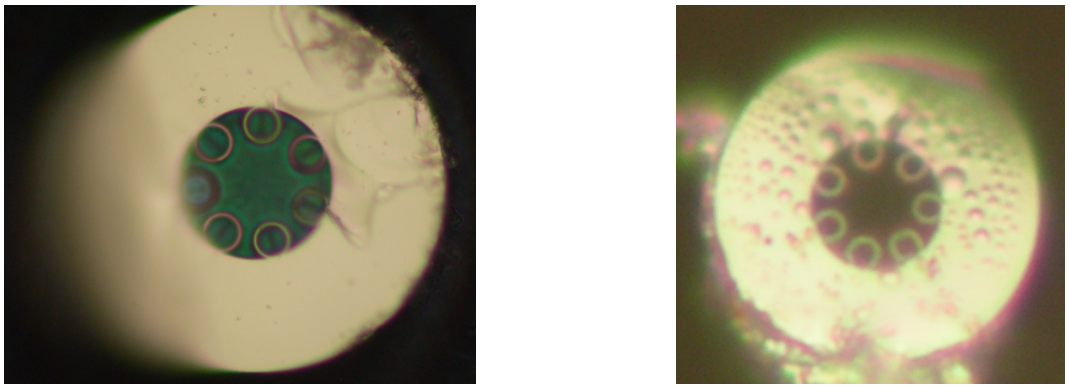

(a) (b)

Figure 2-13: Optical micrograph images of a 7 ring HCNCF's cross-section used to calculate the aspect ratio between the outer tube diameter $d_{\text{tube}}$ and the core diameter $D$. (a) Original fibre with an outer diameter of approximately 130 µm and an aspect ratio of $d_{\text{tube}}/D = 0.25 \pm 0.03$. (b) The same fibre as in (a) but draw-down to an outer diameter of approximately 23 µm and an aspect ratio of $d_{\text{tube}}/D = 0.23 \pm 0.01$ (draw-down = 5.6).

for the draw-down version. From the results it can be seen that the ratios are similar within measurement uncertainty, therefore indicating that the tubes may have not collapsed during tapering. The uncertainty comes from measuring the ratio for each resonator and then calculating the standard deviation. However, it must be noted that the calculations of these ratios is only as accurate as the quality of the image under scrutiny. So, it is important before relying on the result that the picture of the fibre's cross-section is of the highest possible resolution. However, practically speaking while tapering using a microscope is the most time-efficient way to calculate the ratios. Using high resolution imaging methods such as a scanning electron microscope (SEM) is not feasible when configuring the tapering stage due to the length of time an SEM image takes as the calibration of the tapering process may need 10s of samples.

# Chapter 3

# Multimode hollow-core negative curvature fibres

Many applications benefit from having a single-mode fibre as the beam quality is high and thus the far-field profile of the fibre's output is well known. However, there are many applications which benefit from an increase in power that is being transported in an optical fibre. For example, high power lasers which are typically multimode would benefit from a hollow-core multimode fibre since coupling efficiency would be high due to the shape and size of the laser modes matching those of higher-order modes in the optical fibre. Furthermore, multimode fibres would improve the signal to noise ratios in experiments where the signal is low as more modes means more light, assuming a multimode source. This chapter focuses on the development of multimode HCNCF for the ultimate goal of VUV transmission. It must be noted that in this chapter I personally did all of the work presented except for deriving equations (3.5) and (3.7).

## 3.1 Counting modes

In section 2.1.1 it was discussed that a standard step-index fibre is single-moded when its normalised frequency, $V$, is less than 2.405 (equation (2.16)). Therefore, meeting this condition can be done by varying the size of the refractive index step between core and cladding, increasing the core radius or reducing the guided wavelength. The number of guided modes in this type of optical fibre can be calculated exactly. However, as previously discussed due to the reversed refractive index profile of a HCNCF the number of 'modes' cannot be calculated exactly. Instead to obtain a single mode HCNCF the physical ratios presented in (Uebel et al. 2016) must be met in order for the higher modes to decay significantly faster than the fundamental mode. One of those ratios is $d_{\text{tube}}/D \approx 0.68$, where $d_{\text{tube}}$ is the diameter of the tube and $D$ is the diameter of the fibre's core. This ratio can be simply broken by adding more tubes to the fibre but keeping their diameters and the spacing between them constant. This process would increase the core diameter of the fibre and therefore $d_{\text{tube}}/D < 0.68$. Since there is no analytical formula which explicitly outputs the number of modes in a HCNCF because no mode in this structure is truly guided, in the sense that the inequality (2.14) is not met. Therefore a different metric needs to be used in order to quantify the number of modes in a HCNCF.

We know from a standard step-index fibre whose physical parameters are known that the number of modes follows the proportionality,

$$N_{\text{modes}} \propto a^2 \tag{3.1}$$

where $a$ is the core radius of the optical fibre. In the case of a HCNCF we suppose that,

$$N_{\text{HCNCF}} = a^x \tag{3.2}$$

where $N_{\mathrm{HCNCF}}$ represents the number of modes in a HCNCF, and $x$ is the constant of proportionality that needs to be determined. It is expected that the relationship will be of this form as the number of modes should scale with the cross-sectional area, so $x = 2$ (Uebel et al. 2016). Since there is no analytical result describing the behaviour of the electromagnetic fields in the guiding region of these fibres, the answers need to be calculated numerically. The finite element method, using COMSOL Multiphysics software, is an optimal method for this purpose as this technique is ideal when solving physical problems with complicated structures where an analytical result is absent (Jin 2015). The models represented in figure 3-1 were discretised into segments of varying size which depend on the complexity of the local structure. The mesh style used was free triangular so the radial and azimuthal results from the model were captured. At the boundaries of these meshed regions local solutions to Maxwell's equations were obtained. At the end of the process the individual modal properties were extracted (e.g. their complex propagation constant $\beta$ and their mode intensity profiles). The only difference between the fibre models in figure 3-1 are the number of tubes. Since the size and space between the tubes was to remain constant, adding more of them results in a larger core. Hence, if the number of modes could be deduced then the constant $x$ can be calculated.

Four different fibre designs were simulated (figure 3-1). The number of tubes in the fibres were 10, 15, 20 and 25. The fixed parameters as a function of wavelength $\lambda$ was the ring wall thickness, $0.90\lambda$, the outer tube radius $5.5\lambda$ and the gap between them, $3.8\lambda$ (defined as distance from the outer wall of the ring to the outer wall of the neighbouring ring). Increasing the number of tubes whilst keeping the spacing between them constant increases the core diameter. In terms of wavelength the core diameter of the 10 ring fibre was $37\lambda$, for the 15 ring fibre, $60\lambda$, for the 20 tube fibre, $83\lambda$ and for the 25 tube fibre, $110\lambda$. These fibres followed a fibre designed for infra-red wavelengths which was multimoded (Love 2018). The quadrants in the cladding represents a perfectly matched

layer (which for computational efficiency requires a boundary-style of meshing). This layer allows the waves to decay exponentially as it travels through it simulating a radiation mode (Bérenger 2007). A scattering boundary condition was placed on the outer edges of the structure to ensure that no wave is reflected back into the core (Frei 2015). The distance between the inner jacket boundary and the start of the perfectly

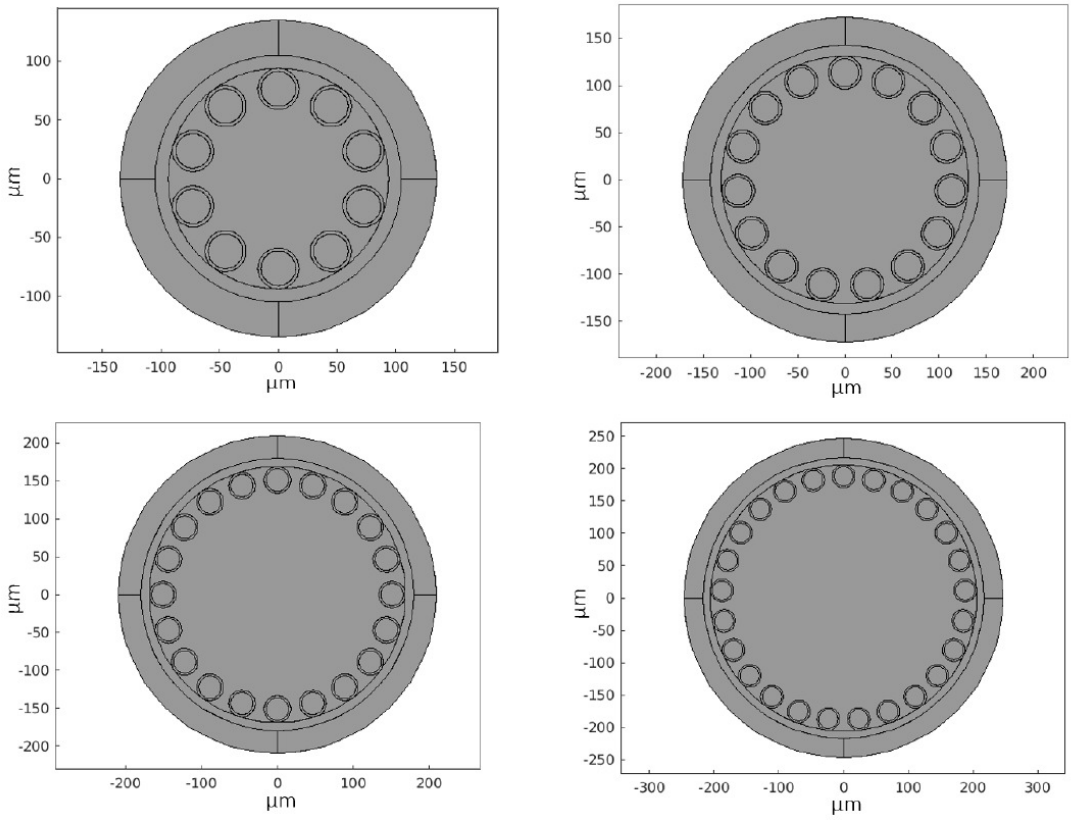


Figure 3-1: The models of the fibres used to calculated the number of modes as a function of core radius. All the parameters are constant with the exception of the number of tubes and hence the core radius. From the top left to the bottom right the number of tubes ranged from 10 to 25. The following parameters are represented in terms of wavelength $\lambda$, starting with the top left. The wall thickness $0.9\lambda$, the outer resonator radius $5.5\lambda$ and the gap between them, $3.8\lambda$ (defined as the outer wall of the resonator to the next nearest outer wall). $\lambda/D = 37$ (10 tubes), $\lambda/D = 60$ (15 tubes), $\lambda/D = 83$ (20 tubes) and $\lambda/D = 110$ (25 tubes) where $D$ is the core diameter. The quadrants on the outside of the cladding represent a perfectly matched layer. The thickness of the cladding is chosen such that the light will not reflect back into the core from the boundary of the model. This is further ensured by the addition of a scattering boundary condition at the perimeter of the model.

matched layer was chosen such that it is not antiresonant and therefore not reflecting waves back into the core.

As previously discussed, modes in a HCNCF are not truly guided and hence, are not equivalent to those found in a step-index fibre. Instead of a defined number of 'guided' core modes, many modes are confined in the core with their only difference being that their attenuation is considered too 'high'. This implies that to calculate the number of modes in the core a loss threshold needs to be introduced. The number of modes are those which have a loss below that threshold. To ensure that no modes were missed the system was set to solve for 1000 modes with an effective refractive index just below 1, allowing for core modes to be found.

From equation (3.2) it can be seen that $x$ is simply calculated from

$$\log(N_{\text{HCNCF}}) = x \log(a) \tag{3.3}$$

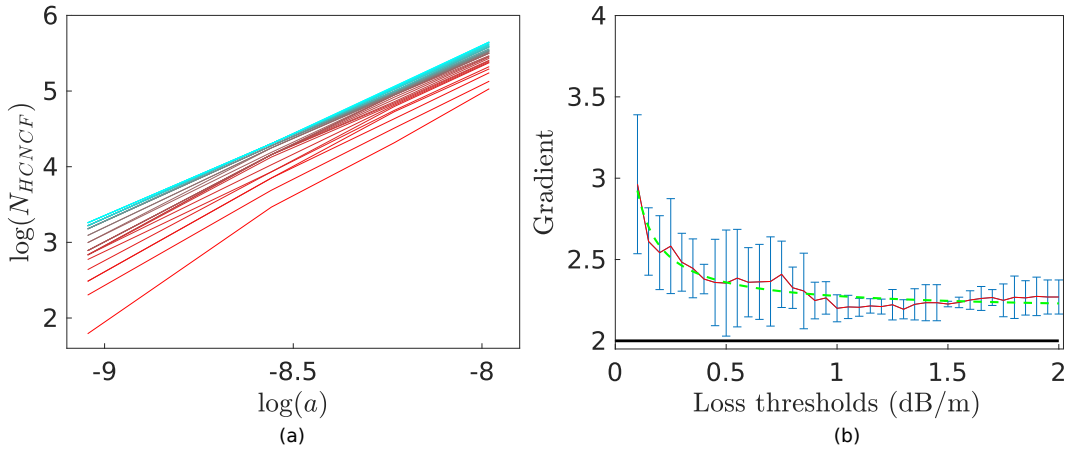


Figure 3-2: (a) 38 solutions of loss thresholds between 0.1 to 2 dB/m in steps of 0.05 dB/m. The colour gradient shows red as low-loss and light-blue as high-loss. (b) The gradient measurement of all of the solutions of (a). The error bars arise from the solutions in (a) showing the standard deviations of the gradient (2-point difference) as not all of the solutions are linear. The solid black line shows the result from a step-index fibre. The dashed-green curve represents the fitted result which is in the form of a power-law.

Hence if the gradient from the curve which describes equation (3.3) can be found then the increase in the number of modes as a function of area for a given loss threshold can be calculated. Figure 3-2(a) shows the results for a loss threshold range of 0.1 to 2 dB/m in steps of 0.05 dB/m. The error bars represent the standard deviation of the gradients which arise by measuring the 2-point difference between the individual points in figure 3-2(a). The lines are not parallel, which means that $x$ is not simply a constant but is a function of the loss threshold. The lines are also not straight so there is a range of values for $x$ for a given loss threshold. A curve was fitted (equation (3.4)) to the results in order to interpolate a value for $x$. The gradient measurement shows (figure 3-2(b)) that for all results the number of modes increase more rapidly than $x = 2$. Therefore, it appears that from these simulations a HCNCF generates more modes as a function of core diameter than a standard step-index fibre. If this were to be a conjecture the result also makes sense as the larger the core the fewer bounces per unit length and therefore a reduction in the loss. In addition the larger the core the smaller the propagating angles because $\beta$ increases due to a larger effective refractive index which also contributes to a smaller number of bounces, and therefore interactions with the glass, per unit length.

Visually inspecting figure 3-2(b) it appears that the relationship between the gradient and core size follows a power-law in nature. Since the actual analytical formula is unknown an power-law curve was fitted as an empirical guide for interpolation purposes,

$$x = a{L_{\mathrm{TH}}}^{b} + c \tag{3.4}$$

where $L_{\mathrm{TH}}$ is the loss threshold and $a$, $b$ and $c$ are constants to be determined. They were found to be $a = 0.10 \pm 0.06$, $b = -0.87 \pm 0.24$ and $c = 2.2 \pm 0.1$. This curve is the dashed green line in figure 3-2(b).

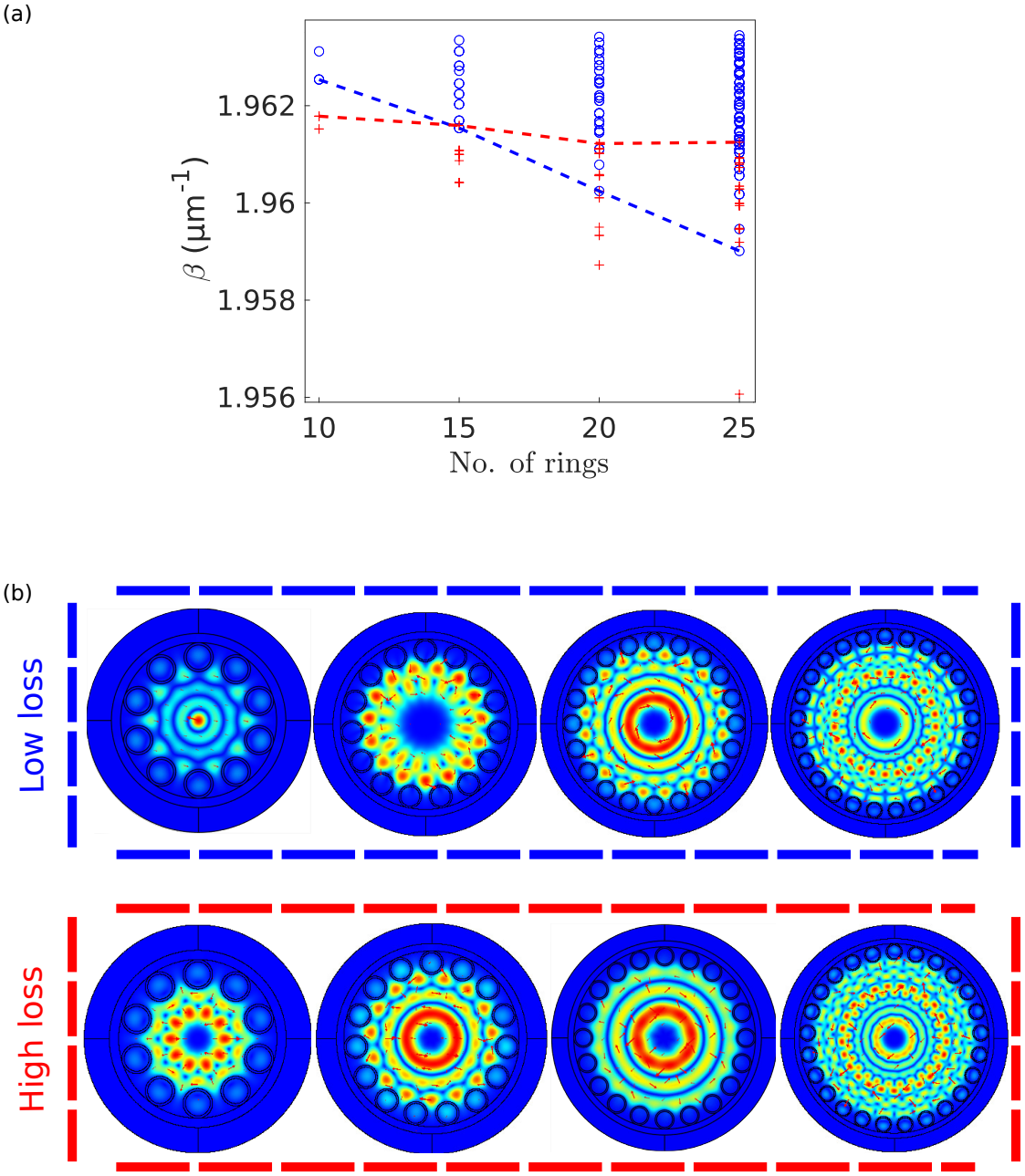


Figure 3-3: (a) Propagation constant $\beta$ for modes with a loss threshold of less than 0.1 dB/m (blue) and for modes with a loss between 0.1 dB/m and 0.2 dB/m (red). The blue-dashed line traces minimum $\beta$ for modes with a loss of less than 0.1 dB/m and the red-dashed line follows the maximum $\beta$ for modes with a loss threshold between 0.1 and 0.2 dB/m. (b) The modal profiles of those being traced by the blue-dashed line (top row) and red-dashed line (bottom row). The red-arrows on the modal profiles represent the polarization of the electric field.

So far the arguments have been solely focused on counting the number of modes below a certain loss threshold. However, as shown in figure 3-3, when comparing the propagation constant $\beta$ of the surviving modes an interesting result is found. Some higher-order modes have a greater value of $\beta$ than the lower-order modes. $\beta$ is a discrete variable where the greater the value of $\beta$ the lower the order the mode is, with the fundamental mode having the largest value of $\beta$. Higher-order modes by nature of there propagation angle interact more with the tubes of the HCNCF and are therefore more lossy. However, the higher-order modes which have a greater $\beta$ value than lower order modes were found to be more transverse-magnetic-like as the polorization of the electric field near the tubes are more perpendicular to the tubes, whilst the lower-loss lower $\beta$ value modes are more transverse-electric-like as their fields near the tubes are more parallel to the tube walls. Transverse-magnetic modes are more lossy than their transverse-electric mode counterparts as seen from equations (2.9) and (2.10).

The results shown thus far rely on using numerical methods. However, some approximate models which revolve around treating these fibres as a Bragg fibre can be used to obtain the number of guided modes below a certain loss threshold (Bird 2017). From this study the attenuation of HE/EH modes in dB which is incurred in propagation through a distance of one wavelength $\lambda$ is given by,

$$\alpha_\lambda = 8.686 \left(\frac{x_0}{2\pi}\right)^{N+2} \frac{1}{2} \frac{n^{2N+2}+1}{(n^2-1)^{(N+1)/2)}} \left(\frac{\lambda}{r_c}\right)^{N+3} \tag{3.5}$$

where $x_0$ is the $m$th (non-trivial) zeros of the Bessel function of the $J_{p-1}$ and $J_{p+1}$ for $\mathrm{HE}_{pm}$ and $\mathrm{EH}_{pm}$ modes respectively. $N$ is the number of antiresonant layers in the structure, $n$ is the refractive index of the glass and $r_c$ is the core radius. Equation 3.5 assumes the layers in the structure are perfectly antiresonant, i.e. $\sin^2(\phi_i) = 1$ (the width of each layer in the structure is at the anitresonant width, section 2.1).

Following the derivation by Prof Tim Birks, if we let $G = V^2/2$ be the number of modes (including polarised states), where $V$ is the normalised frequency and rewriting equation (2.11) so the attenuation per unit distance of wavelength can be given as,

$$\alpha_\lambda = C_N^{-\left(\frac{N+2}{2}\right)} G^{\left(\frac{N+2}{2}\right)} \left(\frac{\lambda}{r_c}\right)^{N+3} \tag{3.6}$$

where the dimensionless quantity $C_N$ is solely dependent on the value of the refractive index and number of antiresonant layers $N$. Rearranging equation (3.6) to make the number of modes $G$ the subject (Winter, Birks and Wadsworth 2019),

$$G = C_N \left(\frac{r_c}{\lambda}\right)^{2\left(\frac{N+3}{N+2}\right)} \alpha_\lambda^{\frac{2}{N+2}} \tag{3.7}$$

For realistic designs of HCNCF the number of antiresonant layers, $N$, is about 3. Using this value as a guide, we have $r_c^{2.4}$ agreeing with the numerical simulations that HCNCFs excite more modes than a standard step-index optical fibre. Hence, using this model of optical fibre to guide many modes is well founded as it also agrees well with the numerical simulation results.

## 3.2 Fabricating a multimode hollow-core negative curvature fibre

The discussion so far has revolved around the theoretical implications of a multimode HCNCF. However, manufacturing one involves a different set of problems that need to be solved. The primary issue is controlling the tolerance on the capillaries. The tolerance is defined as the maximum deviation allowed on the outer diameter of the capillary from the ideal outer diameter. For example, for a standard single-mode fibre (6 to 8 tubes) a typical tolerance would be 8 µm, so for example a target capillary outer diameter of 1.500 mm, could be drawn to a minimum outer diameter of 1.492 mm. Using an example of a 8 tube fibre the tolerance would mean that one could expect a

maximum spacing of 128 µm in the stack (16 tubes in the stack due to the supports). This is a manageable target to reach as the final spacing in the stack will still lead to high quality optical fibres. However, when considering a multimode fibre the tolerance starts to become significantly tighter.

The optical fibre that was manufactured for this task was a 22 tube HCNCF. A 22 tube fibre would have had 44 tubes in the stack. Following the guide of a total tolerance of 128 µm would mean that the maximum tolerance on each capillary was about 3 µm. This reduction in tolerance was difficult to achieve, however, there were two primary conditions that needed to be filled. Firstly, the drawing of the capillaries needs to be done at a very high tension, which means keeping the furnace *cold* and drawing the capillaries quickly. Secondly, the quality of the starting tube needs to be very high. The maximum standard deviation of the outer diameter along the length of the tube should not exceed 0.01 mm, which is the minimum deviation that is provided by the tube suppliers.

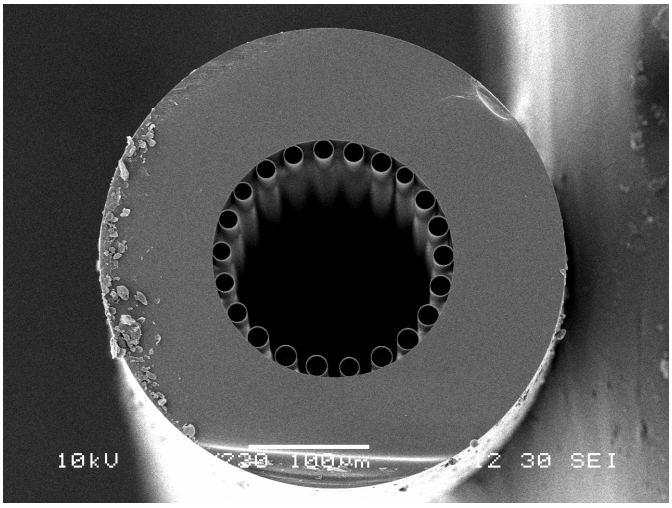


Figure 3-4: SEM of the cross-section of the 22 tube HCNCF. The physical parameters are as follows, outer diameter 386 ± 2 µm, resonator outer diameter 17.2 ± 1 µm, core diameter 164 ± 2 µm and a tube wall thickness is 532 ± 10 nm. (Winter, Birks and Wadsworth 2019)

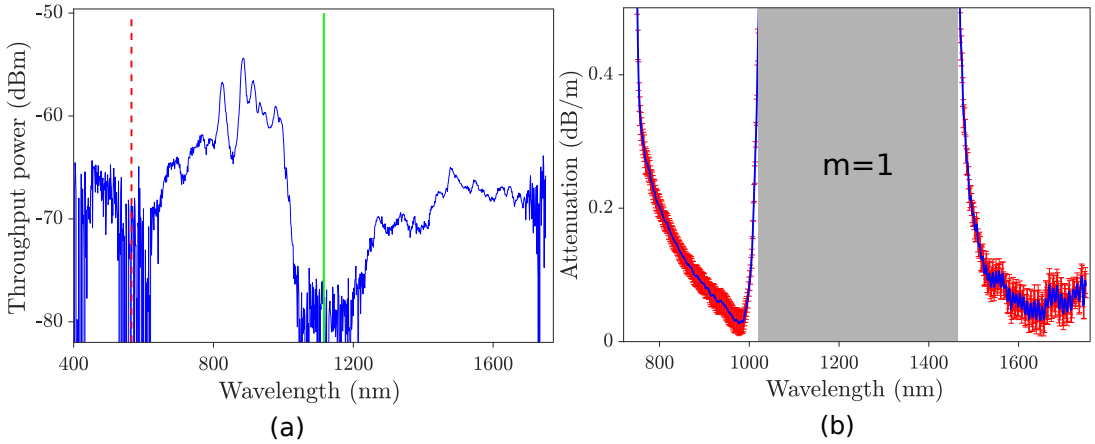


Figure 3-5: (a) Short-piece (approximately 15 cm) transmission of the 22 tube HCNCF. The $m = 1$ at 1120 $\pm$ 28 nm and $m = 2$ at 565 $\pm$ 14 nm. Resonances for a tube wall thickness of 532 $\pm =$ 10 nm are represented by solid (green) and dashed (red) vertical lines respectively. (b) Cut-back measurement from 25 m to 10 m. The minimum loss between the $m = 1$ and $m = 2$ resonance is 0.03 $\pm$ 0.01 dB/m at a wavelength of 970 nm.

For drawing the fibre itself the technique follows the standard stack and draw method with the tubes actively pressurised during the preform to fibre stage. An SEM of the fibre's cross-section is shown is figure 3-4. The stress on the glass during the final stage was 3.51 kg/mm$^2$. The resultant fibre had an outer diameter of 386 $\pm$ 2 µm, the tubes outer diameter was 17.2 $\pm$ 1 µm and the fibre's core diameter was 164 $\pm$ 2 µm (Winter, Birks and Wadsworth 2019).

Figure 3-5 shows the transmission performance of the 22 tube optical fibre with a wall thickness of 532 $\pm$ 14 nm (measured from the $m = 1$ resonance). The set-up used for the short piece transmission consisted of a Xenon lamp whose output was coupled into a patch cable which was butt-coupled (fibre cross-section to fibre cross-section) to the sample fibre. The output of the sample was then butt-coupled into another patch cable which was then connected to a spectrometer. For the cut-back result the set-up was identical except that the initial patch cable was removed and the output of the Xenon lamp was coupled directly into the fibre using mirrors. Near-field images were taken with a CCD camera to ensure the light was propagating in the core of the optical

fibre. The vertical lines on the short piece transmission shows the predicted location of the $m = 1$ (solid, green) at 1115 nm and $m = 2$ at 565 nm (dashed, red) resonances for a tube wall thickness of 532 nm. The cut-back measurement was taken from a long length of 25 m to 10 m. The minimum loss between the $m = 1$ and $m = 2$ resonances is $0.03 \pm 0.01$ dB/m. The low confinement loss is contributed by the core to wavelength ratio which at 970 nm (the location of the minimum loss) is 169.

The low confinement loss of the fibre shown in figure 3-5 is expected due to the quality of the fibre as seen from the SEM image and also the large core relative to the sampled wavelengths. However, the advantage of optical fibres in general is also the ability to bend light. It is therefore expected that due to the inverse relationship between confinement loss and bend loss that a large bend loss might be expected for this optical fibre. Figure 3-6 shows the bend loss performance of this optical fibre. The set-up used was similar to that in figure 2-8(b) (bend at the end) in order to include the higher-order modes in the loss measurements. Figure 3-6(a) represents the bend loss for the two wavelengths, 980 nm and 1630 nm. The former wavelength lies between the $m = 1$ and $m = 2$ resonances with the latter being between $m = 0$ and $m = 1$. At 980 nm the loss starts to increase from a bend diameter of 30 cm, and when compared to the result

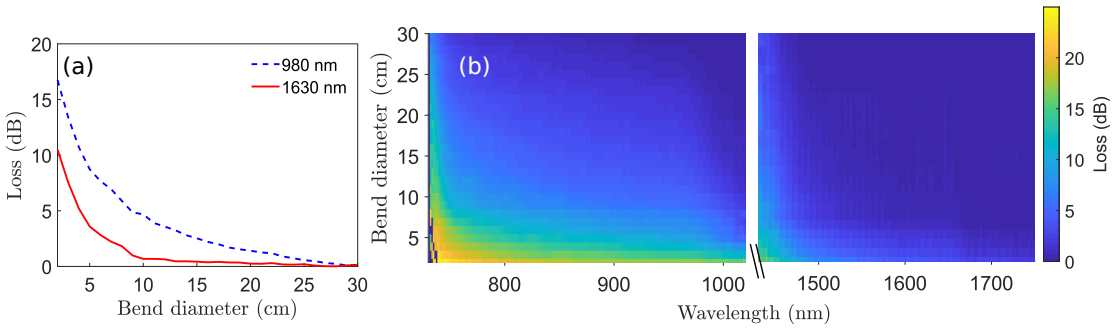


Figure 3-6: (a) Loss versus the bend diameter in centimeters for 180° bends for two wavelengths 980 nm and 1630 nm which exist between the $m = 1$ and $m = 2$ and for wavelengths longer than that at the resonance respectively. (b) Intensity plot of the loss in dB for a bend diameter for a given wavelength. The break in the wavelength axis is the omission of the $m = 1$ resonance.

at 1630 nm where the loss increase is delayed until a bend diameter of approximately 10 cm. Physically this is expected due to the dependencies of wavelengths relative to the core diameter. The greater the ratio is between the core diameter to the guided wavelength the more modes are expected to exist as the structure is further away from the conditions for single mode guidance (Uebel et al. 2016). However, when the fibre is bent the light is forced to interact with a particular side of the optical fibre. This means that there are two contributing factors to the disparity between the losses. Firstly, the shorter wavelengths can more easily penetrate the gaps in between the tubes and couple into cladding modes and get lost. Secondly modes couple into each other due to phase matching as the fibre is bent because of the difference in the distances between one side of the core to the other which can cause mode loss (Gao et al. 2016, figure 2-6). This effect is of course more prevalent where there are more modes. Figure 3-6(b) shows an intensity spectrum for the loss in dB when the fibre is bent for a given wavelength. The spectrum shows what is expected from the bend loss models represented in (Marcatili and Schmeltzer 1964). The shorter the wavelengths the greater the loss for a given bend diameter. Furthermore, there is also an increase in the loss to the right of the resonances as bending effectively widens the resonance bands as there is an increase in the interaction between the light and the tubes wall, so high loss wavelengths are lost faster through bending. In terms of the applicability of multimode HCNCF the loss is tolerable for applications in high-power delivery. Improvements to the bend loss performance could also be made by reducing the spacing between the tubes by further inflation, thus minimising the interaction of the light with the cladding of the optical fibre.

Figure 3-7 shows two separate experimental set-ups to look at the near-field patterns that the fibre outputs. Figure 3-7(a) shows the set-up used to measure the near-field bend loss of this optical fibre. It consisted of a 980 nm diode whose output was coupled into the 22 tube optical fibre which was initially laid out in 1 m diameter loops with

the final 1 m length being used to induce the bend loss. The output of the fibre was then focused onto a CCD camera. Figure 3-7(b) shows the same set-up except with a 1.3 m length of fibre. The purpose of this experiment is to see if there is a difference output intensity profile of the fibre which would indicate that as a function of bend diameter the fibre is losing higher-order modes.

The near-field intensity profiles are represented in both figure 3-8 for the 10 m piece and figure 3-9 for the 1.3 m piece. Each row represents a certain bend radius for a half-bend turn. Each column represents an offset of 20 μm from the initial position (first column) horizontally across the fibre's core. Both figure 3-8 and 3-9 show the same result. The tighter you make the bend radius of the optical fibre the fewer modes will propagate. This is because higher-order modes interact more with the boundaries of

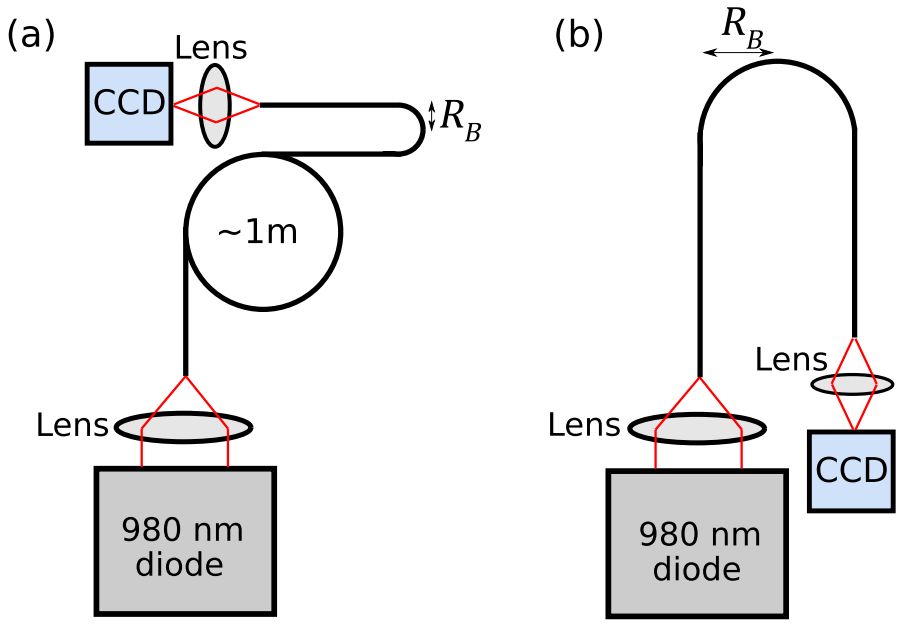


Figure 3-7: Set-up used to measure the far-field output of the optical fibre as a function of bend radius. Both set-ups consisted of a diode which emits 980 nm wavelength light. The output from the diode is focused into the core of the optical fibre. The output of the optical fibre is then focused onto a CCD camera. (a) Shows the set-up for a 10 m long piece of fibre, with the bend at the end to preserve the higher-order modes. Note that the fibre was laid out in loops with a diameter of approximately 1 m. (b) A 1.3 m length of fibre was used with a single half bend.

the core and so couple to radiation modes in the cladding leaving only the lower-order modes. Experimentally we should expect to see the size of the near-field pattern to reduce as the higher-order modes are filtered out as the bends get tighter. This is what we see in both figures as the radius of the blobs reduces with a reduction in the bend radius.

This chapter investigated the behaviour of multimode HCNCFs. It was theoretically shown through both finite-element analysis and an extension of the analytical method in (Bird 2017, derivation by Prof Tim Birks) that the number of modes for a given loss threshold scales faster with core radius in a HCNCF than in a solid-core fibre. Experimentally, it was also shown that a 22 tube HCNCF is highly multimode at a wavelength of 980 nm, where the core diameter to wavelength ratio is 167. It is shown qualitatively through bending the optical fibre and observing the near-field pattern. The radius of the near-field pattern got smaller as the bend radius of the fibre got tighter because higher-order modes coupled to radiation modes in the cladding. The loss performance of the 22 tube HCNCF also indicates that it is suitable for applications within high-power laser delivery from a multimode source and, moreover, the physical and optical properties of the 22 tube fibre make it an ideal candidate for VUV guidance once tapered (section 4.2.2).

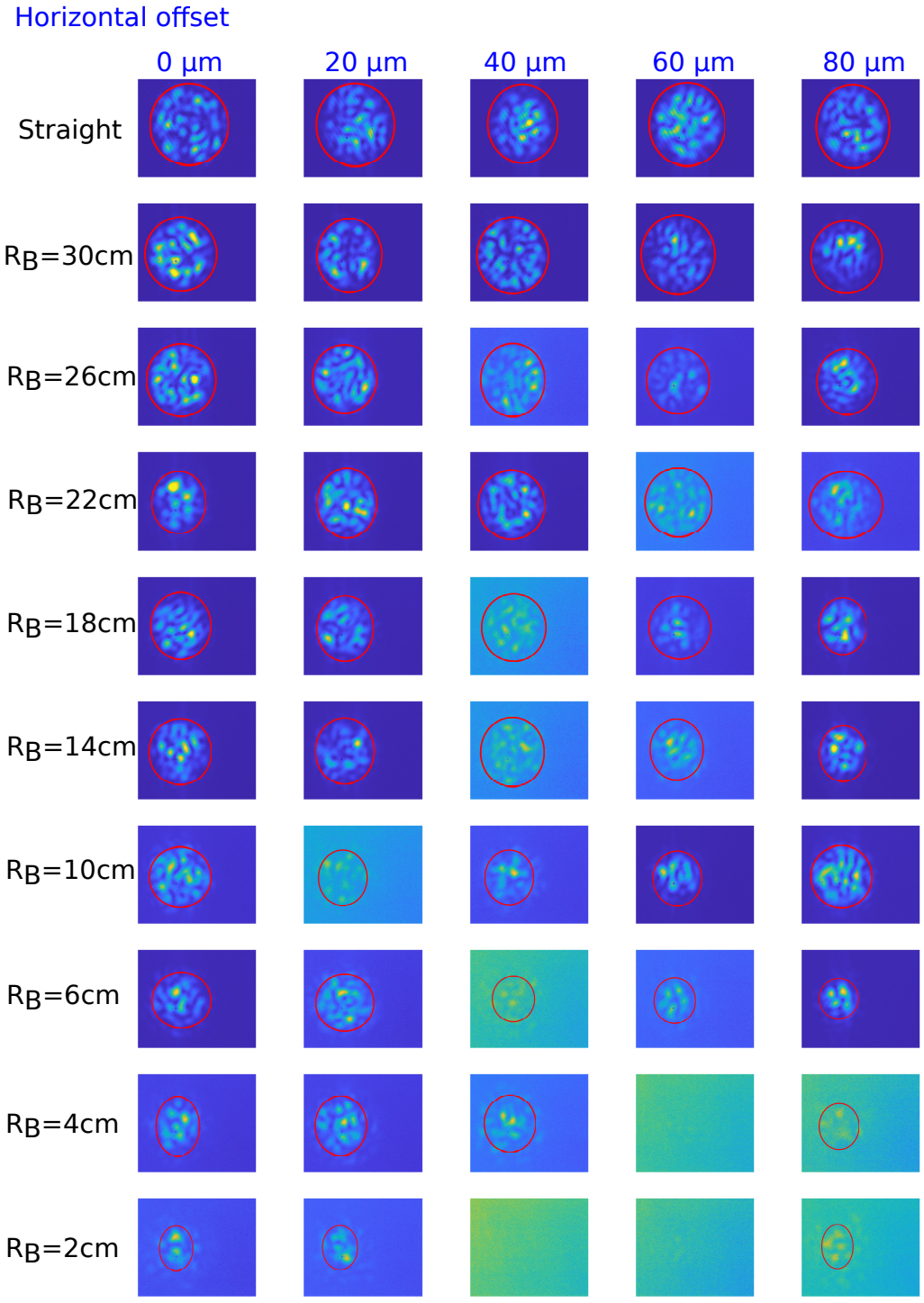


Figure 3-8: Near-field pattern for a 10 m piece of the 22 tube HCNCF. Each column represents an offset of 20 µm from the initial position (first column) horizontally across the fibre's core. The rows represent different bend radii $R_B$. The red ellipses represents the boundary of the near-field pattern. the mode The change in colour of the background is due to an increase in gain in the image.

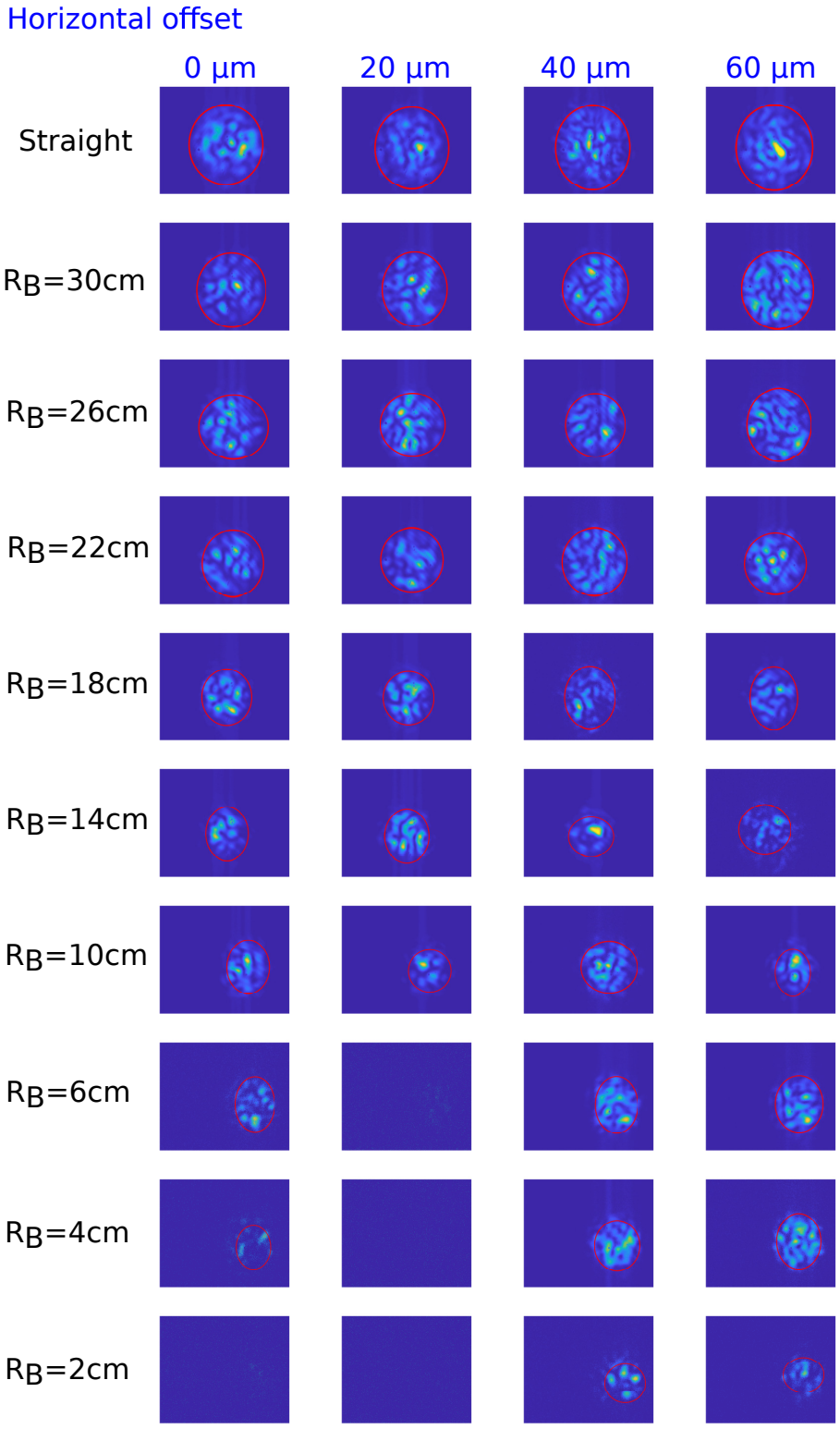


Figure 3-9: Near-field pattern for a 1.3 m piece of the 22 tube HCNCF. The rows represent different bend radii $R_B$. Each column represents an offset of 20 µm from the initial position (first column) horizontally across the fibre's core. The red ellipses represents the boundary of the near-field pattern.

# Chapter 4

# Band shifting and VUV guidance

It was discussed in section 2.1 that the transmission spectra of hollow-core negative curvature fibres consists of wide low-loss regions which are separated by narrow high-loss peaks known as resonances. The wavelength location of the resonances is determined by the thickness of the tubes in the HCNCF. To guide in the VUV the wall thickness needs to be extremely thin, for example to propagate a wavelength of 185 nm in between the first and second resonances the corresponding wall thickness is 110 nm. Producing this wall thickness directly from a fibre drawing tower is extremely difficult due to the stress imposed on the optical fibre (section 2.2). To overcome this issue the post-processing technique of tapering was suggested as a way to reduce the wall thickness of these optical fibres to a width not possible on a fibre tower (section 2.3). Reducing the wall thickness of a HCNCF will shift the resonances to shorter wavelengths and quantifying the amount in which the resonances shift will aid in the production of VUV guiding optical fibres. It must be noted that I solely performed all of the work presented in this chapter except for the experimental set-ups and results with regards

to VUV (< 190 nm) guidance where I worked alongside my collaborators from LASP (University of Colorado).

## 4.1 Fabry-Perot model

The Fabry-Perot etalon was used to model the transmission properties exhibited by the antiresonant effect (section 2.1). Although the insights provided by equation (2.2) for the output intensity as a function of the width of the cavity are useful, the model does exclude the material properties of the cavity. Furthermore, equation (2.2) assumed the light was traveling normal to the surface, but we know that one of the assumptions of antiresonant guidance is that the light traveling at grazing incidence to the surface as $D >> \lambda$, where $D$ is the HCNCF core diameter. This assumption leads to the derivation of equation (2.7) which would calculate the locations of the resonances for a given cavity width. Implementing grazing angle incidence into equation (2.2) results in the output intensity being,

$$I_{\text{out}} = \frac{I_{\text{in}}}{1 + \left(\frac{4R}{T^2}\right) \sin^2(k_0 d \sqrt{n_2(\lambda)^2 - 1})} \tag{4.1}$$

**Algorithm 1** Finding the location for a resonance for a given wall thickness

**procedure** RESONANCELOCATION(**int** $m$, **float** $\lambda$, **float** $\lambda_{\text{shift}}$, **float** $d_{\text{target}}$, **float** $d_{\text{error}}$)
    $d = (\lambda \cdot m/2) \cdot (1/\text{sqrt}(n^2 - 1))$
**while**(abs$(d - d_{\text{target}}) > d_{\text{error}}$):
    **if** $d_{\text{target}} > d$ **then**
        $\lambda = \lambda \cdot (1 + \lambda_{\text{shift}})$
        $n = \text{getRefractiveIndex}(\lambda)$
        $d = (\lambda \cdot m/2) \cdot (1/\text{sqrt}(n^2 - 1))$
    **if** $d_{\text{target}} < d$ **then**
        $\lambda = \lambda \cdot (1 - \lambda_{\text{shift}})$
        $n = \text{getRefractiveIndex}(\lambda)$
        $d = (\lambda \cdot m/2) \cdot (1/\text{sqrt}(n^2 - 1))$
**return** $\lambda$

where $I_{\text{in}}(I_{\text{out}})$ is the input(output) intensity, $R$ is the reflectivity of the surface, $T$ is the transmission of the surface (i.e. $T = 1 - R$), $k_0$ is the wavenumber, $n_2(\lambda)$ is the wavelength dependent refractive index of the material, $d$ is the width of the cavity and $\theta$ is the refracted angle that the light ray enters the cavity. Equation (4.1) contains the refractive index of the material and hence the behaviour of the resonances and the transmission bands in between can be studied as the wavelength gets reduced.

The resonance locations can be calculated from equation (2.7). However, as the refractive index is dependent on wavelength an iterative procedure needs to be implemented in order to calculate the location of the resonances. Algorithm (1) describes the procedure. In this case $m$ is the order of the resonance, $\lambda$ is the wavelength, $\lambda_{\text{shift}}$ is the percentage in shift of wavelength, $d_{\text{target}}$ is the target wall thickness and $d_{\text{error}}$ is the minimum deviation of the target wall thickness with the guessed wall thickness ($d$) to exit the while loop. $n$ is the refractive index which is calculated by function

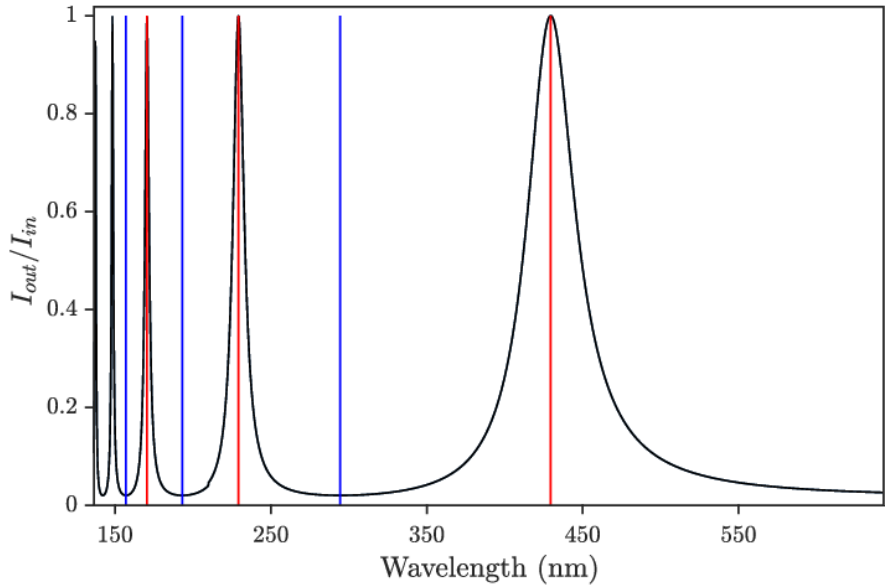


Figure 4-1: Example of a Fabry-Perot model transmission spectrum for a hollow-core negative curvature fibre covering three resonances. The tube wall thickness is set to 200 nm, the reflectivity $R = 0.75$ and the transmission $T = 0.25$. The red(blue) vertical lines represent the locations of the resonances(antiresonances). The resonances are located at 429 nm ($m = 1$), 229 nm ($m = 2$) and 170 nm ($m = 3$).

which returns the refractive index for a given wavelength. The procedure returns the wavelength location of the $m$th resonance for a given wall thickness.

Figure 4-1 shows an example of a transmission curve from the Fabry-Perot model for three resonances. The model's parameters are a wall thickness of 200 nm, reflectivity $R = 0.75$ and therefore transmission is $T = 0.25$. $R = 0.75$ was chosen as a value because it realistically represents the product of many grazing angle reflections from the light inside an optical fibre where an individual reflection may have $R_{single} > 0.9999$. The red(blue) vertical lines represent the locations of the resonances(antiresonances). The resonances are located at 429 nm ($m = 1$), 229 nm ($m = 2$) and 170 nm ($m = 3$). The Fabry-Perot model does not include the loss produced by the structure but the importance of studying the model is the behaviour of the resonances. The $m = 1$ and $m = 3$ resonances in figure 4-1 are 259 nm apart in wavelength. The ratio between the refractive index at these two wavelengths is $n(170\text{ nm})/n(429\text{ nm}) = 1.11$. This large difference means that the resonances are closer together than they otherwise would be if the refractive index were to remain constant. Therefore the $m = 2$ resonance should not be at half the value of the $m = 1$ resonance, which is seen as $229/429 = 0.534$, and that the $m = 3$ resonance should not be third of the $m = 1$ resonance, $170/429 = 0.396$. In this regime where the refractive index is non-linear, reducing the wall thickness will cause a non-linear shift in the resonance towards shorter wavelengths.

Within the VUV the refractive index starts to rise rapidly. Figure 4-2 demonstrates the effect of the position of the resonance with respect to the wall thickness of the structure. Starting with a wall thickness of 110 nm the wall thickness is reduced down to a wall thickness of 30 nm. The solid-red horizontal line is located at a wavelength of 190 nm and represents the boundary where the VUV starts. The most apparent feature of this result is the non-linear nature of it. Below approximately 170 nm the refractive index is increasing so fast that for every nanometer reduction in wall thickness, the dis-

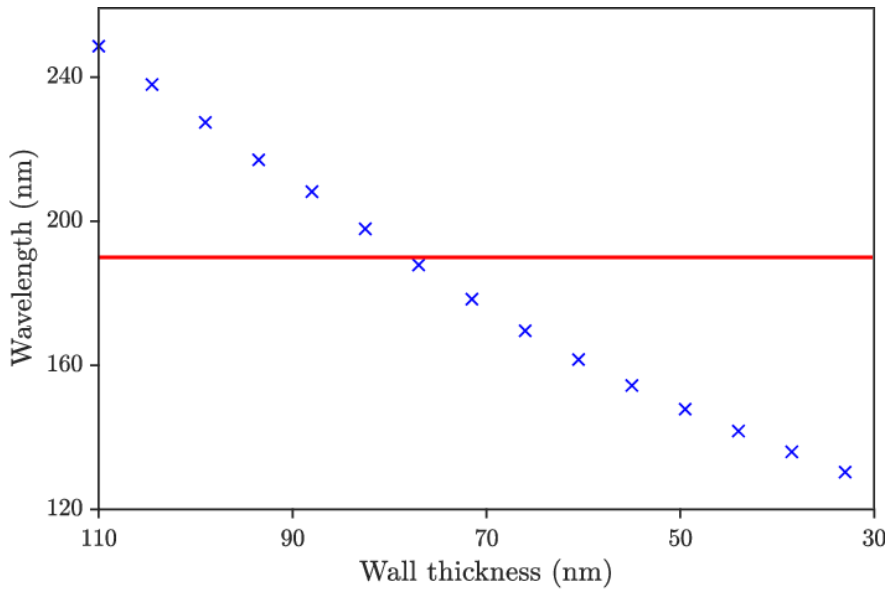


Figure 4-2: Tracking the location of the $m = 1$ resonance in wavelength with respect to the reduction in wall thickness. The wall thickness started at 110 nm and was reduced to 30 nm. The solid-red horizontal line is located at a wavelength of 190 nm and represents the boundary where the VUV starts.

tance between the location of the $m = 1$ between successive wall thicknesses becomes smaller. The large change in the refractive index, for VUV designed HCNCFs, due to a small reduction in wall thickness is seen when looking at the ratio $n(\lambda_2)/n(\lambda_1)$. For example, in the UV $n(238\text{ nm})/n(248\text{ nm}) = 1.00$, there is no change whilst in the VUV $n(136\text{ nm})/n(142\text{ nm}) = 1.07$ there is a significant change in the refractive index over a change in wall thickness of 5 nm.

Although the driving parameter in designing a HCNCF is the thickness of the tube when it comes to choosing which wavelengths to guide, the position of these wavelengths with respect to the resonance order also needs to be taken into account. In the VUV we have seen how the increase in the refractive index causes the first order resonances to bunch up with respect to the wall thickness of the optical fibre. However, practically speaking the bandwidth between resonances is crucial to maximise the number of wavelengths which are guided. Typically, in the regime where the refractive index is constant aiming

to guide the desired wavelengths between the $m = 1$ and $m = 2$ resonances or the $m = 2$ and the $m = 3$ resonances is reasonable as the separation between them spans hundreds of nanometers. Therefore the possible errors in the manufacturing process where it is challenging to calibrate the required wall thickness exactly during production becomes less significant. However, in the VUV the large refractive index constrains the guiding wavelengths to be between the $m = 1$ and $m = 2$ resonances or the $m = 0$ and $m = 1$ resonances (note that $m = 0$ extends to infinity). Understanding the compression of the spacing between the resonances is crucial as it gives an estimate as to what the behaviour of the transmission bands given the engineering constraints.

Figure 4-3 shows how the normalised frequency bandwidth between the $m = 1$ and $m = 2$ resonance shrinks due to the increase in the refractive index. Here $f_1(f_2)$ is the frequency at the $m = 1(m = 2)$ resonance. $\Delta f$ is the difference between $f_1$ and $f_2$. The frequency bandwidth is normalised by $f_1$. The analysis starts with a wall thickness of

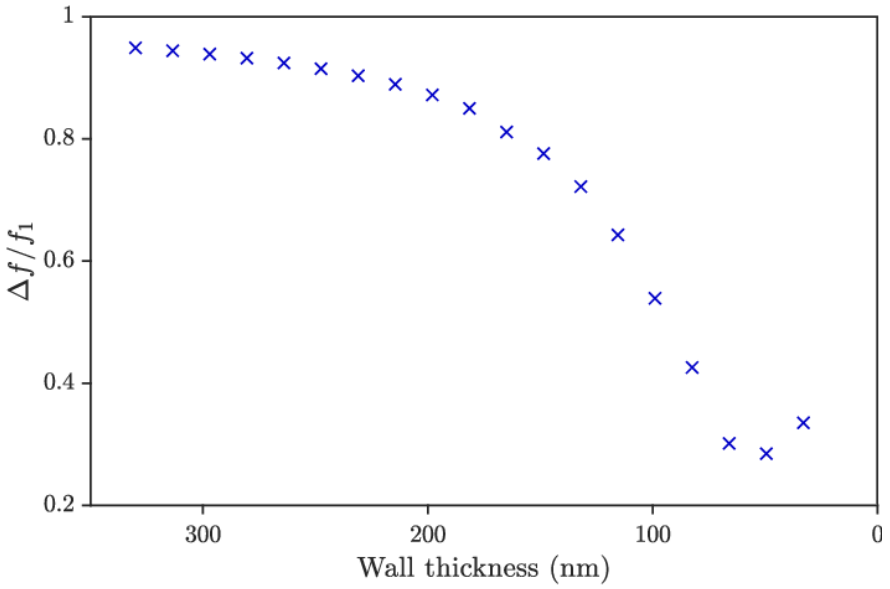


Figure 4-3: Tracking the normlised frequency bandwidth between the $m = 1$ and $m = 2$ resonance with respect to the reduction in wall thickness. $f_1(f_2)$ is the frequency at the $m = 1(m = 2)$ resonance. $\Delta f$ is the difference between $f_1$ and $f_2$. The frequency bandwidth is normalised by $f_1$. The wall thickness started at 330 nm and was reduced to 30 nm.

| Wall thickness (nm) | $m = 1$ (nm) | $m = 2$ (nm) |
|---|---|---|
| 76.5 | 187 | 136 |
| 78.2 | 190 | 137 |
| 79.9 | 193 | 137 |
| 81.6 | 196 | 138 |
| 83.3 | 199 | 139 |
| 85.0 | 203 | 140 |
| 86.7 | 206 | 141 |
| 88.4 | 209 | 142 |
| 90.1 | 211 | 143 |
| 91.8 | 214 | 144 |
| 93.5 | 217 | 145 |

Table 4.1: Tube wall thickness with the corresponding location of the $m = 1$ and $m = 2$ resonance. The target wall thickness of 85 nm is varied slightly to show the shift in the $m = 1$ and $m = 2$ resonance wavelength.

330 nm which is reduced a minimum of 30 nm. Between the wall thickness of 330 nm to about 180 nm, the reduction in the bandwidth is small as the refractive index is not changing by much between the $m = 1$ and $m = 2$ resonance. However, between 180 nm to 80 nm the frequency bandwidth is reduced linearly which is expected as the refractive index is increasing but at a slow constant rate. For wall thicknesses below 80 nm the resonances are located in regions where the refractive index is increasing rapidly. The increase in the refractive index is causing the resonances to come closer together, this causes a reduction in the frequency bandwidth. From about 60 nm to 40 nm, the $m = 2$ frequency is only 30% different than that of the frequency at $m = 1$.

Table 4.1 shows the position of the $m = 1$ and $m = 2$ resonance for a given wall thickness. The wall thickness is varied about 85 nm (a wall thickness designed for the VUV) to demonstrate the realistic effect on the bandwidth when building a HCNCF to guide VUV wavelengths. It can be seen that the maximum bandwidth range is 72 nm and the minimum bandwidth range is 51 nm. Realistically the tubes in the structure contain a mixture of wall thickness. Different thicknesses mean that the tubes have resonances at different wavelengths which causes the overall resonance to widen. In this

example the range of the $m = 1$ wavelengths is 30 nm and for the $m = 2$ wavelengths it is 9 nm. These results highlight the importance of manufacturing optical fibres whose tubes have a very small deviation from the target wall thickness in order to maximise the size of the transmission bandwidth. Note that although the compression is exaggerated in the VUV due to the increase in the refractive index, this effect is still present in the visible and near-IR. However, the effect of the contraction is not as strong due to the slowly varying refractive index within that wavelength range.

Investigating the Fabry-Perot model with regards to the behaviour of the bands towards the VUV has important implications in the engineering of the optical fibre. For HCNCFs the guidance mechanism assumes glancing angle reflections as the light travels through the optical fibre. It is thus safe to assume that the shallower the angle the greater the Fresnel reflection (Hecht 2016). Therefore, it's expected that the rise in loss due to the resonance is sharp as represented in figure 2-3 for a reflectivity coefficient greater than 0.75. This sharp rise to resonance would aid in increasing the width of the low-loss region in the VUV where experimental optical fibres suffer from widened resonances due to a distribution in the wall thickness across different tubes during manufacturing. This sharp rise is reflected in the literature (Pryamikov et al. 2011, Kolyadin et al. 2013, Wang and Ding 2017).

The discussion so far has been theoretical. Observing and quantifying experimental bandshifts will lead to a practical understanding of what is needed to produce a VUV guiding HCNCF using the tapering technique.

### 4.1.1 Experimental band shifting

The Fabry-Perot model was used to describe the physics of the transmission band as the fibre's outer diameter is reduced via tapering. It is also important to experimentally demonstrate the shifts in the resonances for a tapered fibre. The method shown in

figure 4-4 was used in order to measure the transmission spectrum of the test sample fibre. A Xenon lamp was used as the white light source due as its transmission spectra ranged from approximately 180 nm to the mid-infrared (Zhang and Boyd 2000). The light was coupled into an input fibre (SMF-28 for example) via two parabolic mirrors. The first one the light was incident on was used to collimate the light and the next was used to focus electromagnetic waves into the core of the optical fibre. The input fibre had a couple of important properties. Firstly, not to absorb any wavelengths which the spectrometer could detect and also a core diameter equal to or less than the sample core diameter. This was to ensure that only core modes are excited in the sample fibre and avoid generating cladding modes. The types of input fibres could be SMF-28, photonic crystal fibre or a high-OH doped step-index fibre as the UV absorption is relatively low (Février et al. 2009, Huebner et al. 2000). The test samples were about 10 cm in length to maximise the output signal by keeping it in a straight line. The output fibre should have a core large enough to collect all of the output light from the sample. Again, like the input fibre, this optical fibre should not contain any material that would absorb the wavelengths which could be detected by the spectrometer. All of the fibres in this set-up were butt-coupled (cross-section to cross-section) to each

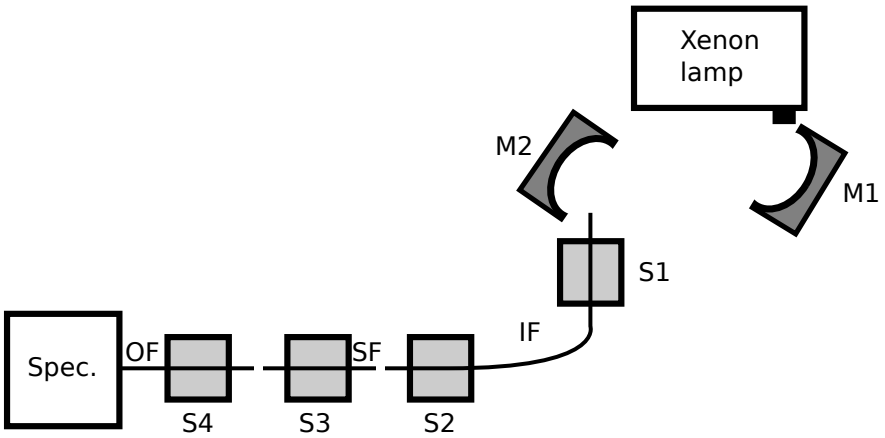


Figure 4-4: Experimental set-up used to measure the transmission of the fibre in dBm. Mirrors M1 and M2 are parabolic, IF is the input fibre, SF is the sample fibre and OF is the output fibre which is coupled to a spectrometer. S1, S2, S3 and S4 are the stages which hold the optical fibres. The spectrometer (Spec.), then records the output signal of the optical fibre.

other. The butt-coupling was performed by adjusting the position of one of the fibres such that the output intensity of the other fibre was maximised in order for the fibre core to align both vertically and horizontally.

The HCNCF fibre that was used to test the scaling consisted of 7 tubes and was produced using the stack and draw method (section 2.2). Figure 4-5 shows the attenuation curve measured from the 7 tube HCNCF (inset). The final attenuation curve represents the mean of 10 separate spectra where the cut-back (section 2.1.3) measurement technique from a length of 18 m to 5 m was used. It can be seen that in between 1000 nm and 1250 nm the loss of the optical fibre is on average 0.03 $\pm$ 0.02 dB/m. The inset shows an optical micrograph image of the optical fibre. The physical parameters of the fibre are as follows, core diameter is 32 $\pm$ 1 µm, resonator diameter 17 $\pm$ 1 µm and

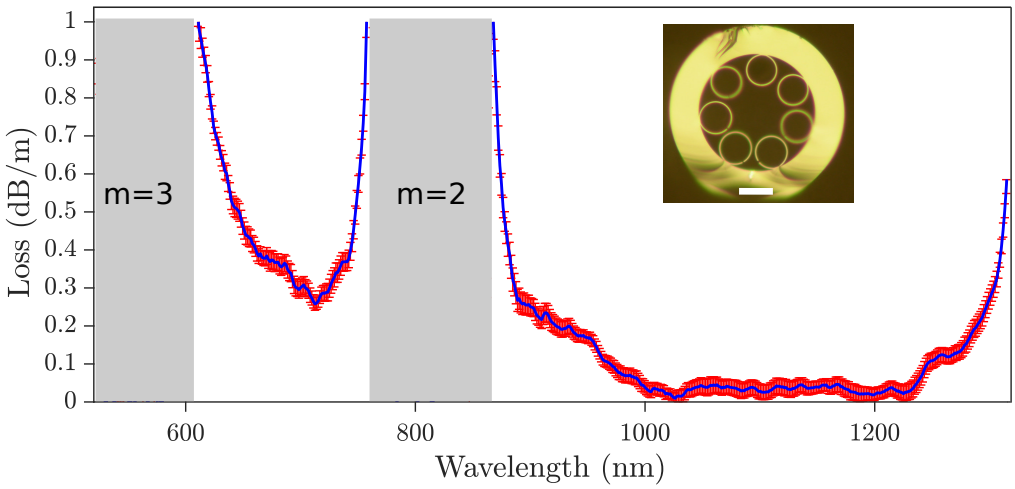


Figure 4-5: Attenuation curve of the fibre (inset) measured via a cut-back measurement from 18 m to 5 m. Between 1000 nm and 1250 nm the average loss is 0.03 $\pm$ 0.02 dB/m. The uncertainty for the loss measurement comes from modifying the set-up by alternating between re-cleaving the output end of the fibre and slightly perturbing the layed out fibre. The inset shows an optical micrograph image of the fibre with a core diameter of 32 $\pm$ 1 µm, resonator diameter 17 $\pm$ 1 µm and a wall thickness of 720 $\pm$ 13 nm. The uncertainties represent the range of the core diameter and the resonator diameter which arise from taking multiple measurements of their sizes. The uncertainty for the wall thickness comes from measuring the width of the $m = 3$ resonance ($\lambda = 512 \pm 7$ nm) meaning that the exact location of the resonance wavelength cannot be pinpointed. The scale bar on the image of the fibre represents 20 µm.

a wall thickness of approximately 720 $\pm$ 13 nm. The uncertainty in the discrete measurements arise from measuring the physical parameters multiple times. However, the error in the wall thickness comes from the width of the $m = 3$ resonance, meaning that there is no constant wall thickness across the 7 tubes. Furthermore, the uncertainty in wall thickness arises from the width of the $m = 3$ resonance.

The scaling was tested by using the original fibre in figure 4-5 and incrementing the draw-down ratio from 1 to 2 in steps of 0.2. The length of each sample was approximately 10 cm to maximise the amount of output light from the sample. The results of the band shifts is shown in figure 4-6. Resonance locations were calculated using equation (2.7). A refractive index of 1.45(1.46) was used for resonances at wavelengths greater(less than) 500 nm. It can be seen that the result shows a clear shift of the first resonance. The relative shift should be linear for the wavelengths within the regions being probed as the refractive index varies slowly. This is observed.

Two assumptions were made when the results of figure 4-6 were produced. The first is that the refractive index has a value of 1.45 which is validated from the results of figure 1-7(a). The second assumption is that the wall thickness has been reduced by the quoted draw-down ratio. This postulate may not be entirely justified as the tubes may have collapsed slightly during the tapering process. Even a partial deviation from the target wall thickness can drastically change the transmission properties of the optical fibre (section 4.1).

The test of the structural changes were made using the method discussed in section 2.3.1 where aspect ratios, such as tube diameter to core diameter, of the fibres were measured to see if they remain constant. In this case the aspect ratio was the diameter of the resonator to the diameter of the fibre's core. Figure 4-7(b) shows these results.

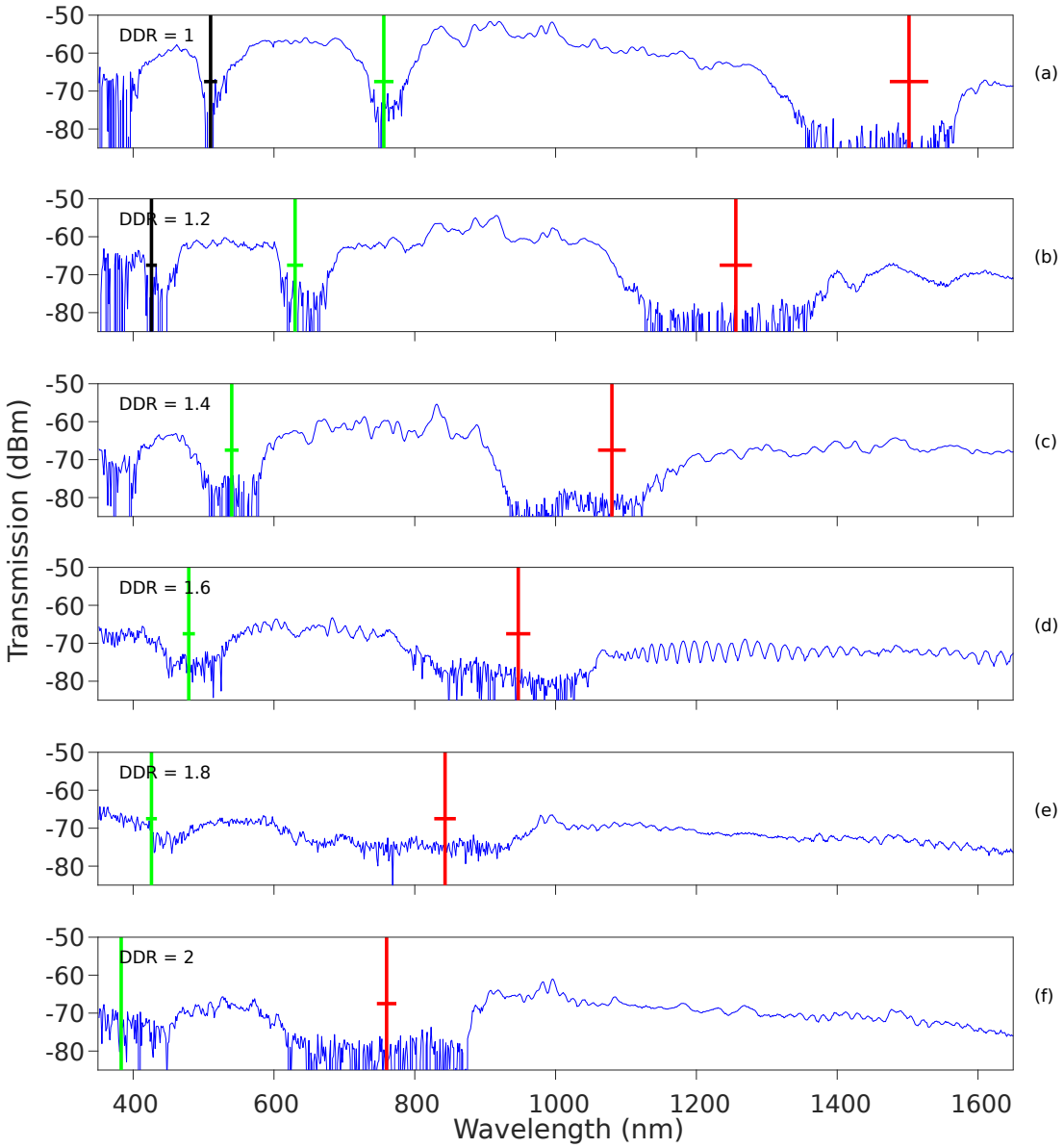


Figure 4-6: Band shifts of the 7 ring HCNCF. The draw-down ratio ranges from 1 to 2 in steps of 0.2. The solid red vertical line represents the predicted location of the $m = 1$ resonance given by equation 2.7, with a refractive index value of 1.45. The solid green vertical line is the predicted location of the $m = 2$ resonance and the black vertical line is the predicted location of the $m = 3$ resonance. For wavelengths which are $< 500$ nm the refractive index value used was 1.46. The horizontal lines are the uncertainties in the predicted locations for the resonance wavelengths. The uncertainty derives from the uncertainty in the predicted wall thickness from the $m = 3$ resonance for DDR $= 1$. The wavelength step in the spectra was 1.5 nm.

The error bars represent the standard deviation in the aspect ratio measured for all 7 resonators in the structure. The last two draw-down results 3.1 and 4.3 will be discussed later. First of all, the error bars suggest that there is a deviation in the size of the resonators which most likely occurred during the inflation process while the fibre was being built. This would explain why the resonances in figure 4-6 are wide. If all the tubes are slightly different sizes then their wall thickness will also vary meaning that the walls will have differing resonant wavelength values, leading to wide regions of high loss. Secondly, all of the aspect ratios lie within their errors, hence, the band shifts are expected to be linearly related. Even though all of the aspect ratios lie with their uncertainties for the DDR values between 1.2 and 2 there is a clear down trend in the mean value, indicating that there is larger average collapse of the tubes with an increase in draw-down ratio. This is not unexpected as the surface tension of the tubes increases with an increase in draw-down ratio, leading to a larger possibility that the tubes would collapse. Figure 4-7(a) shows optical micrograph images of the cross-sections of the optical fibres with draw-down ratios between 1 and 2. Cleaving an optical fibre can occasionally lead to an uneven cross-section making it challenging to obtain

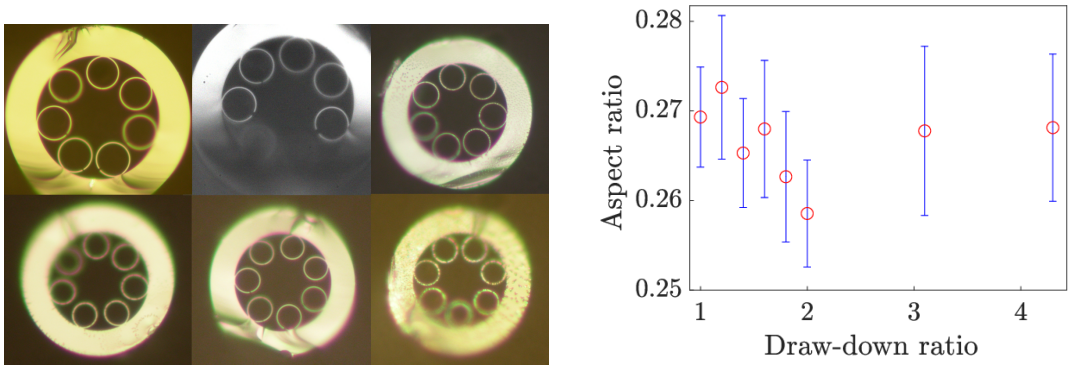


(a) (b)

Figure 4-7: (a) Optical micrograph images of the fibre which have a draw-down ratio of 1 (top left) to 2 (bottom right) in steps of 0.2. (b) The aspect ratio measurements taken as the ratio between the tube diameter and the core diameter. The error bars represent the standard deviation of the aspect ratio which originates from measuring that ratio for each of the resonators in the fibres.

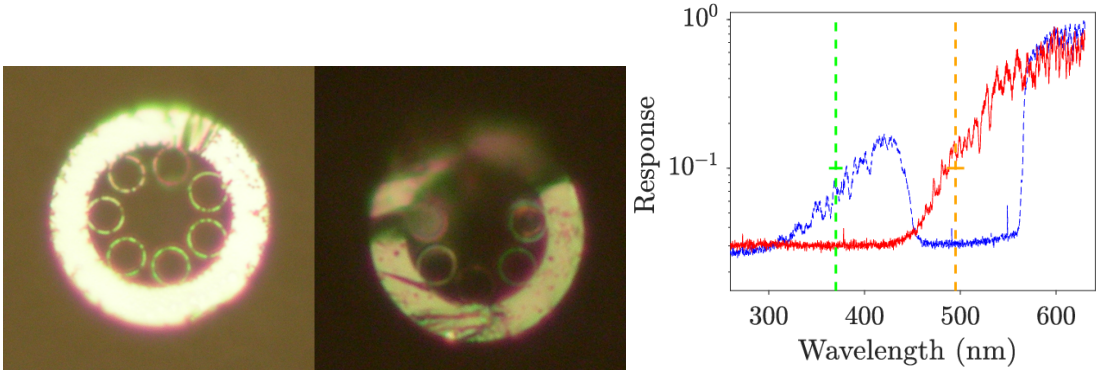


(a) (b)

Figure 4-8: (a) Optical micrograph images of the fibre which have a draw-down ratio of 3.1 (left) and 4.3 (right). (b) The response (or count), represents the signal strength of the spectrum transmitted by the fibres for the draw-down ratios 3.1 (dashed-blue) and 4.3 (solid-red). The dashed vertical orange and vertical dashed green line represents the location of the $m = 1$ resonance, given by equation (2.7), for the draw-down ratios of 3.1 (dashed-blue) and 4.3 (solid-red), respectively. The refractive index was estimated to be at the mid-point of the first resonance for the draw-down ratio of 3.1 ($\lambda = 500$ nm, $n = 1.46$). As the end of the resonance band for the draw-down ratio of 4.3 was not visible it was assumed that the width of the resonance band was the same as that for the draw-down ratio of 3.1. Hence the resonance wavelength was estimated to be 370 nm for a value of refractive index of 1.49. These results were then used to plot the location of the solid green line. The horizontal error bars represent the uncertainty in the measurement of the resonance location. The uncertainty is that of the $m = 3$ (DDR=1) measurement in figure 4-6.

a focused image of the entire cross-section. The tubes in the blurred sections of the images were included in the aspect ratio measurements by refocusing the microscope.

The results for the draw-down ratio of 3.1 and 4.3 are not shown in figure 4-6 as the spectrometer (Ando AQ-6315B) used did not have the capacity to measure below 350 nm. To overcome this problem a miniature CCD based spectrometer (Ocean Optics USB4000 spectrometer) replaced it as it can measure wavelengths down to 200 nm, however with a reduced dynamic range (figure 4-8). It can be seen that the first resonance is still observed for a draw-down ratio of 3.1 with the solid red line representing the prediction given by equation (2.7) (the refractive index was measured from the mid-point of the resonant band using the results from (Kitamura et al. 2007)). However, this is not seen for a draw-down ratio of 4.3. The most likely reason is the experimental

set-up. The parabolic mirrors are poor at reflecting the UV light and hence the signal strength (or response) is low. Therefore, modifications to the set-up need to be made in order to accommodate these shorter wavelengths. The aspect ratios for the draw-down ratios 3.1 and 4.3 are within error of the other draw-down ratios (figure 4-7(b)). The mean value for both DDR = 3.1 and DDR = 4.3 is similar to that of DDR = 1, indicating that the expected wall thickness was reduced by the target draw-down ratio.

Although most of the results were measured where the refractive index of silica glass is constant it was shown that the scaling (equation 2.7) was sufficient in predicting where the resonance, and by extension the antiresonance, wavelengths should occur. The tapered samples were sent to a collaborating group which I visited twice to build (alongside the post-doc Dmitry Vorobiev) the experimental set-up which measured the transmission of the samples in the VUV (Brian Fleming, LASP, University of Colorado at Boulder).

## 4.2 Guiding 185 nm

In section 4.1 the theoretical and experimental results of band shifting were discussed. In summary, as the tube wall thickness is reduced, the resonances shift to shorter wavelengths, with the distance between the $m = 1$ and $m = 2$ resonance reducing, due to the increase in the refractive index.

My attempt in shifting the bands to the VUV was to guide 185 nm between the $m = 1$ and $m = 2$ resonance as it would allow for the development of an experimental set-up to measure in the VUV as well as understanding the nuances in manufacturing such a fibre.

The untapered optical fibre to make this measurement was a 10 tube HCNCF. It was drawn using the standard stack and draw method with the tension on the cross-

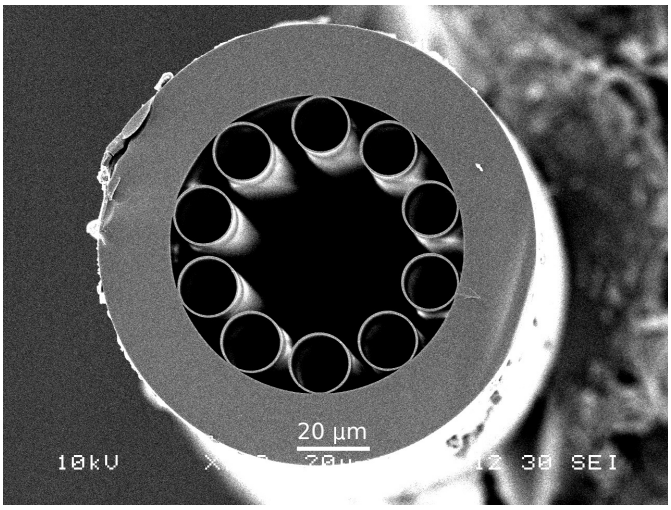


Figure 4-9: SEM image of the untapered optical fibre. The physical parameters of the fibre are the following, outer diameter 120 ± 0.57 µm, core diameter 49 ± 0.49 µm, resonator outer diameter 16 ± 0.39 µm and a wall thickness of 500 ± 28 nm. Scale bar represents a length of 20 µm.

sectional area of the glass being 13.4 kg/mm$^2$ at the preform to fibre stage. Figure 4-9 shows an SEM image of the optical fibre. The physical dimensions of the optical fibre was a tube wall thickness was measured to be 500 ± 28 nm (measured from the $m = 3$ resonance, figure 4-10(a)), outer diameter of 120 ± 0.57 µm,, a core diameter of 49 ± 0.49 µm and a resonator outer diameter of 16 ± 0.39 µm.

Figure 4-10(a) shows the output spectrum of a 15 cm piece. It can be seen that between 400 nm to 1600 nm two resonance dips are observed. The one at longer wavelengths corresponds to the $m = 1$ resonance which occurs at approximately 1000 nm. The $m = 2$ resonance is located at a wavelength of approximately 530 nm. The width of the resonances comes from the small variations in tube tall thickness of the optical fibre. Figure 4-10(b) shows the attenuation curve for the fibre measured using the cut-back method. The long piece of fibre is 40 m which was cut down to a length of 4 m. Even though the short length is typically 10 m, in this case the 4 m length would not cause a significant overestimate of the loss as the fibre is not very multimoded. The lowest loss point in between the $m = 1$ and $m = 2$ resonance occurs at 780 nm with a loss of

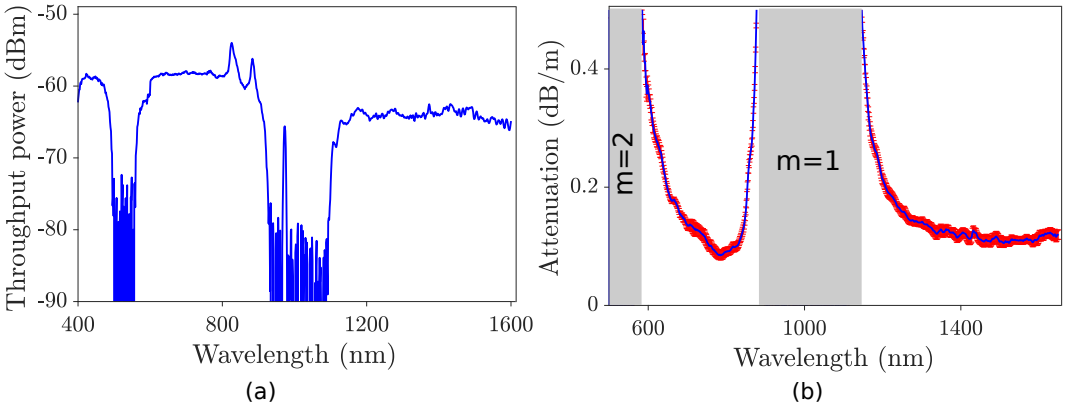


Figure 4-10: (a) Short 15 cm piece transmission of the optical fibre. (b) Cut-back measurement from a long length of 40 m to 4 m. The lowest loss points between $m = 1$ and $m = 2$ resonance is at a wavelength of 780 nm with a loss of 0.08 dB/m. For wavelengths longer than the $m = 1$ the loss is on average 0.1 dB/m. The width of the resonances is attributed to small variations in the wall thickness between the tubes of the optical fibre. The resolution of the measurements was set to 1.4 nm.

0.08 dB/m. For wavelengths longer than the $m = 1$ resonance the loss is on average 0.1 dB/m. The experimental set-up for both measurement consisted of a Xenon lamp as the input white light source which was coupled into an SMF-28 fibre. The output light of the optical fibre was captured by a 400 µm patch cable which was then coupled into a OSA spectrometer.

The low loss from the attenuation spectrum shows the quality is good enough for tapering. The need to have a good quality starting fibre is vital as the quality of the fibre will only degrade due to tapering as there is no active pressurisation occurring during the tapering process, thus the tubes are susceptible to collapsing under their own surface tension whilst being tapered, reducing the quality of the sample.

### 4.2.1 Tapered optical fibre

The tubes of the original untapered optical fibre have a wall thickness of approximately 500 nm whilst the required wall thickness to guide 185 nm between the $m = 1$ and $m = 2$ resonance is 110 nm, which corresponds to a draw-down ratio of 4.4. Reducing

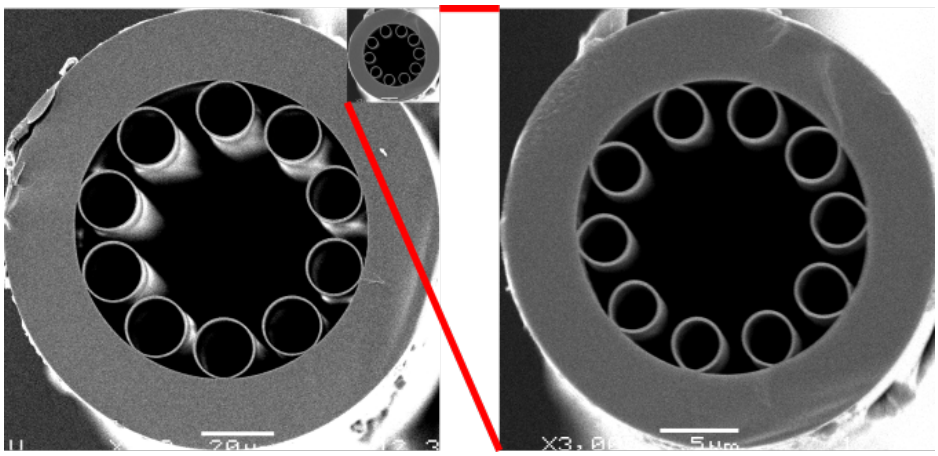

Figure 4-11: (Left) SEM image of the untapered fibre. (Inset) Scaled SEM image of the tapered optical fibre. (Right) SEM image of the tapered fibre with a draw-down ratio of 4.7. The physical parameters of the tapered fibre are as follows, outer diameter 25 $\pm$ 0.15 µm, core diameter 11 $\pm$ 0.07 µm, wall thickness approximately 110 nm and a resonator outer diameter of 3.5 $\pm$ 0.10 µm. Left scale bar represents 20 µm and the right scale bar represents 5 µm.

the outer diameter by 77% whilst keeping the internal structure of the optical fibre from collapsing requires a careful implementation of the tapering process. In this case the cladding of the optical fibre is not that thick therefore the transfer of heat from one side of the cladding to the other will be fast. In this case a single-phase (constant burner and stage retracting speed) was used with the flame sweeping underneath the fibre at a speed of 695 mm/min and the stages retracted at a speed of 731 mm/min.

The final tapered optical fibre can be seen in figure 4-11(right). The physical parameters of the tapered fibre are as follows, outer diameter 25 $\pm$ 0.15 µm, core diameter 11 $\pm$ 0.07 µm, wall thickness approximately 110 nm and a resonator outer diameter of 3.5 $\pm$ 0.10 µm. The draw-down ratio was increased from the target of 4.4 to 4.7. Since it is very likely that the tube will collapse to some degree during tapering then compensating for the difference in the final tube wall thickness and target wall thickness is necessary. This is done by increasing the draw-down ratio such that the 'slightly' collapsed tubes will then have the target wall thickness, as opposed to a thicker wall which would occur without the compensation in draw-down ratio. The drawbacks

with this method are that the 'extra' draw-down ratio is an estimate and the physical properties of the optical fibre, such as the core diameter, will be smaller than the initial design target.

The set-up used to make the 185 nm transmission measurement can be seen in figure 4-12. The apparatus involves a mercury lamp which emits strong lines at 185 nm and 255 nm which then illuminated the cross-sections of an approximately 10 cm long fibre sample. The output from the optical fibre is then incident onto the blazed grating in the monochromotor which reflects the light onto a photomultiplier tube. A water droplet was added to ensure any stray light that is travelling around the fibre is absorbed so it does not enter the monochromotor. The short distances within the set-up meant that it did not need to be evacuated. The output of the mercury lamp for both lines was intense enough that the atmospheric absorption over the path length of the experiment did not have a significant effect on the results (Wilkinson and Johnston 1950). Aligning the output of the optical fibre to the monochromator required the fibre to lay straight on its stage. HCNCFs have a low numerical aperture, approximately 0.04, meaning that all of the light can be readily collected by the blazed grating.

Using equation (2.7) predictsfor a wall thickness of 110 nm, that the $m = 1$ and $m = 2$ resonance to be located at 255 nm and 155 nm, respectively. Figure 4-13 shows the results of the transmission of the sample tapered fibre. The line transmission (blue dots) of the optical fibre as well as without the optical fibre (grey crosses) at 185 nm and 255 nm is shown. The solid black line represents the transmission spectrum of the original 10 tube optical fibre. The solid(dashed) vertical lines represent the predicted location of the $m = 1$ (red) and $m = 2$ (green) resonances given by equation (2.7).

The results show a strong signal at 185 nm with the optical fibre in place whilst at 255 nm the signal is at the noise level even though the emission of the mercury lamp at

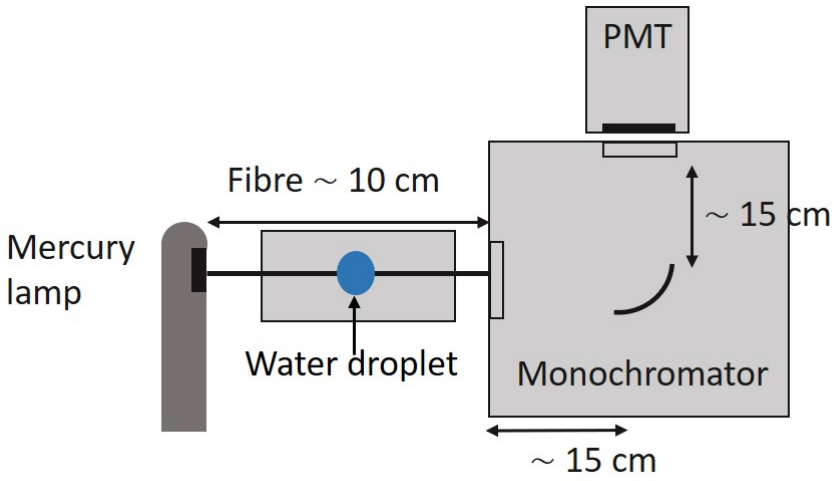


Figure 4-12: Set-up used to measure 185 nm guidance. Initially the output of a mercury lamp which has strong emission lines at 185 nm and 255 nm illuminated the cross-section of the optical fibre which is approximately 10 cm in length. The output of the fibre is then incident onto a concave blazed grating which reflects the light onto a photomultiplier tube (PMT). A water droplet was added to absorb the stray light that travels around the optical fibre preventing it from entering the monochromator. I visited LASP where I helped build this set-up with Dmitry Vorobiev. (Winter, Vorobiev, Fleming, Witt, Gilliam, Rusimova, Yerolatsitis, Birks and Wadsworth 2019)

255 nm is approximately 50 times stronger than at 185 nm. The $m = 1$ resonance is located at 255 nm and the 185 nm signal lies in between the $m = 1$ and $m = 2$ resonances which was the target when designing this fibre. Furthermore, this result demonstrates one of the primary difficulties in developing an optical fibre for the VUV which is the contraction of the transmission bandwidth due to the increase in the refractive index. The percentage change between the $m = 1$ and $m = 2$ resonances of the untapered and tapered fibres was 69% highlighting the need for a good starting structure pre-tapering to avoid wide resonances.

Although the result in figure 4-13 confirms that HCNCF could be fabricated for VUV guidance, in order to push it further two factors need to be addressed. Firstly, the source would need to emit a continuum of wavelengths within the VUV as it would allow for the study of the band behaviour at these ultra-short wavelengths. The second

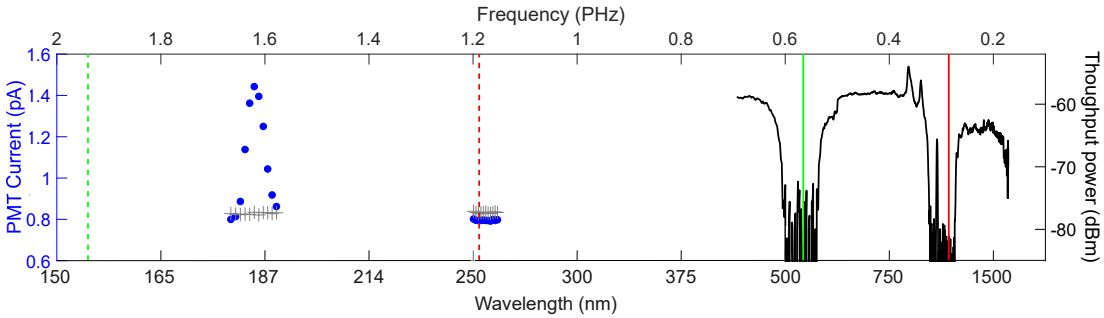


Figure 4-13: Throughput spectrum of a 150 mm long piece of the 10 tube untapered fibre (solid black line). The transmission of the tapered fibre (blue dots) and with the fibre removed (grey crosses) which are at the location of mercury's two brightest lines in the ultraviolet (185 nm and 255 nm). The solid(dashed) vertical lines show the predicted locations of the $m = 1$ (red) and $m = 2$ (green) resonances.

point is that the signal to noise in figure 4-13 is low, a feature which is attributed to the small core of the tapered fibre. The small core limits the number of modes which can propagate through the fibre and hence reduces the strength of the signal which the fibre will output. This is the primary motivation to manufacturing a multimode HCNCF as a better signal to noise will reveal a clearer transmission spectrum and also reduce the confinement loss allow for shorter VUV wavelengths to be guided.

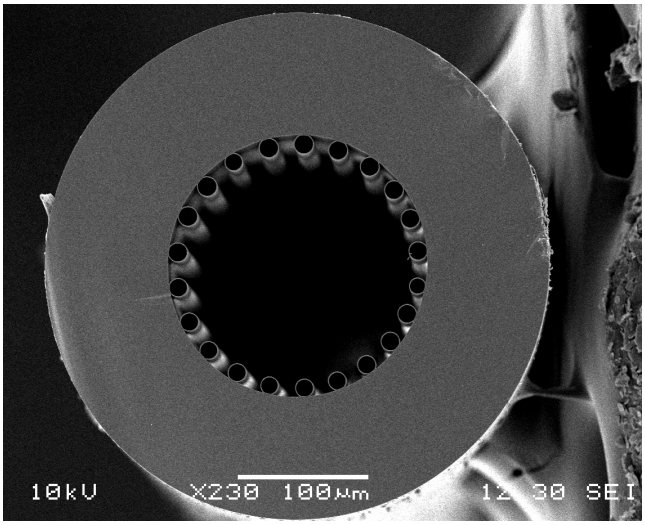


Figure 4-14: SEM an untapered multimode optical fibre. The physical parameters of the optical fibre are as follows, outer diameter is 387 $\pm$ 1 µm, resonator outer diameter 14.8 $\pm$ 0.8 µm, core diameter 171 $\pm$ 2 µm and wall thickness 672 $\pm$ 27 nm.

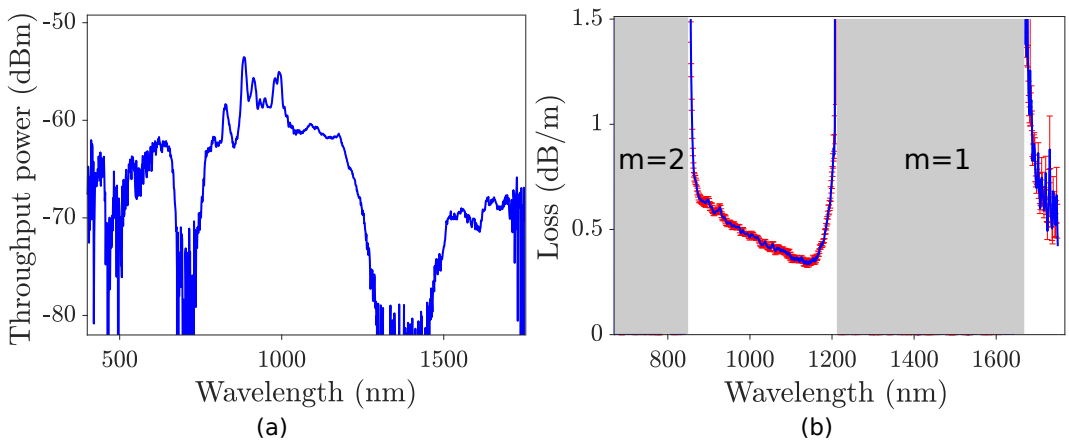


Figure 4-15: (a) Short 15 cm piece transmission of the optical fibre. (b) Cut-back measurement from 22.5 m to 10 m. The loss between the $m = 1$ and $m = 2$ resonance is approximately 0.5 dB/m. The increase in the width of the resonances is attributed to the non-uniformity of the tube wall thicknesses. The wavelength resolution is 1.4 nm.

### 4.2.2 Multimode optical fibre for VUV guidance

The results in section 4.2 showed that manufacturing a fibre which guides VUV is possible. The problems which need to be overcome primarily revolve around improving the signal to noise ratio through the optical fibre by developing a multimode HCNCF.

Whilst the main goal is to produce an optical fibre to guide VUV wavelengths, there are applications which would benefit from fibres which guide in the UV and deep-UV. Namely in eye surgery. The specific wavelengths are the 4th and 5th harmonic of 1064 nm, i.e. 266 nm and 213 nm respectively (Farid et al. 2013). The current technology relies on using tapered capillaries which rely solely on glancing angle guidance. The interaction of the radiation at these wavelengths with the glass makes this technique high loss. Developing a multimode HCNCF for this application is optimal as low loss guidance is required over a distance of approximately 20 cm.

Figure 4-14 is similar to that represented in figure 3-4 except the tubes are not as inflated, thus increasing the space between them. The outer diameter was measured to

be 387 ± 1 μm with the tube outer diameter being 14.8 ± 0.8 μm, the core diameter is 171 ± 2 μm and the wall thickness 672 ± 27 nm. In terms of performance figure 4-15 shows both the short piece (approximately 15 cm) transmission and also the attenuation curve measured via the cut-back technique starting from a length of 22.5 m to 10 m. The short piece transmission shows that the $m = 1$ resonance is located at approximately 1380 nm with the $m = 2$ predictably at about 700 nm. The attenuation is about 0.5 dB/m between the $m = 1$ and $m = 2$ resonances. Although the loss is quite high this fibre is suitable for the application as the material loss of silica glass at both 266 nm and 213 nm is low enough to still achieve the desired goal. Figure 4-16 shows an SEM image of the tapered fibre designed to guide 266 nm. The 22 tube tapered fibre was created using a draw-down ration of 4.06. The tapering comprised of three phases. The first phase reduced the outer diameter from 387 μm to 300 μm. The stage retraction rate was 40 mm/min and the burner sweep speed was 78 mm/min. The ratio between butane and oxygen was kept constant throughout tapering at 0.79. The second phase reduced the outer diameter from 300 μm to 200 μm. The stage retraction rate was 71 mm/min and the burner sweep speed was 91 mm/min. The

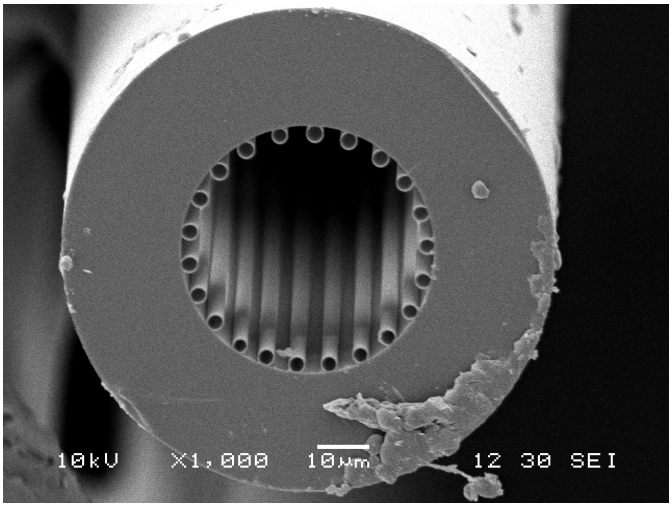


Figure 4-16: SEM of the tapered optical fibre which was designed to guide 266 nm between $m = 1$ and $m = 2$. The physical parameters of the optical fibre are as follows, outer diameter is 96 ± 0.61 μm, resonator outer diameter 3.6 ± 0.20 μm, core diameter 42 ± 0.41 μm and wall thickness 200 ± 6.7 nm.

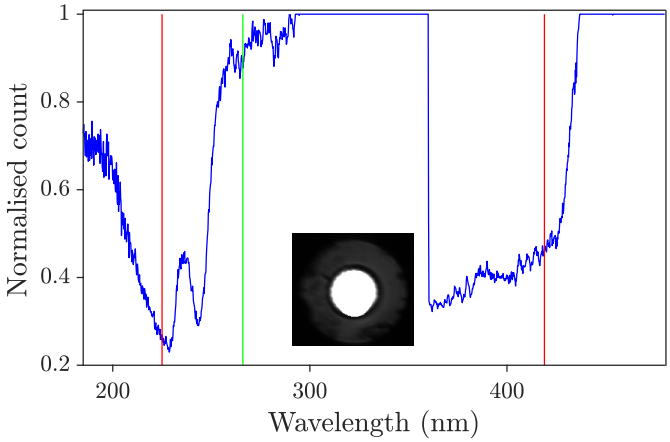


Figure 4-17: Transmission of the 20 cm long tapered piece of fibre designed to guide 266 nm between $m = 1$ and $m = 2$. The vertical green line represents the target wavelength of 266 nm. The red vertical lines shows the predicted locations of the $m = 1$ and $m = 2$ resonances for a wall thickness of 200 nm. The inset shows the light being coupled into the core of the optical fibre. The normalised count is calculated as the transmission point divided by the maximum transmission signal. The bump at approximately 245 nm is due to some of the tube wall thicknesses allowing guidance at that wavelength.

third and final phase reduced the outer diameter from 200 µm to 96 µm. The stage retraction rate was 350 mm/min and the burner sweep speed was 559 mm/min. It resulted in an optical fibre with the following physical parameters. A length of 20 cm, an outer diameter of 96 $\pm$ 0.61µm, a tube outer diameter of 3.6 $\pm$ 0.20 µm, core diameter of $42 \pm 0.41$ µm and a final wall thickness of 200 $\pm$ 6.7 nm. For this wall thickness the predicted locations of the $m = 1$ and $m = 2$ resonance are 358 nm and 198 nm respectively. The experimental set-up used to measure the UV guidance of this optical fibre is represented in figure 4-12 is specially designed to maximise guidance in the UV. The white light source was a Xenon lamp whose output extends into the deep-UV down to approximately 180 nm. The output light was then collimated and focused into a high-OH doped optical fibre, known as the input fibre. The OH doped fibre reduces the loss in the UV with the attenuation being approximately 1 dB/m at 200 nm. The input fibre was then butt-coupled to the sample fibre with the output also being butt-coupled to another high-OH doped fibre which was then the input to a UV to VIS spectrometer (USB4000 Ocean Optics).

When coupling light into the sample fibre, the priority is to excite core modes whilst minimising the number of excited cladding modes. A CCD camera (DMK 41BU02) was used to get a near field image of the output fibre. The inset in figure 4-17 shows that the majority of the light is confined in the core. Furthermore, this behaviour can be seen in in figure 4-17 where the characteristic resonance dips can be seen at approximately 230 nm and 380 nm indicating that little to no cladding light is being measured. The material loss of silica glass at these wavelengths also helps in this respect as the cladding light will be heavily attenuated before reaching the output end of the fibre.

The previous fibre was designed to guide the 4th harmonic of 1064 nm. However, the 5th harmonic of 213 nm guidance is also required by the collaborating group. The same optical fibre as that in figure 4-14 was tapered. The draw-down ratio in this case was 6.00 with the tapering process being the same as that for the 266 nm fibre with the exception being the speeds of the final third phase. The third phase reduced the outer diameter of the fibre from 100 μm to 65 μm. The burner sweep speed was 1300 mm/min

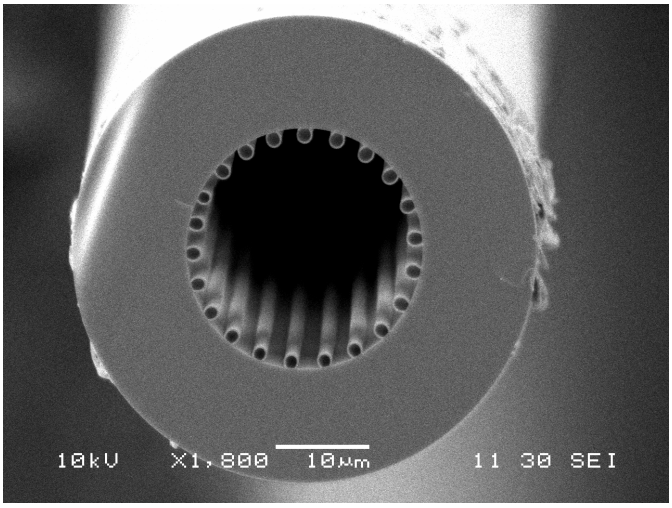


Figure 4-18: SEM of the tapered optical fibre which was designed to guide 213 nm between $m = 1$ and $m = 2$. The physical parameters of the optical fibre are as follows, outer diameter is 65 $\pm$ 0.10 μm, resonator outer diameter 2.5 $\pm$ 0.13 μm, core diameter 29 $\pm$ 0.33 μm and wall thickness 112 $\pm$ 4.5 nm.

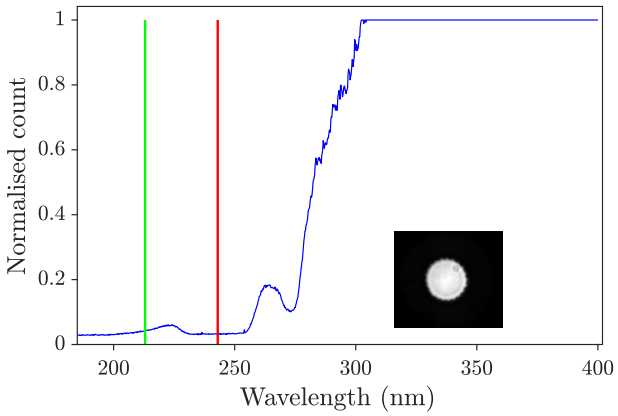


Figure 4-19: Transmission of the 20 cm long tapered piece of fibre designed to guide 213 nm between $m = 1$ and $m = 2$. The vertical green line represents the target wavelength of 213 nm. The vertical red line represents the location of the $m = 1$ resonance for a wall thickness of 112 nm. Inset shows the light being coupled into the core of the optical fibre. The normalised count is calculated as the transmission point divided by the maximum transmission signal.

and the stages retracted from each other at a speed of 1607 mm/min. An SEM image of the tapered fibre can be seen in figure 4-18, with the physical parameters being the following, outer diameter 65 $\pm$ 0.10 µm, resonator outer diameter 2.5 $\pm$ 0.13 µm, core diameter 29 $\pm$ 0.33 µm and the tube wall thickness of approximately 112 $\pm$ 4.5 nm. Figure 4-19 shows the transmission curve for a 20 cm long taper, with the inset being the coupling of the Xenon lamp into the core of the optical fibre. The experimental set-up used to measure the transmission properties of the fibre is the same as that for the 4th harmonic. The characteristic resonance dip can be seen with a rise in signal at about 226 nm. The normalised count is low at these short wavelengths is due to the drop in sensitivity of the spectrometer as well as the weak emission of the Xenon lamp at these wavelengths. Furthermore the signal is made weaker due to the poor reflectivity of the collimating and focusing mirrors which have poor reflectivity in the UV (Hennessy et al. 2016). However, the rise in signal at 226 nm indicates that this fibre should also guide 213 nm.

The previous results revolved around developing optical fibres for both the UV and the deep-UV for applications in eye surgery. However, as previously stated, transmit-

ting shorter wavelengths is a matter of scaling the fibre to the appropriate size. The following example is the result of pushing the multimode design to shorter wavelengths using the fibre represented in figure 3-4. The quality of the fibre which can be seen via the low attenuation of the optical fibre (minimum loss of 0.03 dB/m between the $m = 1$ and $m = 2$ resonances) makes it an ideal candidate to guide VUV wavelengths. The target wavelength was 160 nm between the $m = 1$ and $m = 2$ resonances. This particular wavelength was chosen as it pushed further into the VUV than the previous 185 nm target and it would show the effectiveness of a multimode design in increasing the signal to noise at these short wavelengths.

Guiding shorter wavelengths required a change in the experimental set-up. The primary reason is due to a change in light source, a deuterium lamp with a continuous output which extends from about 100 nm to visible wavelengths (Key and Preston 1980). Such a source means that the features of the transmission bands would be revealed. The experimental set-up can be seen in figure 4-20. The deuterium lamp illuminates the input end of the sample fibre whose output is incident onto a concave blazed grating

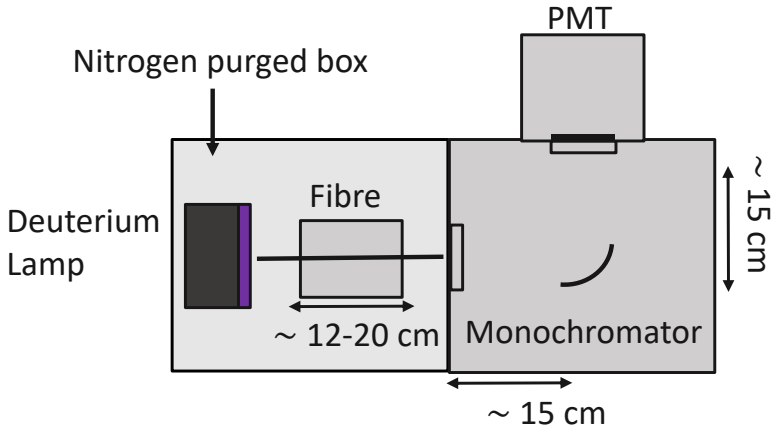


Figure 4-20: Optical set-up used to measure broadband transmission of VUV fibres. The deuterium lamp emits a continuum of wavelengths which extends from approximately 100 nm to beyond the long wavelength edge of the VUV. The light illuminates a cross-section of the optical fibre. The output of the optical fibre is then incident onto a blazed grating which reflects the light onto a photomultiplier tube (PMT). The entire set-up is purged with nitrogen to reduce what would have been the atmospheric loss below 140 nm.

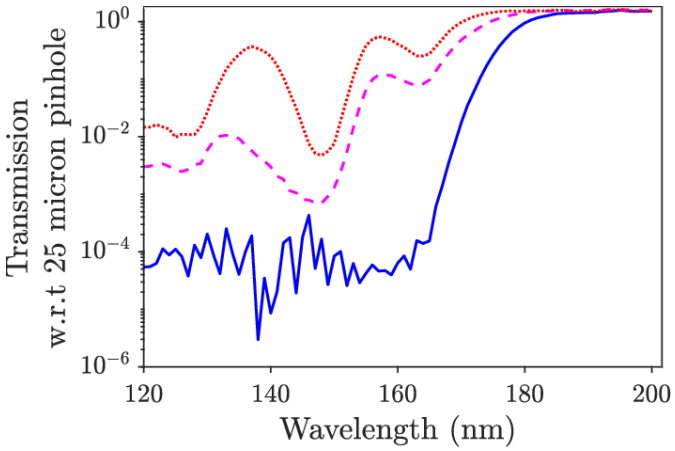


Figure 4-21: Three normalised transmission spectra of the same VUV multimode fibre at time $t_1$ (solid blue), $t_2$ (dashed pink) and $t_3$ (dotted red) where $t_1 < t_2 < t_3$. The normalisation is with respect to the transmission spectra of the deuterium lamp with a 25 µm pinhole at the output.

which reflects the light onto a photomultiplier tubes. Another difference in this set-up to that with the mercury lamp (figure 4-12) is that the entire experiment is purged with nitrogen to reduce the loss from $O_2$ absorption below 180 nm (Gürtler et al. 1977). The effects of the nitrogen purge can be seen in figure 4-21 where a fibre designed to guide 160 nm has its output intensity increase from time $t_1$ to $t_2$ to $t_3$ where it saturates. The length of time in needed to purge the set-up is of course dependent on the pressure of nitrogen which is being pumped into the system, but in our case it is of the order of tens of minutes. Note that I visited LASP (University of Colorado) and built this set-up with Dmitry Vorobiev.

The target wavelength was 160 nm between the $m = 1$ and $m = 2$ resonances. Furthermore the difference in the refractive index at 160 nm and 185 nm is 0.08 which means that the draw-down ratio needs to be exaggerated in order to compensate for the rapid rise in the refractive index. Figure 4-22 shows an SEM image of the cross-section of the tapered fibre. The draw-down ratio in this case was 7.0 with the tapering comprising of a 4-phase process which consisted of 12 sweeps. The constant ratio between butane and oxygen was 0.79. The first phase reduced the outer diameter from

386 μm to 300 μm and had a stage elongation rate of 40 mm/min and burner speed of 78 mm/min. The elongation rate of phase 2 was 140 mm/min whilst the burner speed was set at 186 mm/min with the outer diameter being reduced from 300 μm to 200 μm. Phase 3 had an elongation rate of 550 mm/min and burner speed of 458 mm/min and reduced the outer diameter from 200 μm to 100 μm. The final phase which reduced the outer diameter from 100 μm to 55 μm had an elongation rate of 1400 mm/min and a burner speed of 1307 mm/min. The final physical parameters are as follows, the outer diameter is 55 $\pm$ 0.3 μm, resonator outer diameter 2.3 $\pm$ 0.1 μm, core diameter 24 $\pm$ 0.2 μm and wall thickness 101 $\pm$ 3 nm.

The transmission result in figure 4-23 is that of a tapered fibre which was designed to guide at 160 nm between the $m = 1$ and $m = 2$ resonances. The transmission spectrum is normalised with respect to the transmission of the deuterium lamp with a 25 μm pin hole at its output. The vertical solid-red lines are the predicted locations of the $m = 1$ (230 nm), $m = 2$ (150 nm) and $m = 3$ (130 nm) for a tube wall thickness of 101 nm. The result shows that this optical fibre is guiding in the VUV, confirmed by

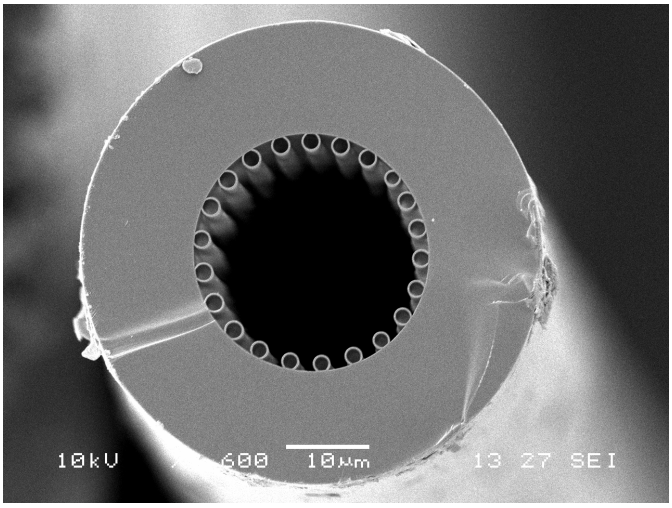


Figure 4-22: SEM of the tapered optical fibre which was designed to guide 160 nm between $m = 1$ and $m = 2$. The physical parameters of the optical fibre are as follows, outer diameter is 55 $\pm$ 0.3 μm, resonator outer diameter 2.3 $\pm$ 0.1 μm, core diameter 24 $\pm$ 0.2 μm and wall thickness 101 $\pm$ 3 nm.

the presence of the resonances, which is a defining characteristic of the antiresonant guidance mechanism. The peak transmission between the $m = 2$ and $m = 3$ resonance occurs at approximately 135 nm. This particular optical fibre does guide 160 nm between the $m = 1$ and $m = 2$ resonance. However, 160 nm is located near the second resonance as oppose to being in the centre of the transmission region. This indicates that during the tapering process the tubes partially collapsed resulting in a thicker wall. Using equation (2.7) the target wall thickness for a wavelength of 160 nm to lie in between the $m = 1$ and $m = 2$ resonance is about 90 nm whilst the vertical solid red lines in figure 4-23 are the predicted resonances for a wall thickness of 101 nm. Therefore, the outer diameter of the tubes was reduced by about 10.8% due to their surface tension.

Figure 4-23 shows that VUV guidance was achieved using HCNCF. However, the application these fibres are designed for would require an array of them to be built. Figure 4-24 shows the transmission spectra (which was normalised in the same way

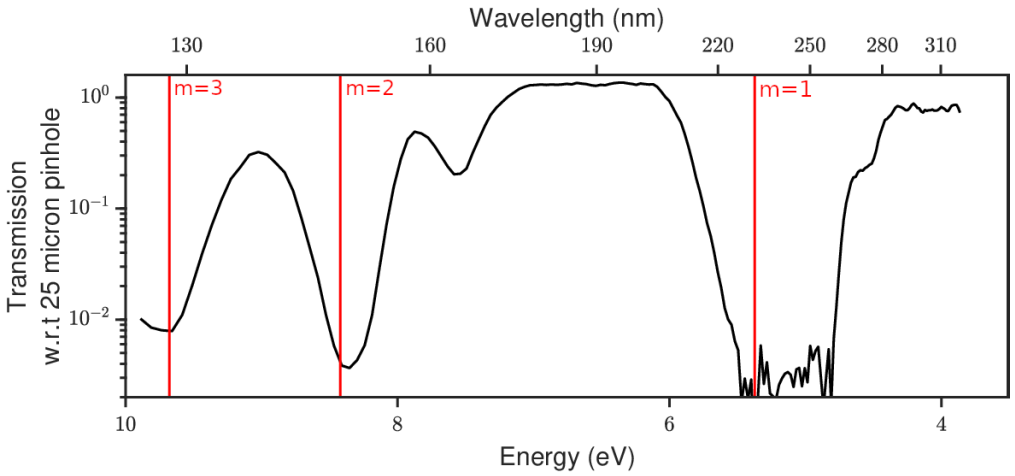


Figure 4-23: Transmission spectra of one of the tapers designed to guide 160 nm between the $m = 1$ and $m = 2$ resonance. The transmission spectra was normalised with respect to the transmission of the deuterium lamp with a 25 µm pinhole at the output. The solid red vertical lines represent the theoretical locations of the first three resonances for a wall thickness of 101 nm. The $m = 1$ resonance is located at 230 nm, the $m = 2$ is at 150 nm and the $m = 3$ resonance is at 130 nm. The abbreviation w.r.t. stands for with respect to.

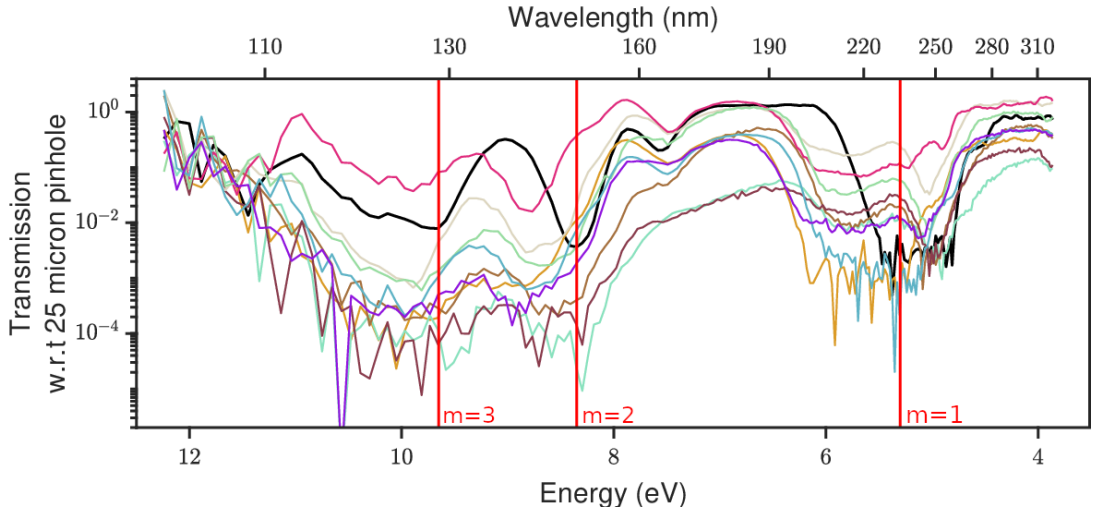


Figure 4-24: Transmission spectra of 10 optical fibre. Each solid transmission line represents a single optical fibre. The transmission spectra were normalised with respect to the transmission of the deuterium lamp with a 25 µm pinhole at the output. The black line as well as the solid-red vertical lines represent the spectrum and resonances from figure 4-23. The abbreviation w.r.t. stands for with respect to.

as in figure 4-23) for 10 VUV tapered optical fibres which were all designed to guide 160 nm between the $m = 1$ and $m = 2$ resonances. The results shows, for all 10 fibres, that the target wavelength is guided between the $m = 1$ and $m = 2$ resonance in all of the samples with varying levels of transmission. Three of the spectra show a clear $m = 1$ resonance. However, the other 7 do not show a noisy signal which would be associated with a resonance but do exhibit a drop in transmission. The wavelength at which this drop occurs is consistent with the samples that have a clear $m = 1$ resonance. This suggests that some of the output of the deuterium lamp is not passing through the core of the optical fibre and is going around the sample and then into the monochromator. This represents some of the limitations which occur when attempting to measure VUV transmission. The $m = 2$ resonance is visible in all but two of the samples. Those are the two fibres (light blue and brown lines) which have the lowest level of transmission between the $m = 1$ and $m = 2$ resonances (solid-red vertical lines at 230 nm and 150 nm respectively). The lack of the $m = 2$, and hence also $m = 3$ resonance, is due to a very low signal-to-noise ratio between $m = 2$ and $m = 3$ reso-

nances. However, the $m = 3$ resonance is visible in the other 8 samples and is roughly at the sample location for all of 8 of them. At approximately 110 nm two samples show a clear signal (black and dark pink), indicating transmission at 110 nm. The refractive index of silica glass at 110 nm is about 1.6. Therefore, assuming glancing angle incidence a ray would enter the glass at an angle of 0.68 radians. For a tube wall thickness of 101 nm the ray of light would travel 260 nm before returning to the core. Using an extinction coefficient of 0.8, the loss over a 260 nm distance is approximately 100 dB. Therefore, the signal at 110 nm is from glancing angle incidence as opposed to antiresonant guidance. At about 130 nm we observe a resonance. The refractive index at 130 nm is approximately 2.2 and the extinction coefficient is $2.0 \cdot 10^{-2}$. The light at this wavelength enters the glass at an angle of 0.47 radians and travels 224 nm through the glass. The loss incurred over a distance of 224 nm is 1.9 dB which is why the features of antiresonant guidance is observed.

To summarise, VUV guidance in a HCNCF has been demonstrated with approximately 135 nm being the shortest wavelength guided through the antiresonant effect. The shortest transmitted wavelength was measured to be about 110 nm but it occurred through glancing angle guidance. The 10 samples showed that the target wavelength of 160 nm can consistently be placed in between the $m = 1$ and $m = 2$ resonance. However, the wavelength is not centered in the transmission band. Therefore improvements to the tapering process will help to prevent the partial collapse of the tubes. Furthermore, modifying the set-up such that the coupling of the light between the deuterium lamp and tapered optical fibre is the same across samples would improve the consistency of the measured transmission levels. The main principles of this research have been demonstrated. The next steps would be to focus on developing these optical fibres to meet the requirements of the final application.

# Chapter 5

# Hollow-core negative curvature fibres for the infra-red

The discussion so far has revolved around the development of HCNCF for guidance in the VUV. Wavelengths which are strongly attenuated by the glass in traditional solid-core optical fibres were shown to be guided by hollow-core structures via the antiresonance effect by removing the material, and hence also the material absorption, in the guided region. However, high absorption is not limited to wavelengths in the UV. Silica glass also heavily absorbs infra-red (IR) radiation (Kitamura et al. 2007). The high extinction coefficient in the IR is due to the absorption of the light by the vibration bonds in $SiO_2$ (Siesler 2008). In this chapter I performed all of the work myself with the exception of the derivation from (Bird 2017), i.e. equation (5.1) to equation (5.47).

The wavelengths of interest are those between 2.8 μm and 10 μm, where applications and absorption is high. To give an example of the extent of loss in glass in the IR, at 2.8 μm the loss is 39 dB/m where the extinction coefficient is $2{\cdot}10^{-6}$ whilst at 10 μm the loss rises to approximately $1{\cdot}10^{6}$ dB/m where the extinction coefficient is 0.2. Similarly to the solution for the UV, a HCNCF structure could be used to allow for guidance at these wavelengths. Looking at the contrast of the losses at 2.8 μm and 10 μm different forms of HCNCF would be necessary to allow low loss propagation at these wavelengths due to the distance the light would propagate in the silica tube walls of the fibre before being reflected back into the core. For example, if the light was travelling normal to a glass wall to minimise the distance travelled. For a fibre ideally designed for 2.8 μm (between $m = 1$ and $m = 2$) that tube wall thickness would be 2 μm meaning the loss would be $1.6 \cdot 10^{-4}$ dB which would allow for the antiresonant effect to take place (section 5.1). On the other hand at 10 μm (between $m = 1$ and $m = 2$) with a tube wall thickness of 2.8 μm the loss would be 6.2 dB which is too high to take advantage of the enhanced reflection provided by the antiresonant effect. Therefore, a pure silica glass HCNCF would guide using via glancing angle guidance at 10 μm rendering the benefit of multiple reflections from antiresonant guidance redundant. Section 5.2 investigates a possible solution to using this type of negative-curvature structure but instead of glass, using a metal.

## 5.1 Guiding in the near-IR

Building a HCNCF for the IR requires the same techniques as explained in section 2.2. Although the challenges are similar to those posed by manufacturing fibres for shorter wavelengths there are some notable differences which lead to an improvement in reliability of the building process. There are two significant differences which makes these fibre easier to manufacture. Firstly, the capillary walls are significantly thicker than for HCNCF designed to guide the visible or shorter wavelengths. This means that

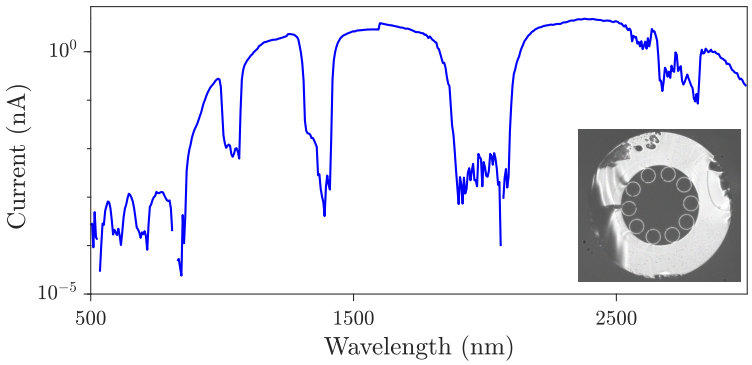


Figure 5-1: Transmission of a 10 m length of fibre. The $m = 1$ resonance (not shown) is located at 4 µm, the $m = 2$ is at 2 µm, $m = 3$ is at 1.4 µm and $m = 4$ is located at 1 µm. The lowering of the transmission about 2.8 µm is due to the O-H absorption at those wavelengths. The inset shows an optical micrograph of the fibre's cross-section. The physical parameters are as follows, number of tubes 10, outer diameter 290 $\pm$ 2 µm, core diameter 92 $\pm$ 1 µm, tube outer diameter 30 $\pm$ 1 µm and a wall thickness of 1.95 $\pm$ 0.1 µm.

the capillaries in the stacking tube do not flex as much in the region where they are not supported by the central support tube which increases the chances of them being fused to the outer wall after drop-off. Secondly, the increase in wall thickness makes the active pressurisation of these capillaries more stable. Small variations in the outer diameter of the capillaries are not exaggerated to the same extent when inflated.

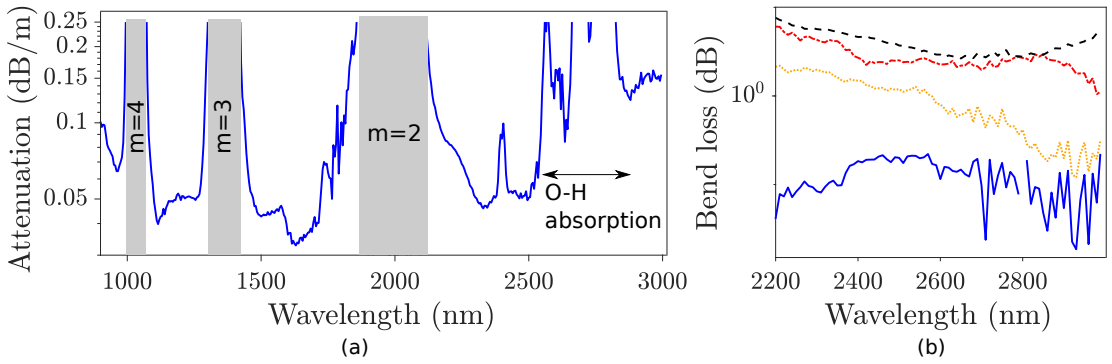


Figure 5-2: (a) Cut-back measurement where the long length was 54 m and the short length was 10 m. The loss peak around 2.8 µm is due to O-H absorption in the atmosphere. The $m = 2$ resonance is located at 2 µm. (b) Bend loss measurements between the $m = 1$ and $m = 2$ resonance. The solid blue curve was for a bend radius of 10 cm, the dotted orange curve represents a bend radius of 5 cm, the red dash-dot line was for a bend radius of 2.5 cm and the final black dashed line represents the loss after a 1 cm bend. The set-up used was that represented in figure 2-8(a) where there was a 180° half-bend.

Figure 5-1 shows the transmission curve of a 10 m piece and cross-section of the optical fibre (inset). The experimental set-up which produced the transmission curve comprised of a tungsten lamp which was butt-coupled into the optical fibre with the output being measured by a spectrometer (Bentham DTMc300). The fibre has an outer diameter of 290 $\pm$ 2 µm, core diameter 92 $\pm$ 1 µm, tube outer diameter 30 $\pm$ 1 µm and a wall thickness of 1.95 $\pm$ 0.1 µm. The fibre was designed to emulate the performance of the IR-fibre in (Love 2018), which was to guide 2.5 to 3 µm between the $m = 1$ resonance at 4 µm and the $m = 2$ resonance at 2 µm. Figure 5-1 shows that this fibre matches this transmission criteria. The reduction in the transmission around 2.8 µm is due to the O-H absorption (Weir et al. 1959). The cut-back measurement is represented in figure 5-2(a) which covers the regions of interest, wavelengths between the $m = 1$ and $m = 2$ resonance. The cut-back length was from 54 m to 10 m. The loss can be seen to drop down to about 0.05 dB/m. However, the increase in loss between 2.5 µm and 2.85 µm is due to the O-H absorption. A solution would be to purge the fibres in a vacuum in order to remove the O-H absorption so the loss at 2.5 µm and 2.85 µm can be measured.

The close spacing and uniformity of the tube walls of the optical fibre indicate that the fibre should perform well in terms of bend loss. Moreover the core diameter to wavelength ratio is about 33 which is ideal in the balance between confinement and bend loss. Figure 5-2(b) shows four bend loss curves. the bend loss measured different bend radii for wavelengths between the $m = 1$ and $m = 2$ resonance. The optical set-up was based around that in figure 2-8(a) to omit higher order modes in order to measure the bend loss of the fundamental mode. Due to the core diameter to wavelength ratio the loss is relatively low with a bend radius of 1 cm which was measured to be 4.5 dB. For larger bends the loss becomes tolerable to be used for a variety of applications as shown for the bend radii of 10 cm and 5 cm which reported losses of 0.1 dB and 0.4 dB around 2.8 µm. Secondly, the bend loss starts to increase towards the resonance as the light

interacts more with the glass, which means those already high-loss wavelengths near the resonance become more lossy. When comparing the loss in figure 5-2(b) to that of the 22 tube multimode fibre shown in figure 3-6 the fibre presented here is shown to guide fewer modes. This can be seen from how the bend loss behaves as the bend radius is decreased. Figure 3-6 shows an immediate increase in the bend loss between $m = 1$ and $m = 2$ with relatively large bends whilst the increase in the loss between the bends in this optical fibre only becomes significant at very small bends such as for a bend radius of 2.5 cm, away from the resonance.

The problems which are faced in the VUV are similar to those in the IR with respect to the absortion characteristics of silica glass. The fibre shown here demonstrates the repeatability of manufacturing of a HCNCF for the IR. However, 2.8 μm can be considered to be on the shorter side for the IR. The next section represents the push to developing a fibre to guide 10 μm, a wavelength where the loss is significantly greater and thus new problems need to be overcome.

## 5.2 Metal coated hollow-core negative curvature fibres for 10 μm guidance

It was shown that hollow-core negative curvature fibre can guide near and mid-IR wavelengths. Due to the hollow-core and broadband transmissions these types of fibres have found applications for high-power delivery and guidance into the mid-IR (Yu et al. 2012, Poletti 2014, Hassan et al. 2016, Debord et al. 2017, Van Putten et al. 2016). However, it was also shown that when moving deeper into the IR, beyond 4 μm the extinction coefficient of the glass rises rapidly rendering the use of silica glass 'inappropriate'. Therefore a different material needs to be used to make viable fibres at these wavelengths.

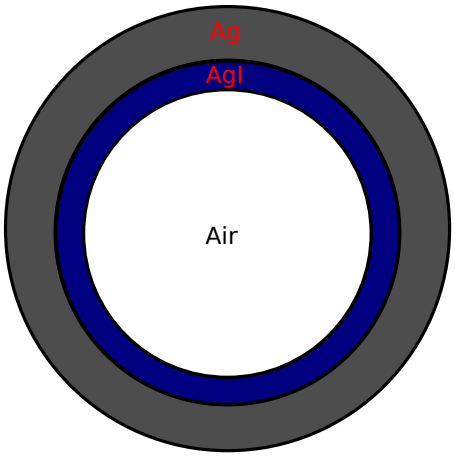


Figure 5-3: Schematic of the Bragg fibre model used in the analysis. Core material is air (white) with radius of 150 μm, refractive index is 1 and an extinction coefficient of 0. The air core is followed by a AgI layer (blue) which ranges in thickness between 0 to 7 μm, refractive index of 2 and an extinction coefficient of 0. The final layer (grey) is made of Ag which has a thickness of 25 μm, refractive index of 11 and extinction coefficient of 70, and extends to $r = \infty$ in the model.

Currently the optical fibres which do guide these wavelengths are cylindrical in shape and consist of an air core surrounded by a dielectric layer which is then surrounded by a metal layer. The cladding of the structure is made of silica glass (figure 5-3). The fibre's guidance mechanism makes use to the antiresonant effect with the thickness of the dielectric layer determining the location of the resonances. The issue with this structure is that it produces a high confinement loss with the state of art commercial examples producing losses of 1 dB/m due to the light scattering off the dielectric surface. The hypothesis for this section is whether or not a HCNCF with a metal boundary on the inside of the tubes produces a lower loss than its cylindrical fibre counterpart.

Although there is currently no analytical solution which can describe the loss in a HCNCF, the metal and dielectric cylindrical fibre has been extensively studied (Yeh et al. 1978, Bird 2017). Before moving onto a structure with a metal layer it would be beneficial to set-up a dielectric cylindrical Bragg fibre model. The following is based on the analysis from (Bird 2017).

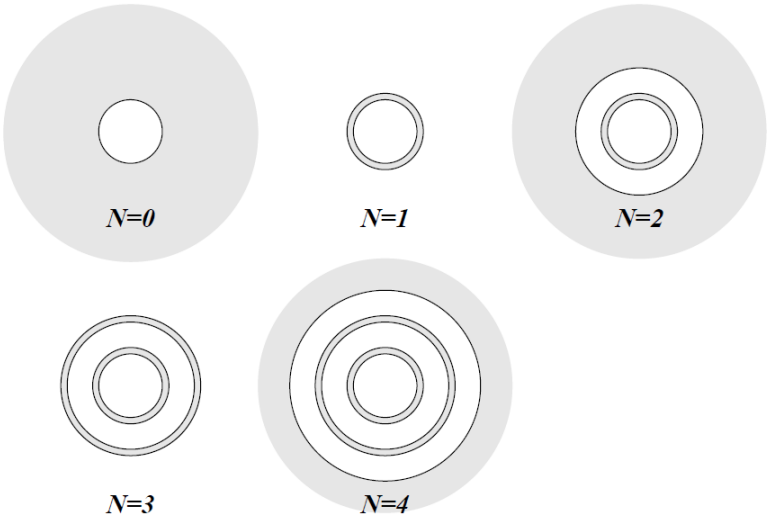


Figure 5-4: Schematic diagram of glass-air multi-layered structures. Air regions are white, glass regions are shaded, and black lines represent the boundaries between layers. $N$ refers to the number of complete anti-resonant layers in each structure: $N = 0$ represents a hollow glass tube; $N = 1$ a thin-walled capillary; $N = 2$ a jacketed capillary; $N = 3$ two nested capillaries; $N = 4$ as for $N = 3$ but with an outer glass jacket. In each case the outermost region extends to infinity. (Bird 2017)

Consider a cylindrically symmetric structure which is uniform along its length ($z$ direction) which consists of concentric regions of glass with a relative dielectric constant $\epsilon$ and air, $\epsilon_{air} = 1$. The inner most region is filled with air, the outer most is assumed to extend to infinity with each structure being labelled by an integer $N$ which represents the number of complete finite layers (figure 5-4).

Using a cylindrical coordinate system $(r, \theta, z)$ where positive $z$ is taken a the direction of propagation. The field components follow the form,

$$\Psi(r, \theta, z, t) = \Psi(r, \theta) e^{i(\beta z - \omega t)} \tag{5.1}$$

where $\Psi$ represent the field component $E_r, E_\theta, E_z, H_r, H_\theta$ and $H_z$. $\beta$ is the complex propagation constant that needs to be solved for, $\omega$ is the angular frequency and $i$ is the imaginary unit. Due to the nature of anti-resonant guidance, there will be inward and

outward traveling waves. Therefore, Hankel functions of the first ($H^{(1)}$) and second ($H^{(2)}$) are more appropriate than Bessel functions to use,

$$H_l^{(1)} = J_l(x) + iY_l(x) \tag{5.2}$$

and

$$H_l^{(2)} = J_l(x) - iY_l(x), \tag{5.3}$$

where $J_l(x)$ and $Y_l(x)$ are the Bessel functions of the first and second kind.

The $z$-component of the electric and magnetic fields are given as,

$$E_z(r,\theta) = [(A_j H_l^{(1)}(k_j r) + B_j H_l^{(1)}(k_j r)] \cos(l\theta + \phi) \tag{5.4}$$

and

$$\tilde{H}_z(r,\theta) = [(C_j H_l^{(1)}(k_j r) + D_j H_l^{(1)}(k_j r)] \sin(l\theta + \psi), \tag{5.5}$$

where $A, B, C, D, \phi$ and $\psi$ are constants and $l$ is an integer which represents the order of the Hankel function. The variable $j$ represents the regions of the guiding layer structure starting at 1 for the core region increasing radially to adjacent layers. Due to the dielectric material $\tilde{H}_z$ is defined as (Yeh et al. 1978)

$$\tilde{H}_z(r,\theta) = \left(\frac{\mu_0}{\epsilon_0}\right)^{\frac{1}{2}} H_z(r,\theta) \tag{5.6}$$

The transverse wavevector in each region $j$ is defined as,

$$k_j = (k_0^2 \epsilon_j - \beta^2)^{\frac{1}{2}} \tag{5.7}$$

where $k_0$ is the free-space wavevector and $\epsilon_j$ is the dielectric constant of region $j$. The other field components are given as a function of $E_z$ and $\tilde{H}_z(r,\theta)$

$$E_r(r,\theta) = \frac{i}{k_j^2}\left[\beta\frac{\partial E_z}{\partial r} + \frac{k_0}{r}\frac{\tilde{H}_z}{\partial\theta}\right], \tag{5.8}$$

$$E_\theta(r,\theta) = \frac{i}{k_j^2}\left[\frac{\beta}{r}\frac{\partial E_z}{\partial\theta} - k_0\frac{\tilde{H}_z}{\partial r}\right], \tag{5.9}$$

$$\tilde{H}_r(r,\theta) = \frac{i}{k_j^2}\left[\beta\frac{\partial \tilde{H}_z}{\partial r} - \frac{k_0\epsilon}{r}\frac{E_z}{\partial\theta}\right], \tag{5.10}$$

and

$$\tilde{H}_\theta(r,\theta) = \frac{i}{k_j^2}\left[\frac{\beta}{r}\frac{\partial \tilde{H}_z}{\partial\theta} - k_0\epsilon\frac{E_z}{\partial r}\right]. \tag{5.11}$$

The boundary conditions for this model require $E_z$, $H_z$, $E_\theta$ and $H_\theta$ to be continuous across each interface in the structure. This condition is used to derive the relationship between $A_j, B_j, C_j, D_j$ coefficients and $A_{j+1}, B_{j+1}, C_{j+1}, D_{j+1}$ coefficients in the adjacent layer.

The formulism presented in (Yeh et al. 1978) looks to find the matrix $\mathbf{M}$ that relates these field coefficients by

$$\begin{pmatrix} A_{j+1} \\ B_{j+1} \\ C_{j+1} \\ D_{j+1} \end{pmatrix} = \mathbf{M} \begin{pmatrix} A_j \\ B_j \\ C_j \\ D_j \end{pmatrix}. \tag{5.12}$$

Deriving the matrix $\mathbf{M}$ is done in the following way. Consider layer $j = 1$. The continuity of the $E_z$ component at the boundary between two layers at $r = \rho$ gives,

$$[A_1 H_l^{(1)}(k_1\rho) + B_1 H_l^{(2)}(k_1\rho)]\cos(l\theta + \phi_1) = \\ [A_2 H_l^{(1)}(k_2\rho) + B_2 H_l^{(2)}(k_2\rho)]\cos(l\theta + \phi_2) \quad (5.13)$$

The equation needs to be satisfied azimuthally i.e. for all $\theta$ is means that

$$\phi_1 = \phi_2 \quad (5.14)$$

and similarly for the continuity of $H_z$,

$$\psi_1 = \psi_2. \quad (5.15)$$

Since $l$ is an integer which represents the Hankel function order it is kept constant across the structure for mode solutions the trigonometric terms cancel each other out. Therefore, the continuity condition of $E_z$ and $H_z$ across a boundary is given as,

$$A_1 H_l^{(1)}(k_1\rho) + B_1 H_l^{(2)}(k_1\rho) = A_2 H_l^{(1)}(k_2\rho) + B_2 H_l^{(2)}(k_2\rho) \quad (5.16)$$

$$C_1 H_l^{(1)}(k_1\rho) + D_1 H_l^{(2)}(k_1\rho) = C_2 H_l^{(1)}(k_2\rho) + D_2 H_l^{(2)}(k_2\rho) \quad (5.17)$$

The continuity of the $E_\theta$ component (equation 5.9) is

$$\frac{i}{k_1^2}(-\frac{l\beta}{\rho}\left[A_1 H_l^{(1)}(k_1\rho) + B_1 H_l^{(2)}(k_1\rho)\right]\sin(l\theta + \phi) \\ - k_0 k_1\left[C_1 H_l^{(1)'}(k_1\rho) + D_1 H_l^{(2)'}(k_1\rho)\right]\cos(l\theta + \psi)) = \\ \frac{i}{k_2^2}(-\frac{l\beta}{\rho}\left[A_2 H_l^{(1)}(k_2\rho) + B_2 H_l^{(2)}(k_2\rho)\right]\sin(l\theta + \phi) \\ - k_0 k_2\left[C_2 H_l^{(1)'}(k_2\rho) + D_2 H_l^{(2)'}(k_2\rho)\right]\cos(l\theta + \psi)) \quad (5.18)$$

where the prime represents the derivative with respect to its own argument. As stated before this needs to be satisfied to all $\theta$. We know that $k_1 \neq k_2$ the coefficients of the sin and cos terms are not equal. Therefore, in order to preserve the azimuthal condition a relationship must be found which equations these trigonometric terms,

$$\sin(l\theta + \phi) = \pm\cos(l\theta + \psi) \tag{5.19}$$

which leads to

$$\phi = \psi \pm \frac{\pi}{2} \tag{5.20}$$

Moving on to the $\tilde{H}_\theta$ from equation 5.11 give

$$\begin{aligned}\frac{i}{k_1^2}(-\frac{l\beta}{\rho}&\left[C_1 H_l^{(1)}(k_1\rho) + D_1 H_l^{(2)}(k_1\rho)\right]\sin(l\theta+\phi)\\ &- k_0 k_1 \epsilon_1 \left[A_1 H_l^{(1)'}(k_1\rho) + B_1 H_l^{(2)'}(k_1\rho)\right]\cos(l\theta+\psi))\\ &= \frac{i}{k_2^2}(-\frac{l\beta}{\rho}\left[C_2 H_l^{(1)}(k_2\rho) + D_2 H_l^{(2)}(k_2\rho)\right]\sin(l\theta+\phi)\\ &\quad - k_0 k_2 \epsilon_2 \left[A_2 H_l^{(1)'}(k_2\rho) + B_2 H_l^{(2)'}(k_2\rho)\right]\cos(l\theta+\psi))\end{aligned} \tag{5.21}$$

Using the relationship between $\phi$ and $\psi$ there are two possible solutions which can be obtained for each solution. For example, if $\phi = 0$ then $\psi = -\frac{\pi}{2}$ (set $I$). Likewise if $\phi = -\frac{\pi}{2}$ then $\psi = 0$ (set $II$).

$$I \quad E_z = [(AH_l^{(1)}(kr) + BH_l^{(2)}(kr)]\cos(l\theta) \tag{5.22}$$

$$H_z = [(CH_l^{(1)}(kr) + DH_l^{(2)}(kr)]\sin(l\theta) \tag{5.23}$$

$$II \quad E_z = [(AH_l^{(1)}(kr) + BH_l^{(2)}(kr)]\sin(l\theta) \tag{5.24}$$

$$H_z = [(CH_l^{(1)}(kr) + DH_l^{(2)}(kr)]\cos(l\theta) \tag{5.25}$$

Looking for solutions in set $I$ by setting $\phi = 0$ then $\psi = -\frac{\pi}{2}$ the trigometric terms in equations (5.18) and (5.21) can be dropped. The notation of $(1 \to 2)$ from (Yeh et al. 1978) $(1 \to 2)$ is used to represent the same terms except that the subscript 1 are replaced with a 2. The final forms of the boundary conditions are

$$A_1 H_l^{(1)}(k_1\rho) + B_1 H_l^{(2)}(k_1\rho) + 0 + 0 = (1 \to 2), \tag{5.26}$$

$$\frac{k_0\epsilon_1}{k_1} A_1 H_l^{(1)'}(k_1\rho) + \frac{k_0\epsilon_1}{k_1} B_1 H_l^{(2)'}(k_1\rho) + \frac{l\beta}{k_1^2\rho} C_1 H_l^{(1)}(k_1\rho) + \frac{l\beta}{k_1^2\rho} D_1 H_l^{(2)}(k_1\rho) = (1 \to 2), \tag{5.27}$$

$$0 + 0 + C_1 H_l^{(1)}(k_1\rho) + D_1 H_l^{(2)}(k_1\rho) = (1 \to 2), \tag{5.28}$$

and

$$\frac{l\beta}{k_1^2\rho} A_1 H_l^{(1)}(k_1\rho) + \frac{l\beta}{k_1^2\rho} B_1 H_l^{(2)}(k_1\rho) + \frac{k_0}{k_1} C_1 H_l^{(2)'}(k_1\rho) + \frac{k_0}{k_1} D_1 H_l^{(2)'}(k_1\rho) = (1 \to 2) \tag{5.29}$$

The formulae can be written in a matrix form

$$M(1,\rho) \begin{pmatrix} A_1 \\ B_1 \\ C_1 \\ D_1 \end{pmatrix} = M(2,\rho) \begin{pmatrix} A_2 \\ B_2 \\ C_2 \\ D_2 \end{pmatrix} \tag{5.30}$$

where

$$M(j,\rho) = \begin{bmatrix} H_l^{(1)}(k_j\rho) & H_l^{(2)}(k_j\rho) & 0 & 0 \\ \frac{k_0\epsilon_j}{k_j}H_l^{(1)'}(k_j\rho) & \frac{k_0\epsilon_j}{k_j}H_l^{(2)'}(k_j\rho) & \frac{l\beta}{k_j^2\rho}H_l^{(1)}(k_j\rho) & \frac{l\beta}{k_j^2\rho}H_l^{(2)}(k_j\rho) \\ 0 & 0 & H_l^{(1)}(k_j\rho) & H_l^{(2)}(k_j\rho) \\ \frac{l\beta}{k_j^2\rho}H_l^{(1)}(k_j\rho) & \frac{l\beta}{k_j^2\rho}H_l^{(2)}(k_j\rho) & \frac{k_0}{k_j}H_l^{(1)'}(k_j\rho) & \frac{k_0}{k_j}H_l^{(2)'}(k_j\rho) \end{bmatrix} \tag{5.31}$$

Now that we have the final matrix form which needs to be used it is possible to solve for $\beta$. Equation (5.30) can be re-written as

$$\begin{pmatrix} A_1 \\ B_1 \\ C_1 \\ D_1 \end{pmatrix} = M(1,\rho)^{-1}M(2,\rho) \begin{pmatrix} A_2 \\ B_2 \\ C_2 \\ D_2 \end{pmatrix} \tag{5.32}$$

where there is one inverse-matrix pair for each boundary layer in the structure. Therefore, by considering the successive layers the coefficients in the final layer can be calculated as,

$$\begin{pmatrix} A_f \\ B_f \\ C_f \\ D_f \end{pmatrix} = M^{-1}(f,\rho_f)M(N,\rho_f)M^{-1}(N,\rho_{N-1})M(N-1,r_{N-1})...M^{-1}(1,\rho_c)M(c,\rho_c) \begin{pmatrix} A_c \\ B_c \\ C_c \\ D_c \end{pmatrix} \tag{5.33}$$

where $N$ represents the number of complete anti-resonant layers, $c$ is the core, $f$ is the final infinitely long outer region and $r_j$ is the $j$th radius from the center of the model.

Solving equation (5.33) for $\beta$ requires looking at the properties of the Hankel functions. As $r \to 0$ then $Y \to$ inf where $Y$ is the Bessel function of the second kind.

Therefore for solutions to remain finite at $r = 0$ we need,

$$A_c = B_c \quad \text{and} \quad C_c = D_c \tag{5.34}$$

in order for the $Y$ Bessel function terms in equations (5.4) and (5.5) will cancel at $r = 0$. Another condition is that there are no incoming waves from outside the structure which means that

$$B_f = 0 \quad \text{and} \quad D_f = 0. \tag{5.35}$$

These conditions allow for $\beta$ to be obtained and hence the individual modal attenuation of the structure. As the loss in dB, $\alpha_{\text{dB}}$, is calculated as,

$$\alpha_{\text{dB}} = \beta \cdot 20 \ln(10) \tag{5.36}$$

Parameterising the terms into dimensionless parameters $x$ and $D$ to aid in reducing the number of parameters is done by,

$$x = k_c r_c = (k_0^2 - \beta^2)^{\frac{1}{2}} r_c \quad \text{and} \quad D = k_0 r_c = \frac{2\pi}{\lambda_0} r_c. \tag{5.37}$$

From equation (5.7) and taking the core dielectric constant $\epsilon = 1$ the propagation constant can be expressed as

$$\beta = k_0 \left(1 - \frac{x^2}{D^2}\right)^{\frac{1}{2}}. \tag{5.38}$$

Re-writing matrix (5.31) in terms of the dimensionless variables yields,

$$k_j r = \frac{r}{r_c} D(\epsilon_j - 1 + \frac{x^2}{D^2})^{\frac{1}{2}}, \quad \frac{k_0}{k_j} = \frac{1}{(\epsilon_j - 1 + \frac{x^2}{D^2})^{1/2}}, \quad \frac{l\beta}{k_j^2 r} = \frac{r_c}{r} \frac{l}{D} \frac{(1 - \frac{x^2}{D^2})^{1/2}}{(\epsilon_j - 1 + \frac{x^2}{D^2})}. \tag{5.39}$$

To simplify the equations we set $G$ as

$$G_j = \frac{(1-\frac{x^2}{D^2})^{1/2}}{(\epsilon_j - 1 + \frac{x^2}{D^2})} \tag{5.40}$$

The parameterised versions of the matrices are written as

$$M(j,\rho) = \begin{bmatrix} H_l^{(1)}(k_j\rho) & H_l^{(2)}(k_j\rho) & 0 & 0 \\ \frac{\epsilon_j H_l^{(1)'}(k_j r)}{(\epsilon_j - 1 + \frac{x^2}{D^2})^{\frac{1}{2}}} & \frac{\epsilon_j H_l^{(2)'}(k_j r)}{(\epsilon_j - 1 + \frac{x^2}{D^2})^{\frac{1}{2}}} & \frac{r_c}{r}\frac{l}{D} G_j H_l^{(1)}(k_j r) & \frac{r_c}{r}\frac{l}{D} G_j H_l^{(2)}(k_j r) \\ 0 & 0 & H_l^{(1)}(k_j\rho) & H_l^{(2)}(k_j\rho) \\ \frac{r_c}{r}\frac{l}{D} G_j H_l^{(1)}(k_j r) & \frac{r_c}{r}\frac{l}{D} G_j H_l^{(2)}(k_j r) & \frac{H_l^{(1)'}(k_j r)}{(\epsilon_j - 1 + \frac{x^2}{D^2})^{\frac{1}{2}}} & \frac{H_l^{(2)'}(k_j r)}{(\epsilon_j - 1 + \frac{x^2}{D^2})^{\frac{1}{2}}} \end{bmatrix} \tag{5.41}$$

and

$$M^{-1}(j,\rho) = \begin{bmatrix} \frac{H_l^{(2)'}(k_j r)}{(\epsilon_j - 1 + \frac{x^2}{D^2})^{\frac{1}{2}}} & -\frac{1}{\epsilon_j} H_l^{(2)}(k_j r) & \frac{r_c}{r}\frac{l}{\epsilon_j D} G_j H_l^{(2)}(k_j r) & 0 \\ -\frac{H_l^{(1)'}(k_j r)}{(\epsilon_j - 1 + \frac{x^2}{D^2})^{\frac{1}{2}}} & \frac{1}{\epsilon_j} H_l^{(1)}(k_j r) & -\frac{r_c}{r}\frac{l}{\epsilon_j D} G_j H_l^{(1)}(k_j r) & 0 \\ \frac{r_c}{r}\frac{l}{D} G_j H_l^{(2)}(k_j r) & 0 & \frac{H_l^{(2)'}(k_j r)}{(\epsilon_j - 1 + \frac{x^2}{D^2})^{\frac{1}{2}}} & -H_l^{(2)}(k_j\rho) \\ -\frac{r_c}{r}\frac{l}{D} G_j H_l^{(1)}(k_j r) & 0 & -\frac{H_l^{(1)'}(k_j r)}{(\epsilon_j - 1 + \frac{x^2}{D^2})^{\frac{1}{2}}} & H_l^{(1)}(k_j r) \end{bmatrix} \times \frac{r}{r_c}\frac{i\pi}{4} D(\epsilon_j - 1 + \frac{x^2}{D^2}) \tag{5.42}$$

The terms $D, \epsilon, l, r/r_c$ all of which are defined by the structure of the model and also $x$. The dimensionless parameter $D$ is set by the structure and is therefore invariant for a fixed wavelength. On the other hand $x$ is the parameter which needs to be found in order to determine $\beta$. To find $x$ a minimisation procedure needs to be implemented.

The satisfy the conditions set by (5.34) we set

$$\begin{pmatrix} A_c \\ B_c \\ C_c \\ D_c \end{pmatrix} = \begin{pmatrix} 1 \\ 1 \\ P \\ P \end{pmatrix} \tag{5.43}$$

where $P$ is the value to be determined. Using this condition equation (5.33) can be re-written as,

$$\begin{pmatrix} A_f \\ B_f \\ C_f \\ D_f \end{pmatrix} = \begin{bmatrix} m_{11}(x) & m_{12}(x) & m_{13}(x) & m_{14}(x) \\ m_{21}(x) & m_{22}(x) & m_{23}(x) & m_{24}(x) \\ m_{31}(x) & m_{32}(x) & m_{33}(x) & m_{34}(x) \\ m_{41}(x) & m_{42}(x) & m_{43}(x) & m_{44}(x) \end{bmatrix} \begin{pmatrix} 1 \\ 1 \\ P \\ P \end{pmatrix} \tag{5.44}$$

The conditions set by (5.35) can be used to determine the value of $P$ for a given value of $x$. Since both $B_f = 0$ and $D_f = 0$ we can use one of them to obtain a value for $P$ for a value of $x$ and then use the other term as the minimisation parameter. For example, using $B_f$ to get a value of $P$ is done in the following way. Starting from

$$B_f(x, P) = (m_{21}(x) + m_{22}(x) + Pm_{23}(x) + Pm_{24}(x)) = 0, \tag{5.45}$$

and making $P$ the subject,

$$P = \frac{-(m_{21}(x) + m_{22}(x))}{(m_{23}(x) + m_{24}(x))}. \tag{5.46}$$

Now we need the find the value of $x$ which minimises,

$$|D_f(x, P)|^2 = |m_{41}(x) + m_{42}(x) + P(m_{43}(x) + m_{44}(x))|^2 = 0.$$

$$|D_f(x, B_f = 0)|^2 = |m_{41}(x) + m_{42}(x) + \frac{-(m_{21}(x) + m_{22}(x))}{(m_{23}(x) + m_{24}(x))}(m_{43}(x) + m_{44}(x))|^2 = 0. \quad (5.47)$$

Once equation (5.47) has been minimised, the value of $x$ can be used to obtain the propagation constant $\beta$ and hence the loss. For each value of $l$ there will be multiple values of $x$ that satisfy equation (5.47), which define separate modes in the structure. It must be noted that with $l = 0$, matrices (5.41) and (5.42) are simplified such that the four elements top right and bottom left are all equal to zero. Furthermore the top left block represents TM mode solutions as both $H_z$ and $E_\theta$ equal zero whilst the four in the bottom right block result in TE solutions as $E_z$ and $H_\theta$ are equal to zero. The formulation described thus far is well known for *standard* hollow-fibre structure where the material oscillates between glass and air layers. However, it was also shown that in order to guide a wavelength of 10 μm silica glass is not a suitable material due the its high extinction coefficient at those wavelengths. Current commercial state-of-the-art fibres use a metal coating as the last boundary material with the first layer being between air and a dielectric material which is low loss at those wavelengths, such as AgI (Kriesel et al. 2011). In the outermost metal region of the model the value of $k_f r_N$ becomes very large which causes the Hankel function calculation to blow up and so cannot be computed. In order to tackle this, the final matrix ($M^{-1}$) in equation (5.33) needs to be modified. We know that,

$$\begin{pmatrix} A_f \\ B_f \\ C_f \\ D_f \end{pmatrix} = M^{-1}(k_f, r_N) \begin{pmatrix} A(P) \\ B(P) \\ C(P) \\ D(P) \end{pmatrix} \quad (5.48)$$

Where $A, B, C, D$ are all functions of the parameter $P$. We know $B_f = 0$ and $D_f = 0$, so focusing on the second and fourth row of the matrices on the RHS we get,

$$B_f = 0 = -\frac{A(P)}{(\epsilon_j - 1\frac{x^2}{D^2})^{1/2}} H_l^{(1)}(k_j r) + \frac{B(P)}{\epsilon_j} H_l^{(1)}(k_j r) - \frac{C(P) r_c}{r} \frac{l}{\epsilon_j D} G_j H_l^{(1)}(k_j r) \tag{5.49}$$

and

$$D_f = 0 = -\frac{A(P) r_c}{r} \frac{l}{\epsilon_j D} G_j H_l^{(1)}(k_j r) - \frac{C(P)}{(\epsilon_j - 1\frac{x^2}{D^2})^{1/2}} H_l^{(1)}(k_j r) + D(P) H_l^{(1)}(k_j r) \tag{5.50}$$

It can be seen that when multiplied out both are purely functions of $H_l^1$ only. The significance of this means that $H_l^1$ can be scaled in such a way that the calculation in the metal layer becomes manageable. The Hankel functions are exponentially scaled such that,

$$H_l^{(1)e} = H_l^{(1)} e^{-ik_f r_N} \tag{5.51}$$

where $H_l^{(1)e}$ is the exponentially scaled Hankel function of the first kind. With this substitution a solution for $x$ and hence $\beta$ can now be found.

Finding the correct solution for $x$ relies on choosing the right starting value as there are multiple valleys in the phase space the minima in which contain the correct value of $x$ for a given mode. Furthermore an efficient minimisation algorithm needs to be implemented, in this case the Nelder-Mead method was used due to its good performance in low-dimensional problems (Gao and Han 2012).

The Bragg fibre model that was simulated was based on a popular structure used to guide 10 μm (Gao and Han 2012, Sampaolo et al. 2015, Lin et al. 2009, George and

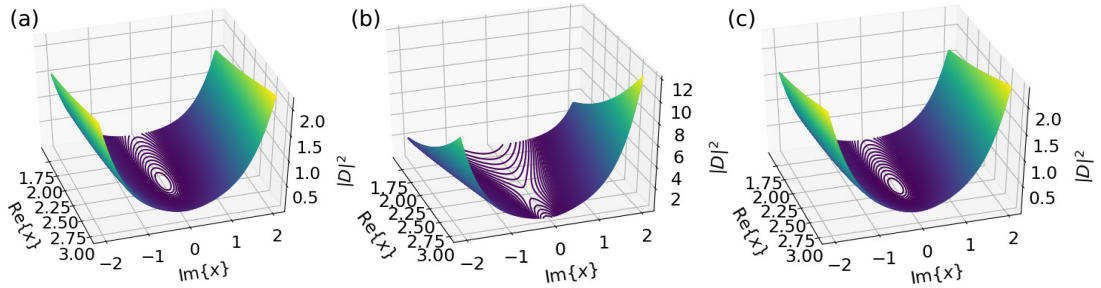


Figure 5-5: Parameter sweep of the $HE_{11}$ mode for different values of $\Re(x)$ and $\Im(x)$ used in the minimisation of $|D|^2$. The model here is that represented in figure 5-3. (a) Corresponds to a dielectric layer thickness of 2.0 µm which is away from a resonance. (b) A thickness of 2.9 µm which is at a resonance and (c) 3.7 µm which is away from resonance.

Harrington 2005). It consisted of an air core surrounded by a layer of AgI and then Ag. The cladding material is ignored in the model and the metal is assumed to be infinitely thick ($r_{\text{metal}} \to \infty$) making the effect of a cladding on the propagation of the light irrelevant (Fox 2002). Figure 5-3 shows a schematic of the optical fibre model used in this analysis. It has an air core (white) which has a radius set to 150 µm, refractive index of 1 and extinction coefficient of 0. The next layer is made of the dielectric material AgI (blue) which has a thickness which ranges from 0 to 7 µm, a refractive index of 2 and an extinction coefficient of 0. The final outer layer (grey) is made of Ag and is infinitely thick. The refractive index and extinction coefficient is 11 and 70 respectively.

Figure 5-5 shows the importance of choosing the correct value of $x$ to start with. It shows the phase space of $|D|^2$ for different values of $\Re(x)$ and $\Im(x)$. The mode sampled here is the $HE_{11}$ for the same structure represented in figure 5-3. Three sub-figures are shown with (a), (b) and (c) corresponding to a dielectric layer thickness of 2.0 µm (away from resonance), 2.9 µm (at resonance) and 3.7 µm (away from resonance). It can be seen that the values of $\Re(x)$ and $\Im(x)$ which minimise $|D|^2$ lie in valleys where between the peaks are other minima of $|D|^2$ which correspond to other modes (one minima shown here). Therefore, the starting guess $\Re(x)$ and $\Im(x)$ is crucial finding the values of $x$ which does minimise $|D|^2$. This was done in two steps. Firstly by keeping $\Im(x) = 0$ fixed but letting $\Re(x) = y$ vary, $l$ is an integer defining the mode and $y$

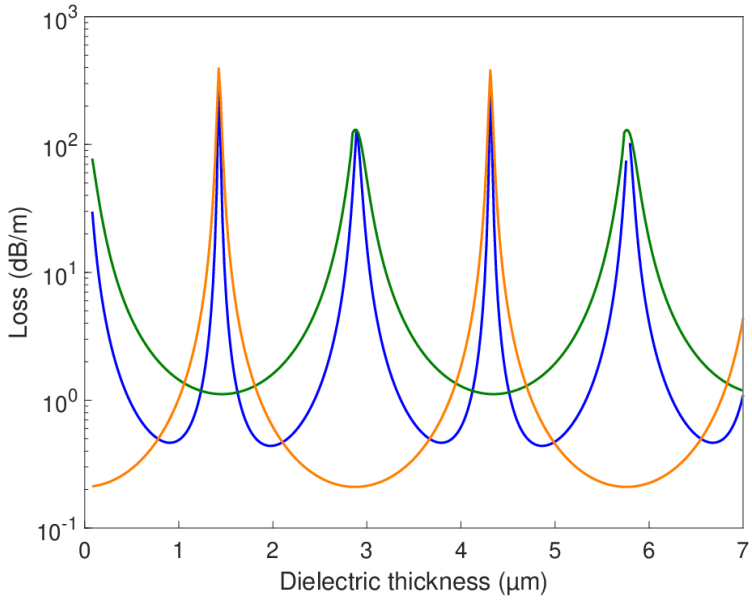


Figure 5-6: Loss curves versus dielectric layer thickness for modes the $HE_{11}$ (blue), $TE_{01}$ (orange) and $TM_{01}$ (green). The dielectric thickness ranged from 0.1 to 7 μm. The high-loss resonances which are separated by a low loss region confirm that this model is guiding via antiresonant guidance.

corresponds to the $m$th zero of the Bessel function such that $J_l(y) = 0$. The second step was to vary both $\Im(x)$ and $\Re(x)$ but using 0 as the starting point for $\Im(x)$ and the minimum value from the first step for $\Re(x)$.

The loss curves shown in figure 5-6 demonstrate the attenuation behaviour of the $HE_{11}$ (blue), $TE_{01}$ (orange) and $TM_{01}$ (green) modes as a function of the dielectric layer thickness for the model in figure 5-3. The wavelength used was 10 μm. It can be seen that the loss contains high resonance peaks which are separated by a low loss region confirming that antiresonant guidance is taking place. The loss for the $HE_{11}$ mode follows the combined behaviour of the $TE_{01}$ and $TM_{01}$. One very interesting aspect of this feature is that the loss curves of the $TE_{01}$ and $TM_{01}$ are shifted from each other. This result is explained through the Fresnel equations for reflection coefficients $r$ which

are given as (Hecht 2016),

$$\text{TE case:} \quad r_{\text{TE}} = \frac{\cos(\theta_i) - \sqrt{\dot{n}^2 - \sin^2(\theta_i)}}{\cos(\theta_i) + \sqrt{\dot{n}^2 - \sin^2(\theta_i)}} \tag{5.52}$$

$$\text{TM case:} \quad r_{\text{TM}} = \frac{-\dot{n}^2\cos(\theta_i) - \sqrt{\dot{n}^2 - \sin^2(\theta_i)}}{\dot{n}^2\cos(\theta_i) + \sqrt{\dot{n}^2 - \sin^2(\theta_i)}} \tag{5.53}$$

where $\theta_i$ is the angle of incidence and the refractive index $\dot{n} \equiv n_2/n_1$. For a metal the Fresnel reflections are written as,

$$\text{TE dielectric-metal case:} \quad r_{\text{TE}} = \frac{\cos(\theta_i) - \sqrt{\tilde{n}^2 - \sin^2(\theta_i)}}{\cos(\theta_i) + \sqrt{\tilde{n}^2 - \sin^2(\theta_i)}} \tag{5.54}$$

$$\text{TM dielectric-metal case:} \quad r_{\text{TM}} = \frac{-\tilde{n}^2\cos(\theta_i) + \sqrt{\tilde{n}^2 - \sin^2(\theta_i)}}{\tilde{n}^2\cos(\theta_i) + \sqrt{\tilde{n}^2 - \sin^2(\theta_i)}} \tag{5.55}$$

where $\tilde{n}^2 = n_R + in_I$. We have two possible cases for the reflection coefficient,

$$\text{Case 1:} \quad r_{\text{TE,TM}} > 0, \quad \text{Case 2:} \quad r_{\text{TE,TM}} < 0.$$

For case 1 there are no phase changes upon reflection, whereas for case 2 there is a $\pi$ phase change as $r_{\text{TE,TM}} = -|r_{\text{TE,TM}}| = e^{i\pi}|r_{\text{TE,TM}}|$. Figure 5-7 shows the phase shift for the TE and TM modes upon reflection from a air-dielectric layer (left, right) and dielectric-metal layer (right). For AgI dielectric layer $n = 2$ and assuming an entrance angle of $\pi/2$, the modes both enter the dielectric at an angle of $\theta_i = 0.53$ radians which leads to $r_{\text{TE}} = -1$ and $r_{\text{TM}} = 1$ meaning that the initial reflection off the dielectric layers causes a $\pi$ phase shift only for the TE mode. The difference in the phases arises from the dielectric-metal layer. If this were a 'standard' HCNCF the air-dielectric-air model would be the best to describe how the phase of the TE and TM modes change in the structure. But we know that the location of the resonances for the the TE and TM modes are the same in a 'standard' HCNCF. In this case the TE modes has a 0 phase shift and the TM mode has a $\pi$ phase shift. However, changing the dielectric-air

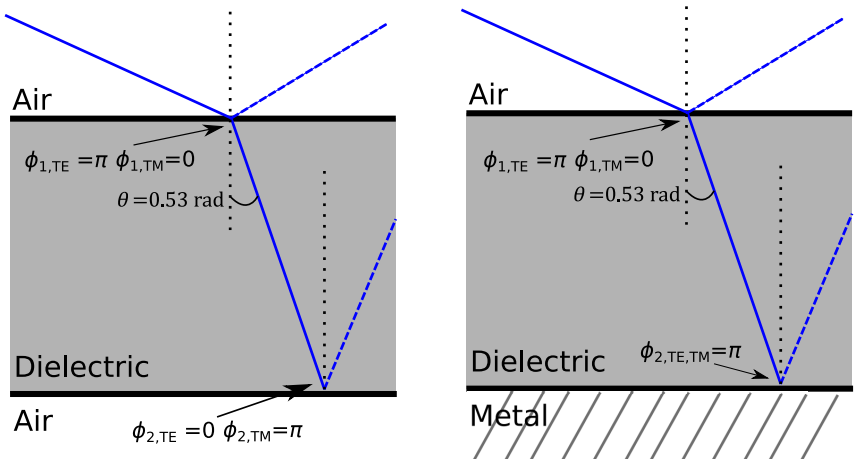


Figure 5-7: Comparing the phase changes $\phi$ upon reflections in an air-dielectric-air and air-dielectric-metal structure for TE and TM modes. The dotted lines are the reflected rays in the structure. Both models assume that the entry angle is 0.53 radians assuming the rays start at an angle of $\pi/2$ radians relative to the structure. (left) Shows the phase changes upon reflection for an air-dielectric-air structure. Only TE modes have a $\pi$ phase shift at the initial air-dielectric reflection. For the dielectric-air layer the TE modes undergoes 0 phase shift whilst the TM mode experiences a $\pi$ phase shift. (right) In the air-dielectric-metal structure, for the dielectric-metal layer both the TE and TM modes undergo a $\pi$ phase shift.

layer to a dielectric-metal layer causes the TE mode to undergo a $\pi$ phase shift. Using the parameters of this model where $\tilde{n}^2 = 11 + i70$ with the reflection angle being $\theta_i = 0.53$ radians returns reflection coefficients $r_{\mathrm{TE}} = -1 - i0.02$ and $r_{\mathrm{TM}} = -1 - i0.03$ which means that both the TE and TM modes undergo a $\pi$ phase shift. This 'extra' phase shift for the TE mode is the position of the resonances for TE and TM modes are not the same.

The objective is to compare the structure in figure 5-3 with an equivalent HCNCF model. As there is no analytical solution which can compute the loss in a HCNCF alternative numerical methods will have to be used, in this case the finite-element method. A commonly used modelling software COMSOL Multiphysics makes use of this technique. Before moving onto the HCNCF model, comparing the analytical Bragg fibre model with the finite-element equivalent is necessary to ensure that the physical effects of the metal layer are properly included. The difficulty in modelling a metal

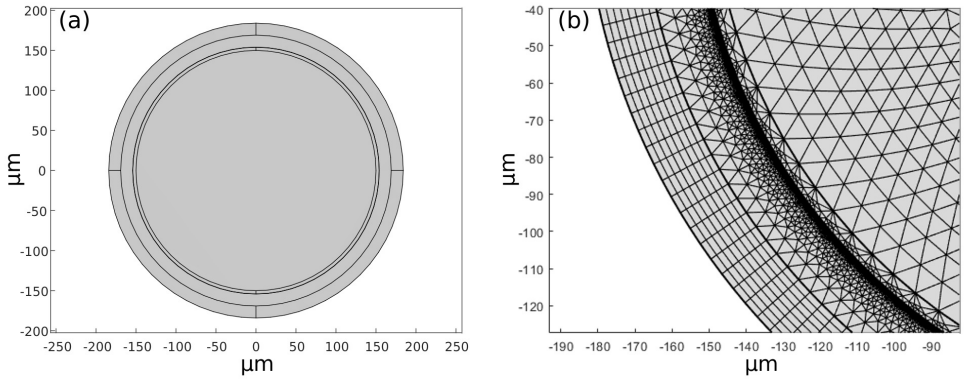


Figure 5-8: (a) Cylindrical hollow-core fibre model with an air core followed by a dielectric and then a metal layer which is surrounded by silica glass. (b) Free-triangular mesh in the entire structure with the outer most layer being mapped as it represents a perfectly matched layer. The physical parameters of this model are as follows, a core radius of 150 , a dielectric thickness layer which varies in thickness between 1.2 and 5 µm, a metal layer which is 100 nm thick and a cladding thickness of 30 µm.

using a finite element method comes from the skin depth. Skin depth, $\delta$, is defined as (Fox 2002)

$$\delta = \sqrt{\frac{\rho}{\pi f \mu_r \mu_0}} \tag{5.56}$$

where $\rho$ is the resistivity of the metal, $f$ is the frequency of the light, $\mu_r$ is the relative permeability and $\mu_0$ is the permeability constant ($\pi \cdot 10^{-7}$). For the metal used in this model Ag and at a wavelength of 10 µm the skin depth is 11.6 nm. To include a step-size of the order of the skin depth in a structure hundreds of microns across whilst keeping the computation time reasonable is the challenge, but is nonetheless important to properly model the effect of having a metal in the structure.

In order to tackle this problem understanding how the mesh is applied to this structure is key. Figure 5-8(a) shows the model used in this study whilst (b) represents the model with a 'free-triangular' mesh with the exception of the outermost layers which is a mapped meshing to efficiently implement the perfectly matched layer. The model has the following physical parameters, a core radius of 150 , a dielectric thickness layer which varies in thickness between 1.2 and 5 µm, a metal layer which is 100 nm thick

and a cladding thickness of 30 μm. The mesh type free triangular is excellent in most situations as it is a simple way to obtain high-quality elements regardless of the meshed geometry. It is effective for multimode fibres such as those in section 3 for example. However, when it comes to generating a very fine free-triangular mesh such as is required in this case the computational cost becomes too large. In figure 5-8(b) the required mesh size in the metal (preferably 2 nm in width and height to properly capture the skin depth effect) was not generated simply due to the required computational time to generate the mesh. This does not include the impractical amount of time it would take to solve the model. Moreover, there would need to be a gradual decline in the mesh size from the core to the metal layer to ensure the correct size of mesh in the correct region of the structure. For example, a large step size in the mesh size between the dielectric and metal layer will cause the mesh in the metal layer to be significantly larger than the target size, leading to inacurate results.

An alternative mesh geometry must be used. For this particular experiment we know that the solution of the models will not vary azimuthaly quickly. The free-triangular mesh would capture the azimuthal behaviour at a high resolution but since the so-

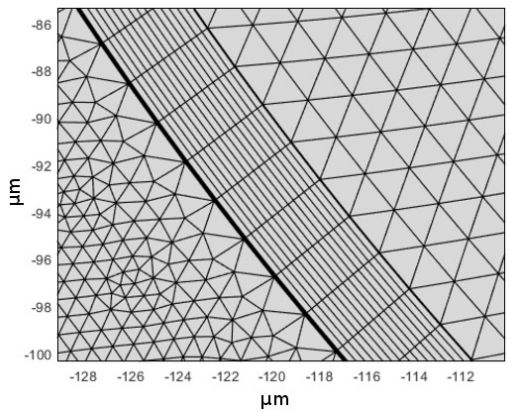


Figure 5-9: Cylindrical fibre model presented in figure 5-8(a) with the more efficient meshing method. The physics of the dielectric layer and metal layer (black line) are now calculated using a mapped meshing technique. The dimensions of the mapped mesh for the dielectric and metal layer are 2 μm azimuthely and 30 nm (dielectric) and 2 nm (metal) radially.

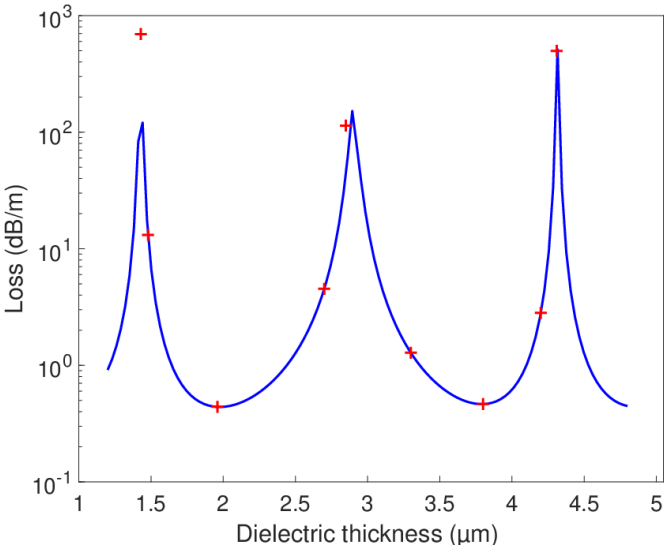


Figure 5-10: Comparison of the loss for the $HE_{11}$ mode between the analytical model for a cylindrical fibre and its COMSOL Multiphysics equivalent (red crosses). The core radius of the cylindrical fibre in this case was 150 μm.

lutions vary slowly azimuthaly this mesh type would provide more unecessary mesh points than needed making the simulation inefficient. A different solution would be to use a 'mapped' type of meshing with a small radial dimension whilst capturing the azimuthal behaviour at a lower resolution. This mapped meshing is therefore ideal for the model presented in figure 5-8(a). The new mesh configuration can be seen in figure 5-9. Here the radial density of the mesh is independent from the azimuthal density of mesh. Due to the radial independence the density of the mesh in the radial direction can be made to be very fine, in this case they are 2 nm apart in the metal which can capture the skin depth effects. Figure 5-10 shows the agreement between the analytical and numerical result for a purely cylindrical geometry. The accuracy indicates that the meshing structure is suitable to be transferred to a HCNCF model as the skin depth effects are captured by the mapped meshing.

The model structure of the HCNCF (figure 5-3) is shown in figure 5-11(a). In terms of material, the core is air, there is a dielectric layer of variable thickness on the outside

edge of the tubes with the same optical properties of AgI. The inside of the tubes is made from Ag, but it is split into 2 domains. The domain on the outer edge contains the mapped meshing and the domain which represents the rest of the tubes contains free-triangular mesh for computational purposes (figure 5-11(b)). The cladding is made from silica glass. The physical dimensions of the HCNCF model are core diameter of 150 µm, the inner diameter of the tubes is 135 µm. The dielectric layer thickness which ranges between 1.2 to 4.3 µm.

A key aspect that needs to be taken into account when evaluating the loss of the HCNCF and cylindrical fibre model is ensuring that the correct modes are being compared. For example, when comparing the loss of the $HE_{11}$ mode they must have the same $\Re(n_{\text{eff}})$, so they have the same $\beta$ and 'bounces' per unit length This was done by building multiple models of the cylindrical fibre which vary in core radius and comparing the $\Re(n_{\text{eff,cyl}})$ of the cylindrical fibre with that of the HCNCF model described here

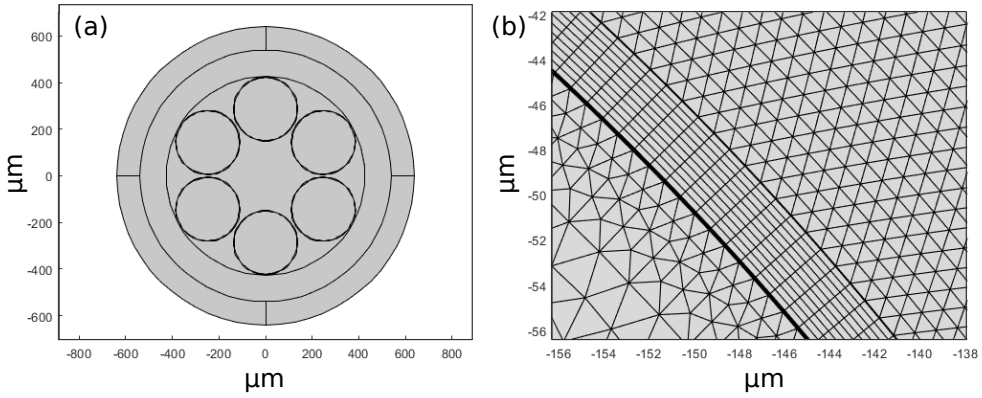


Figure 5-11: (a) HCNCF fibre model where the tubes are made of metal (Ag) and are surrounded by a dielectric material (AgI). The physical parameters are as follows, a core radius of 150 µm, a dielectric layer thickness which ranges between 1.2 to 4.3 µm, a metal tube with an inner diameter of 135 µm. The silica glass cladding is 213 µm thick. (b) A zoomed in image of a tube with the model's mesh superimposed. The core of the fibre has a free-triangular style mesh whilst the dilectric layer has a mapped mesh which is 30 nm in depth and 2 µm in length. Behind the dielectric layer there is a metal layer (thick black line) which is 100 nm thick. That layer also has a mapped mesh which is 2 nm in depth and 2 µm in length. The inside of the tubes is meshed with a free-triangular mesh.

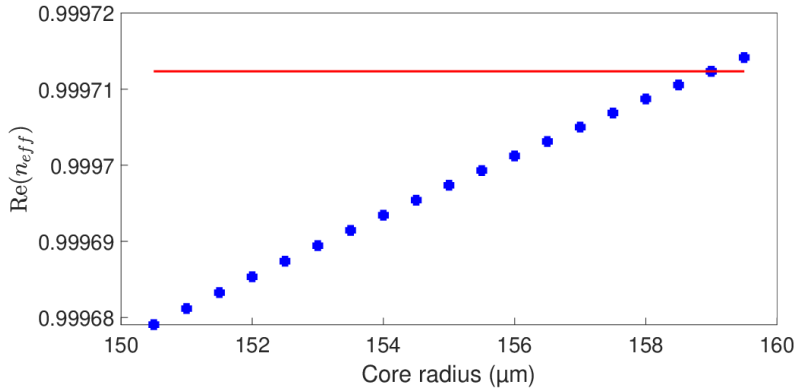


Figure 5-12: $\Re(n_{\text{eff}})$ matching between the cylindrical fibre and the HCNCF fibre shown in figure 5-11(a) for the $HE_{11}$ mode. The blue markers represent $\Re(n_{\text{eff}})$ as a function of core radius for the cylindrical model. The solid-red line shows the $\Re(n_{\text{eff}})$ value for the HCNCF. The matching occurs at a core radius of approximately 159 μm for the cylindrical fibre model.

($\Re(n_{\text{eff,HCNCF}})$). Figure 5-12 shows the $\Re(n_{\text{eff}})$ for the cylindrical fibre as a function of core radius (red marker) with the solid blue line representing $\Re(n_{\text{eff}})$ for the HCNCF in figuree 5-11(a). The results are for the $HE_{11}$ mode. We can see that the $\Re(n_{\text{eff}})$ matching requires a core radius of approximately 159 μm for the cylindrical fibre as at that location $(1 - \Re(n_{\text{eff,cyl}})) - (1 - \Re(n_{\text{eff,HCNCF}})) = -2 \cdot 10^{-10}$, confirming that a cylindrical fibre with this core radius provides like-for-like comparison of loss with the HCNCF model.

The comparison of the loss between the HCNCF (red markers) and the cylindrical Bragg fibre model (solid blue) equivalent is shown in figure 5-13. The results show in the low loss regions, in between the resonances, the loss for the HCNCF is marginally larger than that of the Bragg fibre. The result is strikingly different from the air-glass structure, where the HCNCF structure reduces the loss by orders of magnitude from a cylindrical geometry as it was speculated that the negative curvature of the walls in the HCNCF aid in lowering the loss. Therefore, the fact that with a metal layer the negative-curvature structure is higher loss than the cylindrical fibre indicates that the power of the antiresonant guidance mechanism in a silica-air HCNCF in lowering

loss is aided by the multiple reflections provided by the tubes. If the metal layer was swapped with air it would provide the opportunity for light which penetrates into the tube to reflect back from the next layer of glass it would encounter. The metal layer prevents these extra reflections from occurring. This finding is not only constrained to HE modes. Although TE and TM cannot exist in a HCNCF due to the lack of circular symmetry the quasi-TE/TM modes in the HCNCF (those which have a close match in terms of $\Re(n_{\text{eff}})$) also experience a higher loss in the HCNCF than in the Bragg fibre. For a dielectric wall thickness of 2 μm the loss of the $TE_{01}$ and $TM_{01}$ modes (including the degenerate pairs) are 1.3 dB/m, 0.94 dB/m, 0.55 dB/m and 0.94 dB/m. The quasi-TE/$M_{01}$ modes recorded a loss of 1.1 dB/m, 0.83 dB/m, 1.3 dB/m and 1.1 dB/m. Note that the order in which the losses are written for the HCNCF model not directly correspond to the equivalent modes in the Bragg fibre model. The theme of these results is that the loss is higher in the HCNCF model than in the Bragg fibre model for TE/M modes.

One of the goals of this thesis was to investigate whether or not a HCNCF structure with tubes coated with metal and a dielectric layer would produce lower loses than its cylindrical fibre equivalent. The conjecture arose because the negative curvature of the tubes was shown to reduce the loss in a silica-air fibre. Although the reason as to why this is the case is not currently known. However it was shown here that the loss actually increased slightly in the HCNCF structure when compared to the cylindrical model. The reason is attributed to the lack of air in the tubes. Some of the radiation which penetrated into the tube would have a chance to return to the core as there are multiple glass layers in which the light can interact with. Filling the tubes with a metal stops that effect and hence the antiresonant guidance can only benefit from the single reflection provided by the dielectric layer. Even though the result is negative the understanding of why gives a motivation on what to do next. For example, instead of

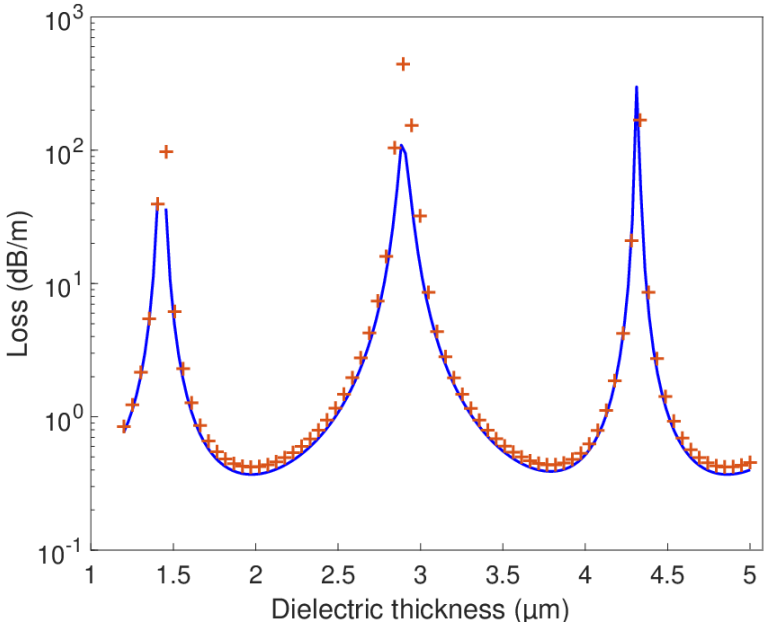


Figure 5-13: Loss comparison between the Bragg fibre model (solid blue) with a core radius of approximately 159 µm and the HCNCF equivalent (red crosses) for the $HE_{11}$ mode.

having the metal filled tube you replace it with air but make the walls of the tubes from a dielectric material with a low loss at 10 µm.

# Chapter 6

# The next steps

Over the course of this thesis I have described how a hollow-core negative curvature fibre can be fabricated to become highly-multimode and how that type of fibre is manufactured and suitable to guide VUV wavelengths. Work delving into the performance of this type of optical fibre in the IR shows that this model can be translated to longer wavelengths. However, the simulations showed that a HCNCF design for 10 μm guidance resulted in a higher loss than its equivalent cylindrical fibre. Even though the main goals of the research were achieved it would be worth discussing the areas in which there is room for improvement and also the next steps in the actual research itself.

Starting with the manufacturing side there are a few changes that would improve the consistency of the fabrication process. The first is to add a tension monitor for the stack to cane stage. Currently the way in which this stage is performed is by choosing the desired OD of the cane and then with a user chosen feed rate, through volume

conservation, the draw speed is calculated. Then the temperature of the furnace is reduced such that it minimises the collapse of the capillaries under their own surface tension. The problem with the current set-up is with regards to estimating the tension, as it is purely reliant on the temperature as the gauge due to the lack of a tension monitor. However, the temperature inside the furnace may not be uniform. Without understanding how the temperature varies across the furnace it is difficult to use the temperature as a gauge for future draws. Therefore, a tension monitor would bypass this issue as the tension is simply the result of the temperature of the glass and the speed that it is being fed into the furnace and pulled out of it. Tension is then a metric that one can use as a reliable target for the stack to cane process. Note that the tension is the driving parameter which is used during the draw of the preform to optical fibre. Secondly the Achilles heel of the entire manufacturing process is the central support tube. The central support tube is vital for keeping the tubes in the correct place in the stack to cane stage. The issue with the current manufacturing process is that the central support tubes are placed at the ends of the stacking tube. The capillaries are unable to flex near the central support tube which means they are in contact with the

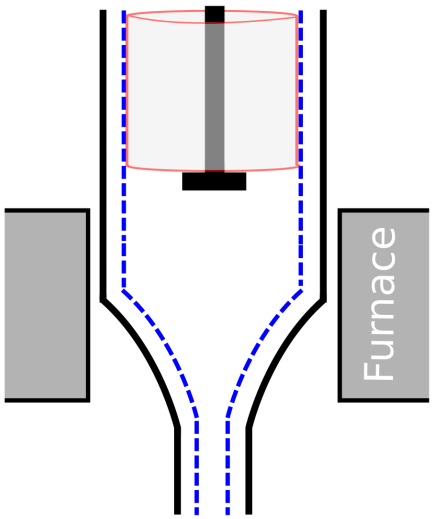


Figure 6-1: Schematic of potential replacement to the central support tube at the top of the stack. Instead a central support tube (red outline) is held in place by a rod (black) just above the furnace whilst the capillaries are fed into the furnace.

inner wall of the stacking tube and the spacing between the capillaries is uniform. In the middle of the stacking tube the capillaries (depending on their outer diameter and wall thicknesses) can flex. The flexing is due to the static electricity in the stacking tube. At the early stage when drawing the stacking tube it would regularly mean that the spacing between the capillaries is non-uniform. Furthermore, the structure is fed vertically into the furnace. As the central support tubes do not have much of an effect on keeping the capillaries near the center of the stacking tube taught and in place, the capillaries are more free to move. The vibrations during the draw process whilst passing the stacking tube into the furnace can cause the capillaries get out of contact with the inner wall of the stacking tube and move out of place, occasionally the capillaries will fuse together in the furnace. Due to the relatively low draw-down ratio from stack to cane and the fact that the canes are seldom optimal at the beginning and mid-stage of the draw the number of canes yielded is typically quite low. For example, when producing the multimode fibre shown in section 3.2 I obtained 2 canes. A future goal would be to modify the stack to cane stage with the goal of increasing the cane yield. One potential option would be to have a central support tube which sits just above the furnace and is held in place from the top of the stack. Figure 6-1 shows a schematic of the potential solution. The central support tube (red outline) is held in place by a rod (black) whilst the stack is fed into the furnace. Since the capillaries will be close to the central support just before the hot-zone of the furnace, the space between them will be uniform and they will be taught enough such that they will fuse to the inner wall of the stacking tube. Therefore, the number of canes that would be gathered would increase significantly. The issue that would have to be dealt with, aside from how the central support tube will be held in place without scratching the capillaries, is dealing with the static electricity. The static on the glass could prevent the capillaries to smoothly slide past the central support tube which would inevitably lead to the capillaries being damaged. Another possible technique to overcome this issue is to fuse the capillaries in place to the inside of the stacking tube using a laser (Wheeler et al. 2020). This would

ensure that the capillaries stay in place during the stack to cane stage maximising the number of canes which are gathered.

Once the optical fibre is manufactured tapering is required in order to reduce the tube wall thickness such that it can guide the VUV. The tapering process currently possesses limitations which when overcome would increase the quality of tapers and also the consistency between them. Much like the stack to cane stage on the fibre drawing tower, the taper rig lacks a tension monitor. Currently a heuristic approach is used when producing the tapers which a tension monitor would largely solve. The temperature of the flame is difficult to measure as it is dependent on not only the proportion of butane and oxygen that is being fed through it but also the local humidity and potential drafts in and around the torch. The position of the flame beneath optical fibre is also challenging to keep constant. A tension monitor would give a quantifiable measurement of the maximum stress that the sample can take at each phase of the tapering process, which would ensure the tubes inside the fibre suffer as minimal of a collapse as possible under their own surface tension. Another solution which could aid this problem of collapse is by pressurising the tubes during the tapering by gluing the core of the optical fibre. However, an issue with this solution would be that the pressurisation would need to increase as the outer diameter of the optical fibre is reduced during tapering.

The main goal of achieving VUV guidance was completed using a multimode HC-NCF with the shortest antiresonant guided wavelength being in the region of 135 nm. However, since it was shown that it is now possible it would be beneficial to know how short a wavelength can be guided through antiresonant guidance. There is a limiting physical factor which is the attenuation of the glass, however, as the tube wall thickness gets smaller there is less material to absorb the UV light. The future goal is to use these fibres on satellites and rovers for planetary missions. It would require a bundle

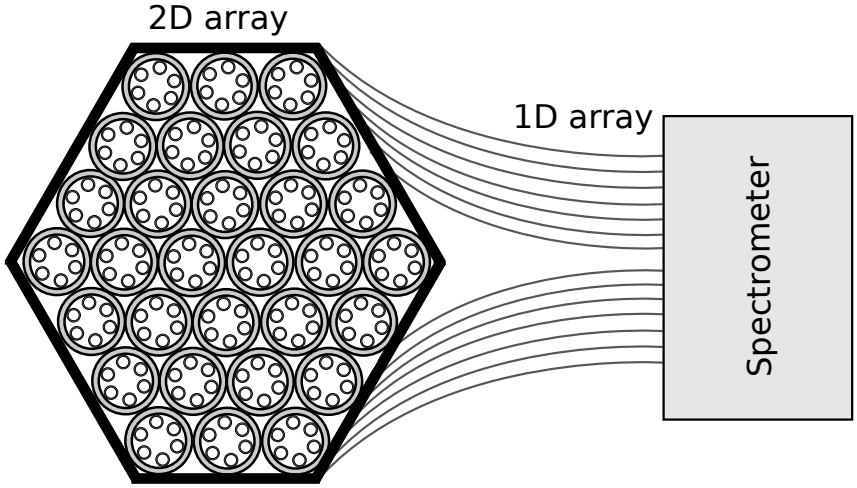


Figure 6-2: 2D array of tapered optical fibres which are then flattened to a 1D array. The output of each optical fibre is then incident onto a spectrometer.

of these of tens of fibres which start as a 2D array and are then flattened into 1D before their outputs are incident onto a spectrometer (figure 6-2). Building this set-up is crucial for the eventual application of such a fibre. Therefore, the outlined potential improvements to the taper rig are important in order to consistently produce these optical fibres as the bundle could contain tens of fibres. Furthermore the improvement to the optical setup used to measure the VUV spectra would be beneficial in order to increase the signal to noise at the shorter end of the VUV ($< 130$ nm). Currently the set-up is purged with nitrogen which does mitigate the atmospheric absorption of VUV wavelengths below 180 nm but improvements would be made if the entire set-up was evacuated. This case would not only simulate conditions in which these fibres would be used but there may be structures in the VUV spectra which would be revealed in a vacuum.

The current set-up is also limited in its capability of performing bend loss and cut-back measurements. Adding a rotation stage to the experimental set-up would fix this issue and allow for bend loss measurements to be made (figure 6-3(a)). The coupling between the deuterium lamp and input end of the optical fibre occurs on top of the

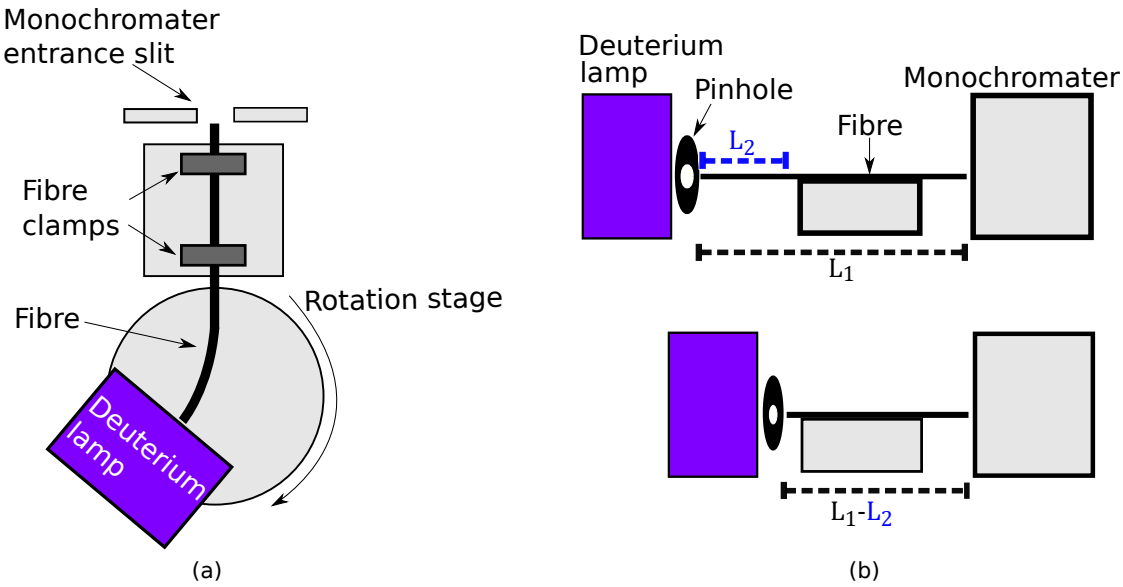


Figure 6-3: (a) Proposed set-up for bend loss measurements. The deuterium lamp couples light into the optical fibre from the rotation stage. (b) Potential cut-back measurement. (Top) The transmission signal of the optical fibre, for the long length $L_1$, is maximised by aligning the core of the fibre with the pinhole. (Bottom) Length $L_2$ is removed from the fibre and the deuterium lamp and pinhole is moved a distance $L_2$ closer to the optical fibre. The transmission is then again maximised for the shorter length fibre.

rotation stage in order to control the bend of the optical fibre. Figure 6-3(b) shows a proposed method to obtain a loss for the VUV fibres using a modified version of the cut-back method. Instead of keeping the coupling at the input end of the optical fibre constant the output end is kept the same. This would be done to ensure that the light collected by the monochromator is constant as aligning to it is very challenging. A pinhole is placed in a fixed position in front of the deuterium lamp. The optical fibre's transmission of length $L_1$ is then maximised by aligning its core with the pinhole. A length $L_2$ is then cut and the deuterium lamp as well as the pinhole is moved a distance $L_2$ closer to the new input end of the shorter fibre. The transmission of the shorter fibre is then maximised so equation (2.20) can be used to obtain a loss in dB. The problem that would need to be overcome with this method is ensuring that the signal for both transmission measurements for lengths $L_1$ and $L_1 - L_2$ are maximised. The next problem is measuring the uncertainty in the attenuation of the fibre. This

is usually done by repeating the transmission measurement for both lengths multiple times but modifying the set-up slightly between each measurement. The modifications could be either cleaving the end of the fibre or slightly perturbing the layout of the fibre (or both). Neither of these methods are possible due to the set-up and length of fibre sample. However, in spite of these problems attempts to measure the bend loss and attenuation would give a greater insight into the performance of these optical fibres in the VUV. Both of these modifications to the set-up are currently being worked on at LASP (University of Colorado).

The calculation for the HCNCF at 10 μm shows that the metal tubed model performs worse in terms of loss than its cylindrical counterpart. The result was a surprise as silica glass HCNCF have losses which are far lower than a silica glass hollow cylindrical fibre. The difference here is that the tubes are now filled with a metal which reduces the number of antiresonant layers which would otherwise be there in a silica glass fibre. The lower the number of antiresonant layers the lower the number of reflections back into the core, hence the loss in increased. Although the layering structure, i.e. air to dielectric to metal, produces greater losses it does raise the possibility of producing non-silica glass based HCNCF. Since the number of antiresonant layers reduces the loss, replacing the material the tubes are made of with one that is low loss at about 10 μm would lead to a HCNCF which is lower loss than state-of-the-art cylindrical based fibres. The question would be how to manufacture these types of fibres.

The work presented here showed that VUV guidance is possible with optical fibres. The next steps are to produce these optical fibres for their intended applications in space-based technologies. Furthermore, the result for the HCNCF at 10 μm shows the importance in the number of antiresonant layers to aid in the reduction of the loss. Moving into the mid-IR the next goal would be to manufacture a HCNCF where the tubes are made of a low loss material for those wavelengths.

# References


Belardi, W. 2015, 'Design and properties of hollow antiresonant fibers for the visible and near infrared spectral range', *Journal of Lightwave Technology* **33**(21), 4497–4503.

Belardi, W. and Knight, J. C. 2014, 'Hollow antiresonant fibers with low bending loss', *Optics express* **22**(8), 10091–10096.

Bérenger, J.-P. 2007, 'Perfectly matched layer (pml) for computational electromagnetics', *Synthesis Lectures on Computational Electromagnetics* **2**(1), 1–117.

Bird, D. 2017, 'Attenuation of model hollow-core, anti-resonant fibres', *Optics express* **25**(19), 23215–23237.

Birks, T. A. and Li, Y. W. 1992, 'The shape of fiber tapers', *Journal of Lightwave Technology* **10**(4), 432–438.

Buchanan, M. 2015, 'Physics in finance: Trading at the speed of light', *Nature* **518**(7538), 161–163.

Canit, J., Billardon, M. and Badoz, J. 1969, 'Relationship between the real and imaginary parts of the refractive index', *JOSA* **59**(8), 1000–1001.

Carter, R. M., Yu, F., Wadsworth, W. J., Shephard, J. D., Birks, T., Knight, J. C. and Hand, D. P. 2017, 'Measurement of resonant bend loss in anti-resonant hollow core optical fiber', *Optics express* **25**(17), 20612–20621.

Chamberlin, P. C., Woods, T. N. and Eparvier, F. G. 2004, Rocket extreme ultraviolet grating spectrometer (egs): calibrations and results of the solar irradiance on february 8, 2002, *in* 'Optical Constants of Materials for UV to X-Ray Wavelengths', Vol. 5538, International Society for Optics and Photonics, pp. 31–42.

Debord, B., Amsanpally, A., Chafer, M., Baz, A., Maurel, M., Blondy, J., Hugonnot, E., Scol, F., Vincetti, L., Gérôme, F. et al. 2017, 'Ultralow transmission loss in inhibited-coupling guiding hollow fibers', *Optica* **4**(2), 209–217.

Dudley, J. M. and Taylor, J. R. 2010, *Supercontinuum generation in optical fibers*, Cambridge University Press.

Fabian, H., Grzesik, U., Wörner, K.-H. and Klein, K.-F. 1991, Optical fibers for uv applications, *in* 'Glasses for Optoelectronics II', Vol. 1513, International Society for Optics and Photonics, pp. 168–173.

Farid, N., Li, C., Wang, H. and Ding, H. 2013, 'Laser-induced breakdown spectroscopic characterization of tungsten plasma using the first, second, and third harmonics of an nd: Yag laser', *Journal of nuclear materials* **433**(1-3), 80–85.

Février, S., Gérôme, F., Labruyère, A., Beaudou, B., Humbert, G. and Auguste, J.-L. 2009, 'Ultraviolet guiding hollow-core photonic crystal fiber', *Optics letters* **34**(19), 2888–2890.

Fox, M. 2002, 'Optical properties of solids'.

Frei, W. 2015, 'Using perfectly matched layers and scattering boundary conditions for wave electromagnetics problems', *Comsol Blog* .

Friebele, E. J. 1986, 'Radiation effects on glass', *Pergamon Press Ltd, Encyclopedia of Materials Science and Engineering.* **6**.

Friebele, E., Long, K., Askina, C., Gingerich, M., Marrone, M. and Griacom, D. 1985, Overview of radiation effects in fiber optics, *in* 'Radiation Effects on Optical Materials', Vol. 541, International Society for Optics and Photonics, pp. 70–88.

Galeener, F. L. 1985, 'Raman and esr studies of the thermal history of amorphous sio2', *Journal of Non-Crystalline Solids* **71**(1-3), 373–386.

Galleani, G., Ledemi, Y., de Lima Filho, E. S., Morency, S., Delaizir, G., Chenu, S., Duclere, J. R. and Messaddeq, Y. 2017, 'Uv-transmitting step-index fluorophosphate glass fiber fabricated by the crucible technique', *Optical Materials* **64**, 524–532.

Gao, F. and Han, L. 2012, 'Implementing the nelder-mead simplex algorithm with adaptive parameters', *Computational Optimization and Applications* **51**(1), 259–277.

Gao, S.-F., Wang, Y.-Y., Ding, W. and Wang, P. 2018, 'Hollow-core negative-curvature fiber for uv guidance', *Optics letters* **43**(6), 1347–1350.

Gao, S.-F., Wang, Y.-Y., Liu, X.-L., Ding, W. and Wang, P. 2016, 'Bending loss characterization in nodeless hollow-core anti-resonant fiber', *Optics express* **24**(13), 14801–14811.

George, R. and Harrington, J. A. 2005, 'Infrared transmissive, hollow plastic waveguides with inner ag–agi coatings', *Applied optics* **44**(30), 6449–6455.

Gürtler, P., Saile, V. and Koch, E. 1977, 'High resolution absorption spectrum of nitrogen in the vacuum ultraviolet', *Chemical Physics Letters* **48**(2), 245–250.

Habib, M. S., Markos, C., Antonio-Lopez, J. E., Correa, R. A., Bang, O. and Bache, M. 2018, 'Multi-stage generation of extreme ultraviolet dispersive waves by tapering gas-filled hollow-core anti-resonant fibers', *Optics express* **26**(19), 24357–24371.

Häffner, H., Hänsel, W., Roos, C., Benhelm, J., Chwalla, M., Körber, T., Rapol, U., Riebe, M., Schmidt, P., Becher, C. et al. 2005, 'Scalable multiparticle entanglement of trapped ions', *Nature* **438**(7068), 643–646.

Hanna, R. 1965, 'Infrared absorption spectrum of silicon dioxide', *Journal of the American Ceramic Society* **48**(11), 595–599.

Harrington, J. A. 2000, 'A review of ir transmitting, hollow waveguides', *Fiber & Integrated Optics* **19**(3), 211–227.

Harrington, J. A. and Gregory, C. C. 1990, 'Hollow sapphire fibers for the delivery of co 2 laser energy', *Optics Letters* **15**(10), 541–543.

Hartung, A., Kobelke, J., Schwuchow, A., Wondraczek, K., Bierlich, J., Popp, J., Frosch, T. and Schmidt, M. A. 2015, 'Origins of modal loss of antiresonant hollow-core optical fibers in the ultraviolet', *Optics Express* **23**(3), 2557–2565.

Hassan, M. R. A., Yu, F., Wadsworth, W. J. and Knight, J. C. 2016, 'Cavity-based mid-ir fiber gas laser pumped by a diode laser', *Optica* **3**(3), 218–221.

Hecht, C. J. and Hecht, J. 1999, *City of light: the story of fiber optics*, Oxford University Press on Demand.

Hecht, E. 2016, *Optics*, Pearson.

Hecht, J. 2015, *Understanding fiber optics*, Jeff Hecht.

Heimann, J., Klein, K.-F., Gonschior, C. P., Klein, M. and Hillrichs, G. 2013, Optical fibers for 355nm pulsed lasers and high-power broadband light sources, *in* 'Optical Fibers and Sensors for Medical Diagnostics and Treatment Applications XIII', Vol. 8576, International Society for Optics and Photonics, p. 85760K.

Heitmann, W. 1990, 'Attenuation analysis of silica-based single-mode fibers', *Journal of optical communications* **11**(4), 122–129.

Hennessy, J. J., Balasubramanian, K., Moore, C. S., Jewell, A. D., Nikzad, S., France, K. C. and Quijada, M. A. 2016, 'Performance and prospects of far ultraviolet alu-

minum mirrors protected by atomic layer deposition', *Journal of Astronomical Telescopes, Instruments, and Systems* **2**(4), 041206.

Hu, J. and Menyuk, C. R. 2009, 'Understanding leaky modes: slab waveguide revisited', *Advances in Optics and Photonics* **1**(1), 58–106.

Huebner, M., Meyer, H., Klein, K.-F., Hillrichs, G., Ruetting, M., Veidemanis, M., Spangenberg, B., Clarkin, J. P. and Nelson, G. W. 2000, Fiber optic systems in the uv region, *in* 'Biomedical Diagnostic, Guidance, and Surgical-Assist Systems II', Vol. 3911, International Society for Optics and Photonics, pp. 303–312.

Jin, J.-M. 2015, *The finite element method in electromagnetics*, John Wiley & Sons.

Kajihara, K., Ikuta, Y., Oto, M., Hirano, M., Skuja, L. and Hosono, H. 2004, 'Uv–vuv laser induced phenomena in sio2 glass', *Nuclear Instruments and Methods in Physics Research Section B: Beam Interactions with Materials and Atoms* **218**, 323–331.

Karlitschek, P., Hillrichs, G. and Klein, K.-F. 1995, 'Photodegradation and nonlinear effects in optical fibers induced by pulsed uv-laser radiation', *Optics communications* **116**(1-3), 219–230.

Key, P. and Preston, R. 1980, 'Magnesium fluoride windowed deuterium lamps as radiance transfer standards between 115 and 370 nm', *Journal of Physics E: Scientific Instruments* **13**(8), 866.

Khalilov, V. K., Dorfman, G., Danilov, E., Guskov, M. and Ermakov, V. 1994, 'Character, mechanism of formation and transformation of point defects in type iv silica glass', *Journal of non-crystalline solids* **169**(1-2), 15–28.

Khalilov, V., Shannon, J. and Timmerman, R. 2014, Improved deep uv fiber for medical and spectroscopy applications, *in* 'Optical Fibers and Sensors for Medical Diagnostics and Treatment Applications XIV', Vol. 8938, International Society for Optics and Photonics, p. 89380A.

Khalilov, V., Shannon, J., Timmerman, R. and Geshell, D. 2015, Improved deep uv fiber for medical and spectroscopy applications, *in* 'Optical Fibers and Sensors for Medical Diagnostics and Treatment Applications XV', Vol. 9317, International Society for Optics and Photonics, p. 93170F.

Kitamura, R., Pilon, L. and Jonasz, M. 2007, 'Optical constants of silica glass from extreme ultraviolet to far infrared at near room temperature', *Applied optics* **46**(33), 8118–8133.

Klein, K.-F., Hillrichs, G., Karlitschek, P. and Mann, K. R. 1997, Possibilities and limitations of optical fibers for the transmission of excimer laser radiation, *in* 'Laser-Induced Damage in Optical Materials: 1996', Vol. 2966, International Society for Optics and Photonics, pp. 564–573.

Klein, K.-F. and Khalilov, V. K. 2015, Uv-fibers: two decades of improvements for new applications, *in* 'Optical Fibers and Sensors for Medical Diagnostics and Treatment Applications XV', Vol. 9317, International Society for Optics and Photonics, p. 93170S.

Kokubun, Y. and Iga, K. 1980, 'Mode analysis of graded-index optical fibers using a scalar wave equation including gradient-index terms and direct numerical integration', *JOSA* **70**(4), 388–394.

Kolyadin, A. N., Kosolapov, A. F., Pryamikov, A. D., Biriukov, A. S., Plotnichenko, V. G. and Dianov, E. M. 2013, 'Light transmission in negative curvature hollow core fiber in extremely high material loss region', *Optics express* **21**(8), 9514–9519.

Kriesel, J. M., Gat, N., Bernacki, B. E., Erikson, R. L., Cannon, B. D., Myers, T. L., Bledt, C. M. and Harrington, J. A. 2011, Hollow core fiber optics for mid-wave and long-wave infrared spectroscopy, *in* 'Chemical, Biological, Radiological, Nuclear, and Explosives (CBRNE) Sensing XII', Vol. 8018, International Society for Optics and Photonics, p. 80180V.

Langmuir, I. 1915, 'The melting-point of tungsten', *Physical Review* **6**(2), 138.

Lin, X., Shi, Y.-W., Sui, K.-R., Zhu, X.-S., Iwai, K. and Miyagi, M. 2009, 'Fabrication and characterization of infrared hollow fiber with multi-sio 2 and agi inner-coating layers', *Applied optics* **48**(35), 6765–6769.

Lipson, A., Lipson, S. G. and Lipson, H. 2010, *Optical physics*, Cambridge University Press.

Litchinitser, N., Abeeluck, A., Headley, C. and Eggleton, B. 2002, 'Antiresonant reflecting photonic crystal optical waveguides', *Optics letters* **27**(18), 1592–1594.

Love, A. 2018, *Hollow Core Optical Fibre Based Gas Discharge Laser Systems*, Springer.

Ludlow, A. D., Boyd, M. M., Ye, J., Peik, E. and Schmidt, P. O. 2015, 'Optical atomic clocks', *Reviews of Modern Physics* **87**(2), 637.

Marcatili, E. A. and Schmeltzer, R. 1964, 'Hollow metallic and dielectric waveguides for long distance optical transmission and lasers', *Bell System Technical Journal* **43**(4), 1783–1809.

Marcuse, D. 2012, *Principles of optical fiber measurements*, Elsevier.

Matsuura, Y., Hongo, A. and Miyagi, M. 1990, 'Dielectric-coated metallic hollow waveguide for 3-$\mu$m er: Yag, 5-$\mu$m co, and 10.6-$\mu$m co 2 laser light transmission', *Applied optics* **29**(15), 2213–2214.

Matsuura, Y. and Miyagi, M. 1993, 'Er: Yag, co, and co 2 laser delivery by zns-coated ag hollow waveguides', *Applied optics* **32**(33), 6598–6601.

Matsuura, Y. and Miyagi, M. 1998, 'Flexible hollow waveguides for delivery of excimer-laser light', *Optics letters* **23**(15), 1226–1228.

Matsuura, Y. and Miyagi, M. 1999, 'Aluminum-coated hollow glass fibers for arf-excimer laser light fabricated by metallorganic chemical-vapor deposition', *Applied optics* **38**(12), 2458–2462.

Matsuura, Y. and Miyagi, M. 2004, 'Hollow optical fibers for ultraviolet and vacuum ultraviolet light', *IEEE Journal of Selected Topics in Quantum Electronics* **10**(6), 1430–1434.

Modes, I. E. T. W. G. 2020, 'Optical processes in microcavities', *Physical Review B* **101**(20).

Peng, K., Zhan, H., Ni, L., Wang, X., Wang, Y., Gao, C., Li, Y., Wang, J., Jing, F. and Lin, A. 2016, 'Single-mode large-mode-area laser fiber with ultralow numerical aperture and high beam quality', *Applied optics* **55**(35), 10133–10137.

Phillips, A. C. 2013, *Introduction to quantum mechanics*, John Wiley & Sons.

Poletti, F. 2014, 'Nested antiresonant nodeless hollow core fiber', *Optics express* **22**(20), 23807–23828.

Pryamikov, A. D., Biriukov, A. S., Kosolapov, A. F., Plotnichenko, V. G., Semjonov, S. L. and Dianov, E. M. 2011, 'Demonstration of a waveguide regime for a silica hollow-core microstructured optical fiber with a negative curvature of the core boundary in the spectral region¿ 3.5 $\mu$m', *Optics express* **19**(2), 1441–1448.

Russell, P. 2003, 'Photonic crystal fibers', *science* **299**(5605), 358–362.

Saggese, S. J., Harrington, J. A. and Sigel, G. H. 1991, 'Attenuation of incoherent infrared radiation in hollow sapphire and silica waveguides', *Optics letters* **16**(1), 27–29.

Saito, M., Matsuura, Y., Kawamura, M. and Miyagi, M. 1990, 'Bending losses of incoherent light in circular hollow waveguides', *JOSA A* **7**(11), 2063–2068.

Sampaolo, A., Patimisco, P., Kriesel, J. M., Tittel, F. K., Scamarcio, G. and Spagnolo, V. 2015, 'Single mode operation with mid-ir hollow fibers in the range 5.1-10.5 $\mu$m', *Optics Express* **23**(1), 195–204.

Siegel Jr, G. 1974, 'Ultraviolet spectra of silicate glasses: a review of some experimental evidence', *Journal of Non-Crystalline Solids* **13**(3), 372–398.

Siesler, H. W. 2008, 'Basic principles of near-infrared spectroscopy', *Practical Spectroscopy Series* **35**, 7.

Skuja, L., Hosono, H. and Hirano, M. 2001, Laser-induced color centers in silica, *in* 'Laser-Induced Damage in Optical Materials: 2000', Vol. 4347, International Society for Optics and Photonics, pp. 155–168.

Stone, J., Wadsworth, W. and Knight, J. 2013, '1064 nm laser-induced defects in pure sio 2 fibers', *Optics letters* **38**(15), 2717–2719.

Tabor, D. and Tabor, D. 1991, *Gases, liquids and solids: and other states of matter*, Cambridge university press.

Uebel, P., Günendi, M. C., Frosz, M. H., Ahmed, G., Edavalath, N. N., Ménard, J.-M. and Russell, P. S. J. 2016, 'Broadband robustly single-mode hollow-core pcf by resonant filtering of higher-order modes', *Optics letters* **41**(9), 1961–1964.

Van Putten, L. D., Fokoua, E. N., Mousavi, S. M. A., Belardi, W., Chaudhuri, S., Badding, J. V. and Poletti, F. 2016, 'Exploring the effect of the core boundary curvature in hollow antiresonant fibers', *IEEE Photonics Technology Letters* **29**(2), 263–266.

Wan, Y., Gebert, F., Wübbena, J. B., Scharnhorst, N., Amairi, S., Leroux, I. D., Hemmerling, B., Lörch, N., Hammerer, K. and Schmidt, P. O. 2014, 'Precision spectroscopy by photon-recoil signal amplification', *Nature communications* **5**(1), 1–6.

Wang, Y. and Ding, W. 2017, 'Confinement loss in hollow-core negative curvature fiber: A multi-layered model', *Optics Express* **25**(26), 33122–33133.

Weeks, R. A. 1994, 'The many varieties of e centers: a review', *Journal of non-crystalline solids* **179**, 1–9.

Weir, C., Lippincott, E., Van Valkenburg, A. and Bunting, E. 1959, 'Infrared studies in the 1-to 15-micron region to 30,000 atmospheres', *Journal of research of the National Bureau of Standards. Section A, Physics and chemistry* **63**(1), 55.

Wheeler, N., Shardlow, P. and Poletti, F. 2020, 'Method for fabricating an optical fibre preform'. US Patent App. 16/628,423.

White, H. E. et al. 1962, 'Modern college physics'.

Wilkinson, P. G. and Johnston, H. L. 1950, 'The absorption spectra of methane, carbon dioxide, water vapor, and ethylene in the vacuum ultraviolet', *The Journal of Chemical Physics* **18**(2), 190–193.

Winter, B., Birks, T. A. and Wadsworth, W. J. 2019, Multimode hollow-core anti-resonant optical fibres, *in* 'Laser Science', Optical Society of America, pp. JTu4A–18.

Winter, B., Vorobiev, D., Fleming, B., Witt, E., Gilliam, W., Rusimova, K. R., Yerolatsitis, S., Birks, T. A. and Wadsworth, W. J. 2019, 185nm guidance in a hollow core optical fibre, *in* 'Laser Science', Optical Society of America, pp. JTu3A–19.

Yao, C., Jia, Z., Li, Z., Jia, S., Zhao, Z., Zhang, L., Feng, Y., Qin, G., Ohishi, Y. and Qin, W. 2018, 'High-power mid-infrared supercontinuum laser source using fluorotellurite fiber', *Optica* **5**(10), 1264–1270.

Yeh, C. 2013, *Handbook of fiber optics: Theory and applications*, Academic Press.

Yeh, P., Yariv, A. and Marom, E. 1978, 'Theory of bragg fiber', *JOSA* **68**(9), 1196–1201.

Yu, F. 2013, Hollow core negative curvature optical fibres, PhD thesis, University of Bath.

Yu, F., Cann, M., Brunton, A., Wadsworth, W. and Knight, J. 2018, 'Single-mode solarization-free hollow-core fiber for ultraviolet pulse delivery', *Optics express* **26**(8), 10879–10887.

Yu, F. and Knight, J. C. 2016, 'Negative curvature hollow-core optical fiber', *IEEE J. Sel. Top. Quantum Electron.* **22**(2), 146–155.

Yu, F., Wadsworth, W. J. and Knight, J. C. 2012, 'Low loss silica hollow core fibers for 3–4 $\mu$m spectral region', *Optics express* **20**(10), 11153–11158.

Zhang, J.-Y. and Boyd, I. W. 2000, 'Lifetime investigation of excimer uv sources', *Applied surface science* **168**(1-4), 296–299.